This is a preproof accepted article for *Mineralogical Magazine*
This version may be subject to change during the production process
DOI: 10.1180/mgm.2025.10124

Petrographic and trace element characterisation of diagenetic carbonates associated with Pb-Zn sulfide and fluorite mineralisation (Upper Triassic, Lombardy Basin, Northern Italy)

Niccolò Coccia*[a], Giovanna Della Porta[a], Fabrizio Berra[a], Marilena Moroni[a], Massimo Tiepolo[a]

[a] Earth Sciences Department "Ardito Desio", University of Milan, via Mangiagalli 34, 20133 Milan, Italy.

Manuscript submission date: 29-09-2024. Received in revised form: 04-06-2025. Accepted: 04-07-2025.

Abstract

The petrographic and geochemical characterisation of the diagenetic calcite and dolomite phases associated with carbonate-hosted ore deposits can contribute to a better understanding of the mineralisation mechanisms. The Lower Carnian Breno Formation and Calcare Metallifero Bergamasco in the Dossena area (Gorno mining district, Lombardy Basin, Southern Alps) are two shallow marine carbonate lithostratigraphic units hosting Alpine-Type Pb-Zn-F-Ba ores. Several interpretations were proposed for the genesis of mineralisation in these Triassic carbonates: syngenetic from submarine exhalations linked to the Ladinian-Carnian volcanism; or Alpine-Type syngenetic to epigenetic in burial settings by hydrothermal fluids, during Early-Middle Jurassic rifting. More recent studies propose that ores formed in shallow burial settings (tens to few hundreds of metres), precipitated from hydrothermal fluids related to Triassic magmatism, before the Early Jurassic rifting.

Petrographic analysis, $\delta^{18}O$ values, $REEY_N$ normalised patterns, calculated element ratios and Lanthanum-La, Cerium-Ce and Europium-Eu normalised anomalies suggest precipitation of the saddle dolomite and calcite cements, filling-fractures preceding and post-dating the mineralisation, from low temperature (<200° C) hydrothermal

Corresponding author e-mail: niccolo.coccia@unimi.it

COCCIA N. https://orcid.org/0009-0004-2551-7169; DELLA PORTA G. https://orcid.org/0000-0003-3479-0592; BERRA F. https://orcid.org/0000-0002-4354-1806; MORONI M. https://orcid.org/0000-0003-1443-1808; TIEPOLO M. https://orcid.org/0000-0001-7575-8105

fluids. The geochemistry of these fluids was influenced by seawater and burial basinal brines. $REEY_N$ patterns and Y/Ho ratios suggest the interaction of these fluids with Permian and Ladinian-Carnian siliciclastic and volcaniclastic deposits and/or with the Variscan metamorphic basement, which are possible sources for metals.

The identified paragenesis supports a hydrothermal epigenetic origin for the mineralisation, at burial depths not shallower than 300 m. In fact, pre-mineralisation fractures filled by saddle dolomite and calcite cements cross-cut voids occluded by burial sparite cements and stylolites in an already lithified host rock, affected by burial compaction and pressure solution.

These results may contribute to the understanding of other global occurrences of carbonate-hosted Pb-Zn mineralisation, providing new insights into complex dolomite and calcite paragenesis preceding and following the ore formation.

***Keywords*:** fracture-filling carbonates; saddle dolomite; Pb-Zn mineralisation; fluorite; Southern Alps; Triassic

Introduction

Carbonate sediment and rocks are affected by diagenetic processes driven by the interaction with different aqueous fluids (marine, meteoric, burial, hydrothermal) at changing temperature and pressure conditions, resulting in several episodes of authigenic carbonate mineral precipitation (through cementation, recrystallisation, replacement) and dissolution (Morad et al., 2000; 2010; Rasmussen and Krapez, 2000; Packard et al., 2001). Authigenic calcite and dolomite crystals precipitated as cements filling primary and secondary porosity or fractures and as replacive mineral phases may be associated with economically significant sediment-hosted orebodies, e.g. hydrocarbon (Ronchi et al., 2012), Pb-Zn-F-Ba (Leach et al., 2005; Davies and Smith, 2006) and Cu-Co-Ni-Ag-Zn-Pb (Bertrandsson Erlandsson et al., 2022). The genesis of ores is often of difficult interpretation and the study of diagenetic carbonates preceding and post-dating the formation of orebodies can help deciphering the characteristics of the fluids associated with the mineralisation and the timing of ore formation (e.g. Mondillo et al., 2020; Giorno et al., 2022; Stacey et al., 2022; Navarro-Ciurana et al., 2023). In the Southern Alps mining districts, several studies focussed on the diagenesis of the carbonate host rocks and of authigenic phases associated with Pb-Zn sulfide (galena PbS and sphalerite ZnS), fluorite (CaF_2) and baryte ($BaSO_4$) ores and the genesis of this mineralisation (Table 1; Lombardy Basin:

https://doi.org/10.1180/mgm.2025.10124 Published online by Cambridge University Press

Omenetto, 1966; Vachè, 1966; Assereto et al., 1977; Omenetto and Vailati, 1977; Rodeghiero et al., 1986; Mondillo et al., 2020; Giorno et al., 2022), as well as in other Alpine domains (Table 1; Zeeh et al., 1998; Kuhlemann et al., 2001; Palinkas et al., 2008; Brusca et al., 2010; Henjes-Kunst et al., 2017). However, the trace element characterisation of carbonate phases associated with ore minerals, which is experiencing a rising scientific interest (e.g. Rieger et al., 2021; Stacey et al., 2022; Navarro-Ciurana et al., 2023 and references therein), has not been previously performed on the Pb-Zn deposits in the Southern Alps and may provide significant information useful for a better understanding of the mineralisation mechanisms.

This study aims at providing new detailed petrographic and geochemical data to evaluate the diagenetic conditions affecting the Upper Triassic shallow-water carbonates of the Breno Formation and Calcare Metallifero Bergamasco, hosting Alpine-Type Pb-Zn sulfide and fluorite ores in the Dossena mines area (Gorno mining district, Orobic Alps, Lombardy Basin, North Italy; Figs 1, 2). The main focus is on the calcite and dolomite diagenetic phases associated with the ore minerals, which have been extensively exploited in particular for fluorite extraction at the beginning of the twentieth century, considering its increasing application in metallurgy and in the glass industry (Assereto et al., 1977). Even though known for a long time, the ore and the associated diagenetic carbonates in Dossena have been underexplored, considering that the last detailed study was carried out by Assereto et al. (1977).

Review of types of Pb-Zn-F-Ba sediment-hosted orebodies

Sediment-hosted Pb-Zn-F-Ba ores account for 57% Zn and 63% Pb global reserves (Mudd et al., 2017) and are classified in three different main types (Wilkinson, 2014): sedimentary-exhalative (SEDEX), Mississippi Valley-Type (MVT) and Irish-Type. Despite extensively studied, there are diverse hypotheses on the processes and geological settings under which these economically significant sediment-hosted deposits form.

The SEDEX mineralisation is regarded as a synsedimentary or syngenetic ore, e.g. precipitated at the same time of deposition of the host rock, or as early diagenetic deposit, typified by sulfide laminated textures and stratabound morphologies (Leach et al., 2005; 2010). The SEDEX mineralisation occurs in shales, carbonate rocks, calcareous and organic-rich siltstones, less commonly in sandstones and conglomerates, and is precipitated by infiltrated or connate seawater at temperatures in the range of 70-300 °C and salinities of 4-23 wt% NaCl eq. (Leach et al., 2004; 2010). SEDEX deposits generally form in intracontinental or failed rift settings (Large et al., 2005) or in rifted continental margins (Large, 1983; Lydon, 1983; 1996; Goodfellow et al., 1993).

https://doi.org/10.1180/mgm.2025.10124 Published online by Cambridge University Press

MVT ore deposits occur in dolostones and limestones with subordinate sandstones in carbonate-dominated sedimentary successions. MVT ores are defined as epigenetic, meaning that they form after the lithification of the host rock, because the mineralisation may replace the host carbonates and can fill primary and/or secondary porosity originated from dissolution or fracturing (Sangster, 1990; Leach and Sangster, 1993; Leach et al., 2005; 2010; Wilkinson, 2014). MVT mineralisation is related to connate bittern brines, commonly derived from seawater evaporation or dissolution of evaporites, with salinities of 13-28 wt% NaCl eq. and temperatures of 90-150 °C, lower than SEDEX (Leach et al., 2001; 2003; 2005; 2010). They are typically hosted in marine carbonate platform sequences in the foreland basin of orogenic belts (Bradley and Leach, 2003), although some MVT deposits occur at the margins of active extensional basins (e.g. Carboniferous of Pennines, UK; Hollis and Walkden, 2002; Devonian Lennard Shelf, Australia; Garven and Wallace, 2009).

The Irish-Type ores formed mainly as replacement of the host rocks or filling open veins and voids and were interpreted as epigenetic with a minor synsedimentary or syngenetic component (Boast et al., 1981; Taylor, 1984; Ashton et al., 1986; Anderson et al., 1998; Hitzman et al., 2002; Fusciardi et al., 2003; Lowther et al., 2003; Wilkinson, 2003; Wilkinson et al., 2005a). The Irish-Type mineralisation is hosted in the clay-free carbonate strata of mixed carbonate-siliciclastic successions in extensional continental margins (Wilkinson et al., 2003). These ores are precipitated by infiltrated and partially evaporated seawater at temperatures of 70-280 °C and salinities of 4-28 wt% NaCl eq. (Wilkinson et al., 2003; 2014; Wilkinson, 2010).

MVT and SEDEX are the two most important types of sediment-hosted Pb-Zn ores (Leach et al., 2010). The attribution of specific deposits to one of the proposed categories, however, may be subjective and controversial. According to Leach et al. (2010), some SEDEX ores replaced sediments during early or burial diagenesis, while some MVT ores exhibit laminated textures and formed in early diagenetic settings, in disagreement with the accepted epigenetic definition. According to the classification criteria reported in Leach et al. (2005), the Irish-Type deposits have more in common with SEDEX than MVT ores and are considered a transitional category that can help understanding the diversity of styles and processes of mineralisation (Leach et al., 2010).

Due to the low concentration of metals and fluorine in marine carbonate host rocks, it is supposed that ore metals are transported by fluids. Transport models able to explain the formation of Pb-Zn, fluorite and baryte ore deposits are summarised by Paradis et al. (2007) and Wilkinson (2014) and comprise: (1) flushing of basinal fluids from uplifted areas towards less elevated areas, with recharge of meteoric waters in the elevated areas

https://doi.org/10.1180/mgm.2025.10124 Published online by Cambridge University Press

(MVT and Irish-Type deposits; Garven and Freeze, 1984; Garven, 1985; Bethke and Marshak, 1990; Garven and Raffensperger, 1997; Wilkinson, 2014); (2) basin-derived fluids from sediment compaction migrating laterally and vertically (MVT deposits; Jackson and Beales, 1967; Sharp, 1978; Richardson and Holland, 1979; Cathles and Smith, 1983; Oliver, 1986; Hollis and Walkden, 2002; Wilkinson, 2014); and (3) deep convection circulation of hydrothermal brines driven by gradients in density, temperature and salinity (SEDEX, MVT and Irish-Type deposits; Morrow, 1998; Nelson et al., 2002; Wilkinson, 2014).

Various models have been proposed to explain the precipitation of Pb-Zn sulfide, fluorite and baryte ores: (1) a mixing model between a fluid enriched in base metals and a fluid enriched in H_2S, with sulfide precipitation triggered by pH variations and drop in temperature (Beales and Jackson, 1966; Anderson, 1975; Anderson and Macqueen, 1982; Sverjensky, 1984; Adams et al., 2000); (2) the transport of base metals and H_2S in the same fluid with sulfide deriving from both bacterial and thermochemical sulfate reduction in the presence of organic matter and evaporites (Anderson, 1975; Beales, 1975); and (3) reduced sulfur transported in the same fluid in which base metals are contained, with sulfide formation driven by cooling water temperature, pH variations and loss of volatiles (Anderson, 1975; Anderson and Macqueen, 1982; Sverjensky, 1984; 1986). Fluorite may precipitate by predominantly basin-derived hydrothermal fluids because of similarities between the composition of fluid inclusions in fluorites and that of nearby sedimentary basinal brines (Richardson and Holland, 1979).

A regionally-extensive Pb-Zn sulfides, fluorite and baryte metallogenic province developed from the central Alpine area to the Dinarides (Brigo and Omenetto, 1979a; Palinkas et al., 2008; Melcher et al., 2023): these deposits are named “Alpine-Type” and are considered as a sub-class of MVT ores (Leach et al., 2003; 2005). Melcher et al. (2023) provided the most recent review about the Alpine-Type deposits, which consist of stratabound, less commonly stratiform, mineralisation mainly hosted in Anisian to Norian (Middle to Upper Triassic) platform carbonates of the Austroalpine and Southern Alps domains (Leach et al., 2003; 2005; Melcher et al., 2023). Alpine-Type ores display finely laminated rhythmites and colloform sphalerite textures and precipitated at <100-200°C by reduced acidic brines with salinities of 10-30 wt% NaCl eq. (Melcher et al., 2023). Two contrasting genetic models were proposed for the genesis of the Alpine-Type mineralisation, mostly based on textural and sedimentological evidence, which led to different timings of ore formation: (1) early, probably syngenetic, during or shortly after the deposition of the host carbonate rocks (e.g. Schulz, 1964; Maucher and Schneider, 1967; Sangster, 1976; Brigo et al., 1977; Cerny, 1989; Schroll et al., 2006; Kucha

https://doi.org/10.1180/mgm.2025.10124 Published online by Cambridge University Press

et al., 2010); and (2) epigenetic in burial settings, Late Triassic, Jurassic or post-Jurassic in age (e.g. Jicha, 1951; Brigo et al., 1977; Zeeh et al., 1998; Kuhlemann et al., 2001; Leach et al., 2003; Mondillo et al., 2020). However, Brigo and Omenetto (1979b) and Brusca et al. (2010) envisaged a mixed model consisting of a minor syngenetic mineralising episode preceding the main epigenetic mineralisation.

Melcher et al. (2023) emphasized the issue of the ore timing both due to the challenges of the recently employed radiometric age determination and due to the scarcity of geochronological data for most of the ore districts. Reasonable precision was obtained from Rb-Sr isotopic geochronology on sphalerite by Henjes-Kunst et al. (2017) in the Bleiberg area (Austria; Table 1), although provided contrasting ages: (1) 225 ± 2.1 Ma in the Raibl Group (Carnian), fitting the late Carnian age of the host rocks and pointing to a syngenetic model; and (2) 201 ± 1.6 Ma in the Wetterstein Formation (Ladinian-Carnian), corresponding to the Triassic-Jurassic boundary and post-dating sedimentation by 24 M.y., in favour of the epigenetic model (Kuhlemann et al., 2001; Leach et al., 2003; Melcher et al. 2010; 2023). Other geochronological data derive from the first in-situ U-Pb radiometric age determination of hydrothermal carbonates from the Gorno mining district by Giorno et al. (2022). The authors obtained ages of 227.1 ± 17.9 Ma for the pre-sulfide saddle dolomite and 226.9 ± 5.3 Ma for the post-ore calcite, implying that the mineralisation at Gorno might have occurred shortly after the deposition of the lower Carnian host rocks.

Geological setting

The Dossena orebodies are located in the western part of the Gorno mining district, which extends for 30 km E-W and 20 km N-S in the Orobic Alps (Lombardy, northern Italy; Fig. 1). The Orobic Alps are part of the Central Southern Alps (Fig. 1a,b), which represent a non-metamorphic south-verging thrust and fold belt (Laubscher, 1985; Schmid et al., 1989; Dal Piaz et al., 2003), bordered to the North by the Periadriatic Lineament (Fig. 1c). In the context of the Alpine Orogeny, the deformation of the Southern Alps domain started in the Late Cretaceous (Bertotti et al., 1993; Berra and Carminati, 2010; Zanchetta et al., 2012).

The Lombardy Basin sedimentary succession (Fig. 2) developed on the metamorphic Variscan basement starting, at the base, with Permian conglomerates (Basal Conglomerates), volcanic and volcaniclastic deposits (Monte Cabianca Vulcanite) and a continental alluvial-lacustrine siliciclastic unit (Pizzo del Diavolo Formation), accumulated in a strike-slip basin and followed by fluvial deposits (Verrucano Lombardo; Casati and Gnaccolini, 1967; Cadel et al., 1996; Cassinis et al., 2011; Jadoul et al., 2012). The overlying Lower Triassic siliciclastic

https://doi.org/10.1180/mgm.2025.10124 Published online by Cambridge University Press

coastal and carbonate deposits represent transgressive marine facies (Servino Formation; Cassinis, 1968; Sciunnach et al., 1996). A subsequent regressive phase was documented between the Olenekian and Anisian (Lower-Middle Triassic) with deposition of evaporites in sabkha settings (Carniola di Bovegno), followed by shallow subtidal limestones and peritidal dolomites (Angolo Limestone and Camorelli Limestone; Assereto and Casati, 1965; Jadoul and Rossi, 1982; Berra et al., 2005), overlain by transgressive, ammonoid-bearing marlstone and limestone of the Prezzo Limestone (Assereto and Casati, 1965; Jadoul et al., 2012). Upper Anisian to Ladinian (Middle Triassic) high-relief carbonate platforms (Esino Limestone), characterised by steep slopes with resedimented breccias (Berra, 2007), interfingered basinward with nodular cherty limestones (Buchenstein Formation) and volcaniclastic sandstones (Wengen Formation). Towards the end of the Ladinian, in the westernmost portion of the Lombardy Basin, the carbonate platform prograded on the adjacent basinal facies sealing the intraplatform basin (Jadoul et al., 1992c; Berra, 2007; Berra and Carminati, 2010; Cassinis et al., 2011; Jadoul et al., 2012). Close to the Ladinian-Carnian boundary (Middle-Upper Triassic), a major relative sea-level fall caused the subaerial exposure of the Esino Limestone platform top, resulting in the deposition of the Calcare Rosso supratidal facies with tepees, paleosols and karst breccias (Assereto and Kendall, 1977; Assereto et al., 1977; Berra and Carminati, 2010; Jadoul et al., 2012). Differently, in the easternmost portion of the Lombardy Basin, the Ladinian basinal succession (Pratotondo Limestone) was covered by Carnian black shales and siltstones (Lozio Shale; Rossetti, 1967; Balini et al., 2000; Berra, 2007; Berra et al., 2011), which draped the platform slope to basin, after the subaerial exposure marked by the Calcare Rosso (Berra, 2007). In the northern sector of the Lombardy Basin, Carnian shallow-water peritidal carbonates (Breno Formation; Assereto and Casati, 1965; Berra and Jadoul, 2002), laterally adjacent to lagoonal facies (Calcare Metallifero Bergamasco and Gorno Formation; Gnaccolini, 1986; Casati and Gnaccolini, 1967; Assereto et al., 1977) interfingered with progradational delta deposits (Val Sabbia Sandstones; Gnaccolini, 1983; 1988; Garzanti, 1985; Gnaccolini and Jadoul, 1988; Garzanti et al., 1995). The upper contact of the Breno Formation with the 10-20 m thick Calcare Metallifero Bergamasco is generally sharp and marked by the occurrence of abundant dark marlstones (Assereto et al., 1977). A subaerial exposure at the top of the Calcare Metallifero Bergamasco locally resulted in the total erosion of this lithostratigraphic unit up to the top of the Breno Formation (Assereto et al., 1977). The basal unit of the Gorno Formation at the contact with the underlying Calcare Metallifero Bergamasco consists of 10 m thick laminated black shales and dark marlstones, labelled as “Basal Tongue” of the Gorno Formation (Fig. 2; Assereto and Casati, 1965; Assereto et al., 1977). The Carnian

https://doi.org/10.1180/mgm.2025.10124 Published online by Cambridge University Press

lithostratigraphic units from the Breno to Gorno formations display a trend of increasing accommodation and siliciclastic input, as a result of extensional tectonics and climate change towards more humid conditions (Assereto et al., 1977; Marinelli et al., 1980; Garzanti, 1985). Volcanic tuff layers, deposited at the top of the Esino Limestone and within the Breno Formation, document a Ladinian-Carnian volcanic activity, possibly linked to a back-arc geodynamic regime (Garzanti and Jadoul, 1985; Cassinis et al., 2008, 2011; Jadoul et al., 2012). The Val Sabbia Sandstones volcaniclastic litharenites confirm the erosion of Ladinian-Carnian volcanic edifices located to the south (Garzanti, 1985; Cassinis et al., 2008). The overlying mixed siliciclastic and dolomitic deposits with evaporites accumulated in sabkha, arid climate supratidal settings (San Giovanni Bianco Formation; Garzanti et al., 1995), followed by calcareous breccias (Castro Sebino Formation; Jadoul et al., 1992a) and the early-dolomitized Dolomia Principale carbonate platform (upper Carnian-Norian). Norian extensional tectonics resulted in the formation of intraplatform basins, characterised by the deposition of dark, well-bedded basinal dolostones and limestones (Dolomie Zonate and Zorzino Limestone; Bonamini and Berra, 2022), sealed by the uppermost Norian Riva di Solto Shales (Jadoul, 1986; Jadoul et al., 1992b; Cassinis, 2011; Trombetta, 2013). The Triassic-Jurassic extensional tectonics, which led to the opening of the Alpine Tethys Ocean between Toarcian and Bajocian (Winterer and Bosellini, 1981; Manatschal and Bernoulli, 1998; Trombetta, 2013), is considered either a single rifting event starting in the Norian (Bertotti et al., 1993) or a tectonic phase consisting of two different extensional pulses recorded in the Norian and in the Sinemurian-Pliensbachian, separated by a relatively quiescent phase in the latest Triassic-earliest Jurassic (Bernoulli et al., 1990; Berra and Carminati, 2010).

Lead-Zinc sulfide and fluorite ore deposits in the Lombardy Basin

Several Pb-Zn, fluorite and baryte mine districts were exploited in the Ladinian-Carnian carbonate succession of the Southern Alps in Lombardy (Figs 1d, 2), mainly hosted in the Esino Limestone, Breno Formation (BRE) and Calcare Metallifero Bergamasco (CMB) (Vachè, 1966; Assereto et al., 1977; Omenetto and Vailati, 1977; Rodeghiero et al., 1986; Mondillo et al., 2020; Giorno et al., 2022). Ores in historical mines are grouped on the basis of the association and abundance of the different exploited minerals (Fig. 1d): (1) Pb-Zn ores in the Pian dei Resinelli, Monte Arera/Val Vedra and Gorno/Oltre il Colle/Monte Trevasco/Val Riso areas (Omenetto, 1966); (2) dominant fluorite ores in the Paglio Pignolino/Dossena area (Assereto et al., 1977; Jadoul and Omenetto, 1980); (3) baryte ores in the Brembana Valley and (4) fluorite-baryte deposits with subordinate Pb-

https://doi.org/10.1180/mgm.2025.10124 Published online by Cambridge University Press

Zn ores in the Presolana area (Assereto et al., 1977; 1978; Brigo et al., 1977; Rodeghiero, 1977; Jadoul and Omenetto, 1980). Despite differences in the relative abundance of minerals, most of the ores occur as stratiform bodies, parallel to bedding, in the CMB at the contact with the overlying black shales of the "Basal Tongue" of the Gorno Formation (Fig. 2), or as discordant bodies within the BRE and CMB limestones (Omenetto, 1966; Vailati, 1966; Omenetto and Vailati, 1977). Assereto et al. (1977) provided detailed descriptions of the mineralisation in the Paglio Pignolino/Dossena area distinguishing lower, middle and upper orebodies on the basis of the stratigraphic position in the host rocks and ore morphology. The lower mineralisation consists of dominant sphalerite associated with minor galena, quartz, calcite and fluorite and occurs in ellipsoidal to spherical pockets stratigraphically positioned 50-60 m below the BRE upper boundary. The middle orebody fills discordant and subconcordant cavities located 30 m below the BRE upper boundary and consists of dominant fluorite with locally abundant sphalerite, subordinated galena, Cu-Sb-As sulfosalts, pyrite, marcasite and baryte associated with calcite, dolomite and quartz. Both the lower and middle mineralised bodies are interpreted as filling decimetre to metre-scale dissolution cavities due to the subaerial exposure of the upper CMB, commonly composing the "matrix" of collapse breccias (Assereto et al., 1977). The upper ore is stratiform and is located at the top of the CMB and in the lower part of the black shales constituting the basal tongue of the Gorno Formation. It consists mainly of fluorite, quartz, illite, calcite and rare sphalerite.

Several interpretations were proposed to explain the genesis of the Pb-Zn sulfide, fluorite and baryte ores and the associated carbonate phases in Lombardy (Table 1): (1) syngenetic mineralisation due to submarine exhalations related to the late Ladinian-Carnian volcanism (Vachè, 1966); (2) early diagenetic mineralisation (Assereto et al., 1977; Omenetto and Vailati, 1977); (3) Alpine-Type syngenetic to epigenetic mineralisation, with recrystallisation of the ore minerals at 3 km burial depths by hydrothermal fluids during the Early-Middle Jurassic rifting (Rodeghiero et al., 1986); (4) Alpine-Type mineralisation in deep burial settings by hydrothermal fluids linked to the Early-Middle Jurassic rifting (Mondillo et al., 2020); and (5) Alpine-Type mineralisation in shallow burial settings (tens to few hundreds of metres) by hydrothermal fluids related to the Triassic magmatism and prior to the Early Jurassic rifting phase (Giorno et al., 2022). Hence, the most recent studies (Mondillo et al., 2020; Giorno et al., 2022) propose that the Pb-Zn sulfide, fluorite and baryte ores in Lombardy were precipitated by hydrothermal fluids, implying that these fluids must have been hotter of at least 5-10 °C than the host rock (cf. hydrothermal fluid definitions by White, 1957; Machel and Lonnee, 2002; Davies and

https://doi.org/10.1180/mgm.2025.10124 Published online by Cambridge University Press

Smith, 2006).

Methods

Sampling and petrography

The ten analysed carbonate samples were collected from the lower Carnian BRE and CMB formations, cropping-out close to the main orebodies of the Dossena mines (Figs 1d, 2) between latitudes of 45.89583°N and 45.89938°N and longitudes from 9.68246°E to 9.68909°E. The detailed location of the collected samples of the BRE and CMB formations is provided in the supplementary material (Fig. S1; Table S1). In the collected specimens, ore minerals are disseminated within the host rock and occur in secondary vuggy porosity and fractures. Petrographic analysis was carried out on 17 thin sections (7 BRE; 10 CMB) using a Zeiss polarized light microscope equipped with a digital camera. Six of the 17 thin sections were cut at the standard thickness of 30 µm and polished with alumina paste, while 11 thin sections were cut at the thickness of about 100 µm and polished with diamond paste. Fourteen thin sections were partially stained with alizarin red-S and K-ferricyanide (Dickson, 1966). Cathodoluminescence (CL) analysis was performed on all the 17 thin sections with a Cambridge Image Technology Limited (CITL), model MK 5-2, operated at 10-16 kV accelerating voltage with a beam current between 200-400 µA and vacuum gauge 50-70 millitorr, at the Earth Sciences Department of the University of Milan.

Carbon and oxygen stable isotopes

Representative powder samples of the carbonate host rock and diagenetic phases were collected for stable C and O isotope ratio measurements from the same slabs from which the thin sections had been obtained. Slabs were previously cleaned with deionized waters, dried with compressed air and then sampled using a handheld low speed microdrill. A total of 30 powder samples were collected, 12 of the BRE (10 calcite, 2 dolomite) and 18 of the CMB (15 calcite, 3 dolomite). Due to the difficulty in separating the calcite cement phases during sampling and the presence of sub-millimetre wide fractures and voids, some calcites were sampled together and analysed as combined calcite cement phases. C and O stable isotope analyses were performed using an automated device for on-line isotope and molecular ratio determination of headspace samples (Gasbench II) and a Thermo Fisher Scientific Delta V Advantage continuous flow mass spectrometer at the Earth Sciences Department of the University of Milan. Carbonate powder samples of ~200 µg were weighed with a precision

https://doi.org/10.1180/mgm.2025.10124 Published online by Cambridge University Press

balance. The calcite powders were reacted with >99% orthophosphoric acid at 70 °C for an hour, while the dolomite powders for 8 hours at the same conditions. The C and O stable isotope compositions are expressed in the conventional delta notation calibrated to the Vienna Pee Dee Belemnite (V-PDB) scale by the international standards IAEA 603 and NBS-18 and by laboratory standards prepared from Carrara and Candoglia marbles. Analytical reproducibility for these analyses was better than ± 0.1‰ for both $\delta^{18}O$ and $\delta^{13}C$ values.

Accessory and trace element concentrations

Major and trace element concentrations were determined at the Geochemistry, Geochronology and Isotope Geology Laboratory of the Earth Sciences Department of the University of Milan by LA ICP-MS (Laser Ablation Inductively Coupled Plasma Mass Spectrometer) on two BRE and five CMB 100 µm thick polished thin sections. The instrument couples an Analyte Excite 193 nm ArF excimer laser microprobe system, equipped with an HelEx II volume sample chamber (Teledyne Cetac Technologies), to a single-collector quadrupole ICP-MS (iCAP RQ, Thermo-Fisher Scientific). The laser spot diameters used for these investigations were of 50, 65 and 110 µm, laser fluence was ~2 J/cm^2, and repetition rate 10 Hz. Helium was used as a carrier gas and its flow rate was set at 0.54 L/min in the sample chamber and 0.34 L/min in the HelEx II cup. He gas was combined with Ar gas before entering the ICP-MS. Each analysis consisted in the acquisition of 40 seconds of background signal, about 60 s of laser signal and 20 s of wash out time. Data reduction was carried out using the Glitter software package (Griffin et al., 2008). The signals of the following masses were acquired: ^{7}Li, ^{9}Be, ^{11}B, ^{25}Mg, ^{29}Si, ^{43}Ca, ^{44}Ca, ^{45}Sc, ^{49}Ti, ^{51}V, ^{53}Cr, ^{55}Mn, ^{57}Fe, ^{59}Co, ^{60}Ni, ^{65}Cu, ^{66}Zn, ^{75}As, ^{85}Rb, ^{88}Sr, ^{89}Y, ^{90}Zr, ^{93}Nb, ^{111}Cd, ^{121}Sb, ^{133}Cs, ^{137}Ba, ^{139}La, ^{140}Ce, ^{141}Pr, ^{146}Nd, ^{149}Sm, ^{151}Eu, ^{157}Gd, ^{159}Tb, ^{163}Dy, ^{89}Y, ^{165}Ho, ^{167}Er, ^{169}Tm, ^{173}Yb, ^{175}Lu, ^{177}Hf, ^{181}Ta, ^{182}W, ^{208}Pb, ^{232}Th and ^{238}U. The NIST-SRM 612 synthetic glass and ^{43}Ca were used as external and internal standards, respectively. Instrumental drift was monitored by repeated analysis of NIST-SRM 612 after every 15-20 unknowns. Data reduction was carried out assuming a concentration of CaO of 30.4 weight % for stoichiometric dolomite $(CaMgCO_3)_2$ and 56.0 weight % for calcite $CaCO_3$. Quality control of the analyses was achieved by analysing the USGS reference basalt glass BCR-2G. Accuracy was better than 7.5% except for ^{57}Fe (61%), ^{25}Mg (27%), ^{66}Zn (31%), ^{75}As (50%) and ^{111}Cd (45%), while precision was within σ (4%). During the second day of measurements, accuracy was better than 7.5% except for ^{11}B (23%), ^{25}Mg (28%), ^{49}Ti (24%), ^{57}Fe (63%), ^{66}Zn (31%), ^{75}As (60%), ^{90}Zr (20%), ^{111}Cd (48%), while precision was within σ (4%). Some carbonate

https://doi.org/10.1180/mgm.2025.10124 Published online by Cambridge University Press

phases were sampled in 2 or 3 spots to verify the consistency of the measurements.

The Rare Earth Elements + Yttrium (REEY) concentrations were normalised (subscript $_N$) to mean shale composition (subscript $_{SN}$) using PAAS (Post-Archean Australian Shale; McLennan, 1989) and to C-1 (volatile-free; Taylor and McLennan, 1981) carbonaceous chondrite (subscript $_{CN}$). REEY concentrations were also normalised to MuQ (Mud from Queensland), providing the present-day composition of alluvial sediments (Kamber et al., 2005) to monitor the discrepancies with PAAS- normalised REEY concentrations. The normalised ($REEY_N$) Nd/Yb_N and Pr/Yb_N ratios were calculated to monitor LREEs depletion with respect to HREEs, La/Sm_N was calculated to monitor the depletion of LREEs with respect to MREEs, while Dy/Yb_N was calculated to track the MREEs depletion with respect to HREEs. Yttrium (Y) was inserted among the REE between Dy and Ho according to its effective ionic radius. Y/Ho ratio was calculated in order to monitor detrital clastic contamination. The majority of geologic material (including all volcanic and siliciclastic sedimentary rocks) has near chondritic values of Y/Ho ratio (24-34), whereas present-day seawater is characterised by Y/Ho ratio >44 (Bau, 1996; Nozaki et al., 1997). Geometric Lanthanum, Cerium, Europium and Gadolinium anomalies, both shale- and chondrite-normalised, were calculated according to the geometric equations of Lawrence et al. (2006): $(La/La^*)_N = La_N/[Pr_N*(Pr_N/Nd_N)^2]$, $(Ce/Ce^*)_N = Ce_N/[Pr_N*(Pr_N/Nd_N)]$, $(Eu/Eu^*)_N = Eu_N/[Sm_N^{(2)}*Tb_N^{(1/3)}]$ and $(Gd/Gd^*)_N = Gd/[(Tb_N^{(2)}*Sm_N)^{(1/3)}]$, as recommended by Barrat et al. (2023) and Barrat and Bayon (2024). Lanthanum and Cerium anomalies normalised to both shale and chondrite were identified also using the graph and formulas for $(Pr/Pr^*)_N = Pr_N/[(0.5*Ce_N)+(0.5*Nd_N)]$ and $(Ce/Ce^*)_N = Ce_N/[(0.5*La_N)+(0.5*Pr_N)]$ proposed by Bau and Dulski (1996). The results from this study were compared with Navarro-Ciurana et al. (2023) diagram that allows distinguishing between present-day marine and hydrothermal fluids. The shale- and chondrite-normalised Europium anomaly was also calculated as $(Eu/Eu^*)_N = Eu_N/[(0.67*Sm_N)+(0.33*Tb_N)]$, according to Bau and Dulski (1996). As for the drilled powders for C and O stable isotopes, in some cases it was difficult to sample individual carbonate phases because of their occurrence within voids and fractures of limited size, of a few 100s µm to few millimetres; hence, the measured values are presented as analysis of mixed phases (e.g. BRE Cal 2 + 3 + 4, BRE Cal 6 + 7).

Results

Diagenetic features of the Breno Formation (BRE)

The analysed BRE depositional texture (Cal 0) consists of peloidal skeletal packstone-wackestone with gastropods and bivalves (Fig. 3a-d), dull red luminescent in CL (Fig. 3b), in which localised dispersed framboidal

https://doi.org/10.1180/mgm.2025.10124 Published online by Cambridge University Press

pyrite are identifiable (Fig. 3c). The diagenetic features of the BRE are summarised in Table 2 and showed in Figs 3, 4, 5.

Cal 1 sparite fills primary voids and mouldic porosity after former aragonitic mollusc shells (Fig. 3a-d), while Cal 2 + 3 + 4 sparites occlude mm-size vugs (Fig. 3e,f). Cal 0, Cal 1 and Cal 2 + 3 + 4 are cross-cut by fractures filled by Dol 1 saddle dolomite (Figs 3g,h, 4a-h) overlain by Cal 5 equant calcite (Figs 3g, 4a,b), which may occur also in the intercrystal porosity between Dol 1 domains (Fig. 4c-e). Cal 6 sparite to microsparite fills fractures crossing Cal 0 to Cal 5 phases (Figs 3a,b, 4a,c,d,g, 5c,d), partially replacing Dol 1 saddle dolomite (Fig. 4b,f,h) and sometimes resulting in breccia textures (Fig. 5a). Sphalerite, galena and fluorite mineralisation occurs between Cal 6 crystals (Fig. 5b,c), while another generation of sparite labelled as Cal 7 cuts across Dol 1 saddle dolomite (Figs 4e-h, 5f) and Cal 6 sparite (Figs 4e-h, 5b), overlies fluorite crystals (Fig. 5e) and locally results in breccia textures made of mm- to cm-size angular fragments of Cal 0 (Fig. 5g,h). Euhedral hexagonal bipyramidal quartz overlies Cal 7 sparite (Figs 4e-h, 5b, e-h), together affected by the formation of stylolite 1 (Figs 3d, 5h). The cross-cutting relationships of the 10 different diagenetic phases recognised in the BRE allowed identifying their relative timing, which is illustrated in Fig. 6a. The phases, from the earliest to the latest, are: Cal 1, Cal 2, Cal 3, Cal 4, Dol 1 saddle dolomite, Cal 5, Cal 6, sphalerite, galena and fluorite, Cal 7 and euhedral hexagonal bipyramidal quartz, followed by stylolite 1.

Diagenetic features of the Calcare Metallifero Bergamasco (CMB)

The CMB Cal 0 host rock in Dossena consists of peloidal packstone with benthic foraminifers and peloidal skeletal packstone with bivalves (Fig. 7a-c), exhibiting bright orange luminescence (Fig. 7d) and pervasive recrystallisation of micrite into microsparite (20-50 µm). Cal 0 host rock is also affected by replacement by a fabric destructive mosaic of luminescent anhedral dolomicrosparite Dol 1 (Fig. 7e-f) and silicification (Figs 7g,h, 8a,b). Eight different diagenetic phases were recognised on Cal 0 host rock, described in Table 3 and displayed in Figs 7, 8, 9.

Cal 1 sparite fills interparticle, vug and mouldic porosity and is crossed by a first set of stylolites (Fig. 7a-d). Fractures filled by Dol 2 saddle dolomite and by Cal 2 sparite (Figs 7h, 8a,b,d,e,h, 9a-d, S2c,d) cross-cut silicified portions of Cal 0 host rock (Figs 7h, 8a,b, 9c) and stylolites of the second set (9a-c). Crystals of Dol 2 are also sparse in the silicified Cal 0 (Fig. S2a,b), while Cal 2 fills the intercrystal voids between Dol 2 saddle dolomite

https://doi.org/10.1180/mgm.2025.10124 Published online by Cambridge University Press

(Fig. 8c,d). Sphalerite, galena and fluorite formed in fractures and secondary voids within Cal 2 (Figs 9b,d-f, S2e-h). In between Cal 2 crystals, fragments of bituminous shales (100 μm – 1 mm) with framboidal pyrite frequently occur (Fig. 9d). Cal 3 equant sparite fills fractures cutting through all the other diagenetic phases (Figs 7c,e, 8e,f, 9e-h, S2f), partially replaces Dol 2 saddle dolomite (Figs 8c,d,g,h, S2c,d), Cal 2 sparite (Fig. 8g,h), Cal 0 host rock (Fig. 7c,d) and overlies fluorite crystals (Fig. S2g,h). Equant quartz mosaic fills the intercrystal porosity between sphalerite, galena and fluorite (Fig. S2e) and is followed by a third set of stylolites (Fig. 9e). The petrographic relationships between the CMB diagenetic phases allowed the identification of the paragenesis, which is displayed in Fig. 6b and that consists of: Cal 1, stylolite 1, Dol 1, silicification by microquartz and chalcedony, stylolite 2, Dol 2 saddle dolomite, Cal 2, sphalerite, galena and fluorite, Cal 3, quartz mosaic and stylolite 3.

Carbon and oxygen stable isotope signature

The $\delta^{13}C$ values of the BRE carbonate phases range from 0.3‰ to 1.9‰, whereas $\delta^{18}O$ are between -11.7‰ and -5.5‰ (Fig. 10a; Table S2). The BRE peloidal skeletal packstone-wackestone (Cal 0) and Cal 1 blocky sparite show $\delta^{13}C$ values of 0.7-1.0‰ and $\delta^{18}O$ between -6.9‰ and -5.9‰. Cal 2 + 3 + 4 blocky sparite cements have cumulative $\delta^{13}C$ values of 0.7-0.8‰ and $\delta^{18}O$ varying between -6.4‰ and -5.5‰. $\delta^{13}C$ of Dol 1 saddle dolomite cement ranges between 0.3% and 1.9‰, while $\delta^{18}O$ is comprised between -11.7‰ and -10.1‰. The $\delta^{13}C$ values of Cal 6 + 7 fracture filling sparite vary between 0.8‰ and 1.7‰, while $\delta^{18}O$ ranges between -8.5‰ and -7.1‰.

Regarding the CMB carbonate phases (Fig. 10b; Table S3), the recrystallised Cal 0 packstone and Cal 1 blocky microsparite to sparite display $\delta^{13}C$ values between 0.1‰ and 0.7‰ and $\delta^{18}O$ of -12.1‰ and -8.4‰. Dol 1 replacive dolomicrosparite has $\delta^{13}C$ of 1.5‰ and $\delta^{18}O$ of -11.6‰. Dol 2 fracture filling saddle dolomite $\delta^{13}C$ ranges between 0.1‰ and 1.3‰, while $\delta^{18}O$ values are -11.7‰ and -11.0‰. Cal 2 fracture filling prismatic to equant calcite exhibits $\delta^{13}C$ values of 0.8-1.0‰, while $\delta^{18}O$ varies between -9.0‰ and -7.5‰. Cal 3 fracture sparite displays $\delta^{13}C$ and $\delta^{18}O$ values that are comprised between -0.2‰ and 1.3‰ and -10.1‰ and -7.8‰, respectively.

Trace element concentrations

The results of trace element concentrations, including REEY, are summarised in Tables 4a,b,c,d and integrated

https://doi.org/10.1180/mgm.2025.10124 Published online by Cambridge University Press

with the shale- and chondrite-normalised ratios to identify trends and anomalies in the different BRE carbonate phases. The BRE diagenetic phases are characterised by relatively low contents of ∑REE that, on average, range between 0.207 ppm for Cal 2 + 3 + 4 sparite and 3.10 ppm for Dol 1 saddle dolomite. The $REEY_{SN}$ patterns show (Fig. 11): (1) slightly LREEs enriched with positive Eu_{SN} anomaly for Cal 0 host rock; (2) bell-shaped with enrichment in HREEs for Cal 2 + 3 + 4 with negative Ce_{SN} and Eu_{SN} anomalies, but this result is based on only one analysis; (3) concave to convex upwards HREEs depleted patterns for Dol 1 saddle dolomite with no to slightly positive Eu_{SN} and Ce_{SN} anomalies; (4) bell-shaped for Cal 6 + 7 sparite to microsparite with positive Eu_{SN} anomalies. Cal 5 shows heterogeneous $REEY_{SN}$ patterns: (i) slightly HREEs enriched with negative Ce_{SN} anomaly; (ii) depleted in HREEs with positive Eu_{SN} anomaly; (iii) HREEs depleted with positive Ce_{SN} anomaly and wide ranges of Nd/Yb_{SN} (from not detected to 2.6), Ce/Ce^*_{SN} (0.6-1.2), La/La^*_{SN} (0.9-1.3) and Eu/Eu^*_{SN} (1.3-1.5). $REEY_{CN}$ patterns are shown in Fig. S3 and are all strongly enriched in LREEs, with more pronounced negative Eu_{CN} anomalies in Cal 2 + 3 + 4, Dol 1 and Cal 5.

The concentrations of trace elements, including REEY, the shale- and chondrite-normalised REEY ratios and anomalies of the CMB carbonate phases are summarised in Tables 5a,b,c,d. Cal 3 has the highest ∑REE content (23.7 ppm), whereas the saddle dolomite (Dol 2) shows the lowest ∑REE (2.97 ppm). The average $REEY_{SN}$ patterns are (Fig. 12): (1) HREEs depleted in Cal 0 host rock with positive Eu_{SN} anomaly; (2) concave to convex upwards HREEs depleted patterns for Dol 2 saddle dolomite, with no Ce_{SN} anomaly and $Eu/Eu^*_{SN} > 1$; (3) bell-shaped with negative to positive Ce_{SN} anomaly, positive Eu_{SN} and Y anomalies for Cal 2 sparite. Dol 1 replacive dolomicrosparite shows two different $REEY_{SN}$ patterns, one flat and the other LREEs enriched (Nd/Yb_{SN} = 0.7-2.2, Eu/Eu^*_{SN} = 1.1-1.6, Y/Ho = 22.9-39.5). Cal 3 fracture filling sparite (Nd/Yb_{SN} = 0.5-11.9, Eu/Eu^*_{SN} = 1.0-1.5, Y/Ho = 21.8-35.1) displays two different $REEY_{SN}$ patterns, one slightly depleted in LREEs and HREEs with respect to MREEs (Cal 3a) and the other convex-concave upwards (Cal 3b; Fig. 12). All the shale-normalised CMB carbonate phases display a positive Eu_{SN} anomaly (Fig. 12) whereas, when chondrite-normalised, the CMB carbonates are characterised by HREEs depletion and negative Eu_{CN} anomalies except for Cal 2, which exhibits positive Eu_{CN} and Y anomalies (Fig. S4). Trace elements besides REEY (Tables 4a,b, 5a,b, S4, S5) display fairly variable distribution across the different carbonate phases, marking the subsequent paragenetic stages, especially those identified in the CMB. Most of the trace elements were measured in all analysed spots and are recorded in all diagenetic phases, while a few elements were discontinuously detected above detection limits and/or were abundant only in some phases. The trace elements detected in all the investigated carbonate

https://doi.org/10.1180/mgm.2025.10124 Published online by Cambridge University Press

phases are Li, B, Sc, Ti, V, Mn, Co, Ni, Cu, Zn, Sr, Zr, Ba, Pb and U, while Sb, As and Rb are commonly not detected. The selected diagrams (Figs 13, S5, S6; Tables 4a,b, 5a,b, S4, S5) illustrate the distribution of and the relationships between some of these accessory elements in the BRE and CMB carbonate phases (Fig. 6). The CMB carbonate phases exhibit higher contents in trace elements and metals than those of the BRE (e.g. CMB Cal 2 and Cal 3 in Zn, U, Cu and Sc with respect to BRE Cal 5 and Cal 6 + 7). As shown in Tables 4a,b, 5a,b, S4, S5 and in most of the diagrams in Figs 13, S5, S6, both BRE and CMB unmineralised Cal 0 host rocks tend to be enriched in Zn, Pb, Cu and U with respect to the saddle dolomites and to the pre- and post-ore sparites.

Discussion

The diagenetic features and their relative timing, identified in the two studied carbonate lithostratigraphic units, are summarised in the paragenetic sequences of Fig. 6. The BRE and CMB carbonate rocks (Cal 0) contain the same mineralisation (sphalerite, galena, fluorite), some equivalent (Cal 1, Dol 1-Dol 2 saddle dolomites, BRE Cal 6 - CMB Cal 2 pre-mineralisation sparites, BRE Cal 7 - CMB Cal 3 post-mineralisation sparites) and some different diagenetic phases (BRE: Cal 2 + 3 + 4, Cal 5; CMB: Dol 1, silicification and quartz mosaic). Furthermore, BRE studied samples exhibit one set of stylolites, while the CMB three. The different paragenetic sequences may be explained by some missed observations, by the diverse carbonate cements preceding and post-dating the fracture-filling saddle dolomite and by the lack in the BRE samples of the early dolomitization (Dol 1) identified in the CMB samples. Almost all the BRE and CMB investigated carbonate phases exhibit ∑REE contents (BRE: 0.207-3.10 ppm, CMB: 2.97-23.7 ppm; Tables 4a, 5a) higher than the expected concentrations for open marine, pristine carbonates (ca. 0.75 ppm; Nothdurft et al., 2004). The different $REEY_{SN}$ and $REEY_{CN}$ patterns observed in the equivalent CMB and BRE carbonate phases are possibly the result of greater proportion of siliciclastic sediment and organic matter embedded in the CMB limestone facies (Fig. 9d).

Diagenetic and geochemical features pre-saddle dolomite

Regarding the host rocks, the luminescence in CL, $\delta^{18}O$ values and REEY shale-normalised trends demonstrate that the original fabric and geochemical marine signature are not preserved in either BRE or CMB Cal 0 (cf. Tucker and Wright, 1990; Machel et al., 1991; Della Porta et al., 2015; Swart, 2015). Dull red luminescence of BRE Cal 0 and bright orange luminescence of CMB Cal 0 reflect their Fe and Mn contents, respectively (BRE: Fe = 261 – 289 ppm, Mn = 218 – 702 ppm; CMB: Fe = 189 – 552 ppm, Mn = 278 – 1109 ppm; Tables 4a, 5a),

https://doi.org/10.1180/mgm.2025.10124 Published online by Cambridge University Press

indicative of carbonate recrystallisation in reducing conditions during burial. Fe and Mn concentrations in carbonate minerals reflect the redox conditions of the fluid from which they precipitated. In fact, in oxidizing conditions, Fe and Mn do not substitute Ca^{2+} in the calcite or dolomite crystals, resulting in non-luminescent carbonates, while calcites and dolomites precipitated in reducing conditions are progressively enriched in Mn^{2+} and Fe^{2+} that respond differently to CL, activating bright luminescence and quenching to dull luminescence, respectively (Tucker and Wright, 1990; Machel et al., 1991; Hiatt and Pufahl, 2014). However, some studies questioned this general rule demonstrating that Mn may be incorporated in carbonates precipitating from slightly acidic fluids in oxidizing conditions, if buffered by hydrocarbons and H_2S dispersed in the system (Meyers, 1989; Spangenberg et al., 1999; Tavazzani et al., 2024). The $\delta^{18}O$ values of BRE and CMB Cal 0 (Fig. 10a,b; Tables S2, S3) are lower than those expected for Upper Triassic marine pristine carbonates (-0.5 to -4.0‰; Veizer et al., 1999), confirming recrystallisation of the original marine carbonate by diagenetic fluids at higher temperature than seawater. The CMB Cal 0 exhibits two different sets of $\delta^{18}O$ values, matching either the dolomite phases (-12.1 to -11.8‰) or the void and fracture filling sparites (-9.4 to -8.4‰), suggesting isotopic resetting by different fluid/rock interactions. For this reason, the involvement of meteoric fluids in the recrystallisation of Cal 0 cannot be completely ruled out, notwithstanding the high positive $\delta^{13}C$ values are in the range expected for Upper Triassic marine pristine carbonates (0.0-3.0‰; Veizer et al., 1999). The $\delta^{13}C$ values are uniform for all the identified carbonate phases, suggesting that the Dissolved Inorganic Carbon (DIC) was inherited from the host limestones. The Y/Ho ratios in both BRE and CMB Cal 0 (Tables 4c, 5c) fall between the Upper Continental Crust (27.5; Taylor and McLennan, 1985; 26.2; Kamber et al., 2005) and seawater (44-74; Bau, 1996), providing additional evidence for recrystallisation and geochemical resetting by diagenetic fluids. Moreover, the $REEY_{SN}$ patterns are flat to convex upwards for BRE Cal 0 and depleted in HREE for CMB Cal 0 (Fig. 14), diverging from the expected seawater shale-normalised patterns (Alibo and Nozaki, 1999; Della Porta et al., 2015) and suggesting possible contamination by siliciclastic sediment. Both BRE and CMB Cal 0 exhibit LREEs enrichment, which can be explained with siliciclastic contamination (Nothdurft et al., 2004; Spangenberg and Herlec, 2006), or with the interaction with volcaniclastic rocks (Haq Siddiqui et al., 2015) or, alternatively, related to hydrothermal influence (Barrat et al., 2000; Frimmel, 2009). Positive correlations (correlation coefficient r^2 = 0.6-1.0) between Si and Rb, Nb, Cs, Hf, Zr, Th, Ba, V, Co, Ni, Cu, Ti contents in both the Cal 0 samples (except for Si-Cu and Si-V in BRE Cal 0 and for Si-Nb, Si-Hf and Si-Co in the CMB Cal 0 which are <0.6; Figs S7, S8; Tables S6, S7) support siliciclastic contamination (Spangenberg and Herlec, 2006).

https://doi.org/10.1180/mgm.2025.10124 Published online by Cambridge University Press

Previous studies demonstrated that 1-2% (Nothdurft et al., 2004) and 2-5% (Della Porta et al., 2015) in weight of siliciclastic sediment are sufficient to alter the pristine $REEY_{SN}$ pattern of marine carbonates and to mask elemental anomalies, resulting in flat and uniform $REEY_{SN}$ patterns. In fact, also La_{SN} and Ce_{SN} anomalies close to 1 are the possible consequence of siliciclastic contamination (Nothdurft et al., 2004; Bolhar and Van Kranendonk, 2007; Della Porta et al., 2015). In the Lower Carnian succession of the Southern Alps, siliciclastic sediment input has been linked to the overlying prograding delta of the volcaniclastic Val Sabbia Sandstones (Gnaccolini, 1983; Garzanti, 1985) and/or to the Carnian Pluvial Event (Simms and Ruffel, 1989, 2018; Preto et al., 2010; 2013; Arche and Lopez-Gomez, 2014; Dal Corso et al., 2015; 2018). The $REEY_{CN}$ patterns of both Cal 0 resemble those of the Upper Continental Crust (Figs S3, S4; Taylor and McLennan, 1981), providing additional evidence for siliciclastic contamination (e.g. Liang and Jones, 2021 about the Mesoproterozoic Gaoyuzhuang Formation in North China). The Cal 0 slightly negative to positive Ce_{SN} anomaly associated with positive Eu_{SN} anomaly (Tables 4d, 5d) could also be related to marine signature overprinted by burial and/or hydrothermal fluids. In fact, most of Cal 0 samples (Fig. 15a) fall within the field of hydrothermal carbonates proposed by Navarro-Ciurana et al. (2023), identified on the basis of the relationships between $(Pr/Pr^*)_{SN}$ and $(Ce/Ce^*)_{SN}$ calculated according to the Bau and Dulski (1996) equations. Empirical and experimental studies suggest that LREEs and Eu are more soluble in high temperature Cl-rich fluids (Michard et al., 1983; James et al., 1995; Douville et al., 1999; Bau and Alexander, 2009; Migdisov et al., 2009; Bau et al., 2010; Craddock et al., 2010; Williams-Jones et al., 2012; Johannessen et al., 2017; Kareem et al., 2021), strongly affecting the Eu_{SN} anomaly. In fact, under acidic conditions, positive Eu_{SN} anomalies can only develop in carbonates precipitated by high-temperature (>250 °C) fluids cooled below 200-250 °C (Sverjensky, 1984; Bau, 1991; Bilal, 1991; Bau and Möller, 1992). In contrast, Eu_{SN} anomalies will be diminished or absent in low temperature fluids that did not exceed 200 °C (Danielson et al., 1992; Alexander et al., 2008) or at long distances from the heating source area (Bau et al., 1996; Johannessen et al., 2017; Kareem et al., 2021).

BRE and CMB Cal 1 non-luminescent sparites might represent meteoric phreatic or marine burial cements precipitated from an oxygenated fluid (Melim et al., 1995); the second interpretation is preferred due to the lack of evidence of meteoric dissolution and vadose diagenetic features (e.g. dogtooth, meniscus, pendant cements). In BRE, the Cal 2 + 3 + 4 sparites represent a progressive burial cement succession filling primary and mouldic porosity, with oscillation of redox conditions and enrichment in Mn^{2+}, as inferred from crystal fabric and CL (Choquette and James, 1987; Machel et al., 1991; Hiatt and Pufahl, 2014; Della Porta et al., 2015; Liu et

https://doi.org/10.1180/mgm.2025.10124 Published online by Cambridge University Press

al., 2022). This cement sequence was not identified in the overlying CMB samples. Instead, distinctive of the CMB samples is the replacive dolomicrosparite Dol 1, not identified in the underlying BRE. The petrographic features and geochemical data of CMB Dol 1 suggest an early dolomitization event overprinted by burial or hydrothermal fluids (Fig. 15a; Navarro-Ciurana et al., 2023). Dol 1 REEY concentrations seem partly inherited by the replaced Cal 0 (Table 5c), including possible siliciclastic contamination (Spangenberg and Herlec, 2006).

Diagenetic and geochemical features of the pre-mineralisation stage

Dol 1 (BRE) and Dol 2 (CMB) fracture-filling saddle dolomites exhibit undulose extinction which, according to previous studies (Searl, 1989; Moore, 1994; Lavoie and Chi, 2001; Spencer et al., 2004; Davies and Packard, 2004; Davies and Smith, 2006), may be related to anomalous incorporation of Ca ions with respect to Mg in the crystalline structure, resulting in distorted crystal lattices. Saddle dolomite is interpreted to form at temperatures higher than 60 °C (Radke and Mathis, 1980; Warren, 2000; Rameil, 2008), probably in a temperature range of 100-180 °C to more than 235 °C (Davies and Smith, 2006), in agreement with the measured low $\delta^{18}O$ values in this study (BRE: Dol 1 = -11.7 to -10.1‰; CMB Dol 2 = -11.7 to -11.0‰; Fig. 10a,b; Tables S2, S3). The zoned luminescence of both saddle dolomites suggests variations in redox conditions and in Mn/Fe ratios of the precipitating fluid (Machel et al., 1991). The spotted bright orange portions identified in Dol 2 CMB saddle dolomite are the result of the partial replacement by Cal 3 sparite (Figs 8d,h, S2d), as similarly documented in other case studies by Machel (1987) and Sirat et al. (2016). The replacement of CMB Dol 2 by Cal 3 is confirmed by the overlap of the geochemical parameters of these two phases (Fig. 15a-e), despite their large difference in ∑REE contents (Dol 2: 1.37-4.97 ppm; Cal 3: 1.22-92.9 ppm; Table 5a). The LREEs enriched patterns and positive Eu_{SN} anomalies identified in the saddle dolomites (Figs 11, 12, 14) are indicative of hydrothermal fluids (Barrat et al., 2000), while a Ce_{SN} negative anomaly is generally absent in carbonates precipitated from acid hydrothermal fluids (Frimmel, 2009). The $REEY_{CN}$ patterns of both saddle dolomites are similar to those of the Upper Continental Crust (Figs S3, S4; Taylor and McLennan, 1981) as well as the Y/Ho ratios (27.5; Taylor and McLennan, 1985; 26.2; Kamber et al., 2005). Similar $REEY_{CN}$ patterns were reported for saddle dolomites in the Middle Devonian Western Canada Sedimentary Basin by Qing and Mountjoy (1994) and interpreted as possibly deriving from the interaction of the precipitating hydrothermal fluid with crustal rocks (siliciclastic deposits and crystalline basement; Qing and Mountjoy, 1992). Hence, on the basis of the petrographic and geochemical data obtained in this study, BRE Dol 1 and CMB Dol 2 saddle

https://doi.org/10.1180/mgm.2025.10124 Published online by Cambridge University Press

dolomites are reasonably the same carbonate phase and seem to be equivalent to other saddle dolomites identified in the Lombardy Basin carbonate units: (1) D3 saddle dolomite in the Ladinian Esino Limestone and BRE described by Hou et al. (2016), interpreted as precipitated in mid to deep burial settings by hydrothermal fluids; (2) Dol 2 by Mondillo et al. (2020) reported as the product of hydrothermal fluids in deep burial settings; and (3) Dol 2 identified in the CMB by Giorno et al. (2022), precipitated by hydrothermal fluids in shallow burial settings. Despite the occurrence in different mining districts of the Lombardy Basin, saddle dolomites always pre-date the mineralisation. As indicated by the homogenization temperatures of 111 ± 14 °C (D3; Hou et al., 2016) and 111 ± 13 °C (Dol 2; Giorno et al., 2022), saddle dolomites seem to be precipitated by similar fluids at similar temperatures. Geochemical data obtained in this study, integrated with the findings from published literature, agree with the interpretation of BRE and CMB saddle dolomites as precipitated by low temperature (<200 °C) hydrothermal fluids.

The fracture-filling hydrothermal saddle dolomites (Dol 1 in BRE and Dol 2 in CMB) are followed by Cal 5 and Cal 6 in BRE and Cal 2 in CMB, preceding the mineralisation. In BRE, Cal 5 equant sparite overlies Dol 1 saddle dolomite and precipitated in the Dol 1 intercrystal porosity. The average Cal 5 $REEY_{SN}$ pattern suggests precipitation by burial basinal brines (bell-shaped average $REEY_{SN}$ pattern; Fig. 14) but the heterogeneity of this calcite REEY data might derive from mixed sampling and contamination from different sparite phases. This is demonstrated in Fig. 4a,b by fractures filled by Cal 6 cross-cutting Cal 5, explaining also the wide standard deviations (SD) in Tables 4a,b,c,d.

Cal 6 in BRE and Cal 2 in CMB fracture-filling calcites represent an equivalent diagenetic phase preceding the mineralisation. They were precipitated in reducing conditions by high temperature fluids (i.e. with respect to seawater) as inferred from the bright luminescence and O stable isotope composition, respectively, outside the range expected for marine pristine carbonates (Fig. 10a,b; Tables S2, S3). In fact, these sparites show common petrographic and CL features, $\delta^{13}C$ and $\delta^{18}O$ values (Fig. 10a,b; Tables S2, S3) and similar $REEY_{SN}$ patterns (Figs 11, 12, 14), despite the mixing between BRE Cal 6 and Cal 7 during geochemical sampling. The MREEs enrichment identified in Cal 6 + 7 and Cal 2 may be due to more stable complexing of MREEs with CO_3^{2-} and OH^- in alkaline solutions (Möller et al., 1998; Schwinn and Markl, 2005) and it is commonly observed in burial diagenetic calcite (Shields and Webb, 2004; Rachidi et al., 2009; Della Porta et al., 2015; Gong et al., 2021) and in diagenetic calcite associated with hydrothermal fluorite (Mondillo et al., 2016; Castorina et al., 2020). The $REEY_{CN}$ patterns and Y/Ho ratios of BRE Cal 6 + 7 and CMB Cal 2 resemble those of seawater with

https://doi.org/10.1180/mgm.2025.10124 Published online by Cambridge University Press

negative Ce_{CN} anomaly (Figs 14, S3, S4; Goldberg et al., 1963; Hogdahl, 1967; Hogdahl et al., 1968; De Baar et al., 1985a; German et al., 1990; Mitra et al., 1994; Bau, 1996; Alibo and Nozaki, 1999; Van Kranendonk et al., 2003; Luong et al., 2018) and those of low temperature (<200 °C) hydrothermal fluids (Bau and Dulski, 1999), supporting the interpretations that they were precipitated by hydrothermal fluids that interacted with connate seawater in primary porosity. In fact, Cal 6 + 7 and Cal 2 sparites plot both in the fields of seawater and hydrothermal fluids in Fig. 15a, based on Navarro-Ciurana et al. (2023), and were possibly precipitated by fluids derived by the mixing of marine water (Y/Ho ratio; negative to positive Ce_{SN} anomaly) and hydrothermal fluids (positive Eu_{SN} anomaly), as reported for similar diagenetic calcites (Bau and Dulski, 1999; Douville et al., 2002; Edmonds and German, 2004; Sylvestre et al., 2017; Castorina et al., 2020; Aftabi et al., 2021; Li et al., 2021; Navarro-Ciurana et al., 2023). A further confirmation for the ore precipitation at temperatures lower than 200 °C is corroborated by the S isotope analyses on sphalerite from the Gorno mine district by Fruth and Maucher (1966). These authors obtained $\delta^{34}S$ values comprised between -9.8‰ and 3.8‰, suggesting the predominance of sulfur related to thermochemical sulfate reduction (Melcher et al., 2023) which, according to the literature, is a process occurring in a temperature range of 90-200 °C (100-140°C, Machel, 1987, 2001; 90-175°C, Krouse et al., 1988; 150-200°C, Heydari and Moore, 1989; 140-180°C, Worden et al., 1995).

Diagenetic and geochemical features of the post-mineralisation stage

BRE Cal 7 might correspond to the CMB fracture-filling Cal 3 sparite, on the basis of the similar petrographic features and of the occurrence in the paragenetic sequences after sphalerite, galena and fluorite mineralisation. In BRE, the Cal 7 distinctive geochemical signature was affected by the mixing with Cal 6 and the interpretation is then provided focussing on post-mineralisation Cal 3 identified in the CMB. CMB Cal 3 displays two distinct $REEY_{SN}$ patterns (Figs 12, 14), consistent with different diagenetic fluids. Cal 3 has the highest ∑REE contents and is strongly enriched in LREEs (Tables 5a,c). This feature can be explained with the possible interaction of the precipitating fluid with crustal rocks (Nothdurft et al., 2004), as confirmed by the $REEY_{CN}$ patterns, which resemble those of the Upper Continental Crust (Fig. 14; Taylor and McLennan, 1981), the Y/Ho ratios (27.5; Taylor and McLennan, 1985; 26.2; Kamber et al., 2005), negative to slightly positive Ce_{SN} and no to positive Eu_{SN} anomalies (Table 5d). Hence, Cal 3 may result from the mixing between basinal fluids, which interacted with siliciclastic rocks and/or metamorphic basement, and hydrothermal fluids (Fig. 15a; Navarro-Ciurana et al., 2023). Cal 3 geochemical data (i.e. stable isotopes, $REEY_{SN}$ patterns, Fe, Mn and Sr

https://doi.org/10.1180/mgm.2025.10124 Published online by Cambridge University Press

contents) overlap with Cal 0 suggesting that Cal 3 fluids possibly caused Cal 0 recrystallisation. The post-mineralisation fracture-filling sparites (BRE Cal 7 and CMB Cal 3) might correspond to other post-ore sparites identified in other mining areas in the Lombardy Basin such as: (1) C3 calcite cement identified by Hou et al. (2016) in the Esino Limestone and BRE, interpreted as precipitated in mid to deep burial settings at temperature of 112 ± 9 °C from fluid inclusions; (2) Cal by Mondillo et al. (2020), interpreted as precipitated by hydrothermal fluids in deep burial settings; and (3) Cal 2 identified in the CMB by Giorno et al. (2022), reported as precipitated by hydrothermal fluids in shallow burial settings.

Carbonate trace elements and possible origin for metals and hydrothermal fluids

For the Gorno mining district, previous studies suggested a contribution of metals deriving from the interaction of the mineralising fluids with weathered siliciclastic and/or volcaniclastic rocks accumulated in the basin (Assereto et al., 1977; Omenetto and Vailati, 1977; Mondillo et al., 2020) and with the metamorphic basement (Garzanti and Jadoul, 1985). The latter provenance was considered compatible with the Pb isotope data obtained by Köppel and Schroll (1988) for the various Triassic Pb-Zn ore deposits in the Southern Alps, including Gorno. Köppel and Schroll (1988) envisaged basement feldspars as contributors of Pb, Ba and Tl, although the latter is characteristic of Salafossa in the Dolomites (Brusca et al., 2010) and Raibl in the Julian Alps (Barago et al., 2023). Assereto et al. (1977) and Omenetto and Vailati (1977) proposed that the Lower Carnian Gorno Formation and Val Sabbia Sandstones (Mondillo et al., 2020), which overlie the BRE and CMB, may be possible metal sources for the mineralisation. Alternatively, the upper Permian fluvial deposits of the Verrucano Lombardo, which underlie the Triassic carbonate sequence in the Lombardy Basin (Fig. 2) and of which the Variscan basement, Collio volcanic rocks and siliciclastic sediments are major contributors, could have been another source of metals.

Besides REEY, other trace elements provide information about the possible influence of the mineralising fluids on the compositions of the carbonate phases. Elements such as Li, B, Sc, Ti, V, Co, Ni, Cu, Zn, Zr, Ba, Pb, U, Sb, As and Rb are easily mobilised by fluids and may be incorporated in newly-formed hydrothermal minerals (e.g. sulfides, sulfates, fluorides) crystallising within carbonate host rocks. Trace elements such as Sr and Mn are common in carbonates but they are not exclusive proxies for hydrothermal fluids because of their different affinity for calcite and dolomite crystal structures (Rimstid et al., 1998) and because of the control by the redox conditions for the incorporation of Mn in carbonates (Machel et al., 1991). Silica is an accessory element

https://doi.org/10.1180/mgm.2025.10124 Published online by Cambridge University Press

always detected in BRE and CMB carbonates with fluctuating concentrations (Tables 4a, 5a) and may be derived from siliciclastic contamination, biogenic origin, hydrothermal quartz and common micro-fragments of sulfidic black shales enclosed in the mineralisation (Fig. 9d). Most of the other analysed elements are variably concentrated in the carbonate phases, which may be the result of burial diagenesis and/or the mineralising process.

The relatively low contents of several trace elements in the saddle dolomites and in the sparites preceding and post-dating the mineralisation might result from cations sequestration from the metal-rich mineralising fluid through the precipitation of sulfides, sulfosalts, baryte and fluorite. The trace element concentrations measured in CMB Cal 2 and Cal 3 are considered more reliable in characterising the precipitating fluids pre- and post-dating the mineralisation with respect to BRE Cal 6 + 7, which could not be separated during sampling. The bright luminescent CMB Cal 2 calcite, which predates the mineralisation, marks a decrease in the concentration of zinc and lead (Fig. 13a,b), the calcophile metals related to sphalerite and galena precipitation. The decrease in Zn and Pb contents may be related to their propensity to precipitate as sulfides in the presence of H_2S (Saito et al., 2003), possibly confirming the first influx of reduced sulfur and the ore mineral precipitation after Cal 2 sparite.

Ba, Cu, Sb and As (Figs 13c,d, S5, S6) are components of baryte and Cu-rich sulfosalts (tetrahedrite and bournonite), which are ore-related hydrothermal minerals intergrown within sulfides and, as Zn and Pb, show a gradual decrease from saddle dolomite to Cal 2 pre- and Cal 3 post-ore. Jarvis et al. (1989) and Dulski (1994) envisaged that Ba contents might interfere on the LA ICP-MS determination of Eu^{151} and Eu^{153} abundances due to their similar mass/charge ratios to those of BaO and $BaOH^+$ species, resulting in apparent positive Eu_N anomalies and leaving doubts on a possible hydrothermal influence. Plots of Ba and Eu contents are widely used to unravel the possible relationships between these two elements and a linear correlation is commonly interpreted as an indicator of apparent interference (Shields and Stille, 2001; Yang et al., 2007; Wang et al., 2012; Ling et al., 2013; Chang et al., 2019; Stacey et al., 2022). In this study, plots of Eu/Eu^*_{SN} and Ba contents in ppm of all the investigated BRE and CMB carbonate phases show negative correlations (Fig. S9a,b; Tables S8, S9), implying that the positive Eu anomalies identified are effectively attributable to hydrothermal influence (Stacey et al., 2022). Co and Ni contents might be related to pyrite, which is an accessory mineral in the ore but that frequently occurs as bacteriogenic framboidal micro-spheres in the host rock and within the bituminous shale fragments enclosed between the pre-mineralisation sparite and the mineralisation (Figs 3c, 9d). These

https://doi.org/10.1180/mgm.2025.10124 Published online by Cambridge University Press

clasts of sulfidic black shales within the sphalerite-galena mineralisation might also explain the occasional and relative high contents in Ti, V and Zr (Figs 13e, S5c,d, S6c,d), possibly related to very fine-grained accessory heavy minerals (rutile, zircon). Compared to the sulfide-related metals, the redox-sensitive uranium appears to behave differently in the metal-rich CMB, where the pre-mineralisation Cal 2 is relatively U-enriched (Fig. 13f). Hydrothermal U uptake by calcite is a known phenomenon in a wide range of temperature and redox conditions (Gabitov et al., 2021 and references therein). Ore-related Cal 2 might have fixed some redox-sensitive U because of the presence of sulfidic black shale fragments typical of reducing conditions (Migdisov et al. 2018). Alternatively, the relative U enrichment in Cal 2 might be dependent on U transported as fluoride complex in the mineralising fluid, resulting in the concomitant fluorite precipitation with sulfides (Xing et al., 2019). Fluorine in the ore fluid might also be responsible for the geochemical signature of scandium of the analysed CMB diagenetic carbonates. In fact, Sc, which is geochemically affine to Mg-bearing minerals, is higher in Dol 2 saddle dolomite (mean values of 0.130 ppm) roughly similar in Cal 2 pre-mineralisation calcite (mean values of 0.127 ppm) and depleted in Cal 3 post-mineralisation sparite (mean values of 1.05 ppm; Fig. 13g). Although recent experiments tested the high stability of chloride and hydroxide complexes in the hydrothermal transport of Sc (Wang et al., 2023), ionic fluorine has been proven as particularly efficient in mobilizing Sc both in laboratory tests (Gramaccioli et al., 2000) and in Sc-enriched hydrothermal deposits, where F-rich minerals occur (Williams-Jones and Vasyukova, 2018; Hreus et al., 2021). The similar geochemical signatures of the post-mineralisation calcites with those of the ore-related carbonates might reflect the pre- and largely post-ore "hydrothermal alteration" typically observed within large, long-lived exhalative ore systems (Goodfellow and Lydon, 2007).

However, proposals for a syngenetic mineralisation due to submarine exhalations (Gorno; Vachè, 1966) are not supported by the findings of this study. The fracture-filling saddle dolomite and following ore minerals cross-cut voids occluded by progressive burial cements in already lithified host rocks, affected by compaction and pressure solution that produced the stylolites, which commonly form in carbonate units at burial depths greater than 300 metres (Dunnington, 1967; Nicolaides and Wallace, 1997; Machel, 2004; Ebner et al., 2008; Beaudoin et al., 2016). These paragenetic relationships point to an epigenetic mineralisation. Considering the burial history curve for the Brembana Valley (Fig. 16; modified after Berra and Carminati, 2010), the study area BRE and CMB successions might have reached burial depths of at least 300 metres in the Early Carnian, after the deposition of the Val Sabbia Sandstones and Gorno Formation (Fig. 2). Nevertheless, burial depths greater

https://doi.org/10.1180/mgm.2025.10124 Published online by Cambridge University Press

than 300 metres for the onset of stylolitisation cannot be discarded, implying also that the mineralisation could be precipitated in later stages, such as the Triassic-Jurassic boundary as proposed by several authors (Zeeh et al., 1998; Kuhlemann et al., 2001; Leach et al., 2003; Melcher et al., 2010; 2023; Henjes-Kunst et al., 2017; Mondillo et al., 2020). Hence, the ore precipitation in Dossena might have started from few hundreds of metres depth, in at least shallow burial settings.

To unravel the possible source for hydrothermal fluids, Y/Ho ratios of the carbonate phases might be helpful. The Y/Ho values of the different investigated BRE and CMB ore-associated carbonate phases range between 26.9 and 71.3 (Tables 4c, 5c), suggesting also a possible contribution from magmatic hydrothermal fluids (Y/Ho = 23-33; Bau, 1996), similarly to what reported by Duan et al. (2017) in the Qingchengzi ore field, China. This is also in agreement with the fluid inclusion data obtained in the carbonate phases of the Esino Limestone and Breno Formation by Hou et al. (2016), who inferred a potential contribution from volcanic activity to the parental diagenetic fluids of dolomites and calcites. In the study area, possible triggers for hydrothermal circulation may have been the Ladinian-Carnian volcanism coupled with extensional and strike-slip tectonics (Cassinis et al., 2008; Giorno et al., 2022), the Norian extensional faults (Bernoulli et al., 1990; Bertotti et al., 1993; Berra and Carminati, 2010) and the Early Jurassic rifting (Garzanti and Jadoul, 1985; Rodeghiero et al., 1986; Mondillo et al., 2020), which are all possible sources for magmatic hydrothermal fluids. The predominance of fluorite in the Dossena deposits may be a further confirmation for the involvement of magmatic fluids in the ore mineral precipitation. In fact, fluid enrichment in F may have possibly been caused by the interaction of the hydrothermal fluids with a cooling magma body and related exsolved volatiles, as similarly reported in Bakos et al. (1972) and Hein et al. (1990). Nonetheless, the contribution from magmatic fluids should be treated carefully considering that: (1) the fluid Y/Ho ratio is strongly dependent on the composition of the rocks with which interacted and on the water-rock ratio (Bau, 1996; Takahashi et al., 2002); and that (2) except for volcanic tuff layers within the BRE (Vachè, 1966), the studied lithostratigraphic units lack evidence of volcanic activity (e.g. magmatic intrusions).

Conclusions

The Lower Carnian Breno Formation (BRE) and the Calcare Metallifero Bergamasco (CMB) are two superimposed carbonate lithostratigraphic units in the Lombardy Basin, hosting Pb-Zn sulfide and fluorite mineralisation associated with fracture-filling saddle dolomite and calcite cements.

Detailed petrographic study allowed identifying 10 diagenetic phases for the BRE (Cal 1, Cal 2, Cal 3, Cal 4, Dol

https://doi.org/10.1180/mgm.2025.10124 Published online by Cambridge University Press

1 saddle dolomite, Cal 5, Cal 6, sphalerite-galena-fluorite, Cal 7, euhedral hexagonal bipyramidal quartz) and 8 diagenetic phases for the CMB (Cal 1, Dol 1 replacive dolomicrosparite of Cal 0, silicification of Cal 0, Dol 2 saddle dolomite, Cal 2, sphalerite-galena-fluorite, Cal 3, quartz mosaic), documenting a complex diagenetic history.

Oxygen stable isotope data of all the investigated carbonate phases are outside the range of values expected for marine pristine carbonates proposed in the literature, consistent with recrystallisation and/or precipitation by high temperature fluids with respect to seawater. The Dissolved Inorganic Carbon (DIC) was inherited by marine carbonate rocks, as suggested by the homogeneous $\delta^{13}C$ values for all the analysed carbonate phases. Stable isotopes, trace element data and REEY elemental anomalies support a precipitation of the carbonate phases preceding and post-dating (saddle dolomites and sparites) the hydrothermal epigenetic mineralisation, as well as the recrystallisation and overprinting of the original marine carbonate host rocks, attributable to low temperature (<200 °C) hydrothermal fluids influenced by basinal brines and seawater. The decrease in concentration of calcophile elements (e.g. Zn, Pb) coincides with the crystallisation of pre-ore bright sparites (BRE Cal 6 and CMB Cal 2), possibly confirming the first influx in the system of reduced sulfur and the consequent ore minerals precipitation following this diagenetic calcite phase.

Fractures filled by saddle dolomite and the pre-ore calcite cross-cut the already lithified Cal 0 host rock, voids occluded by progressive generations of burial cements and stylolites, allowing to set the epigenetic ore precipitation following the onset of pressure solution in at least shallow burial settings, starting from depths of few hundreds of metres. This interpretation agrees with the findings of Giorno et al. (2022) for the Gorno mining district. The possible metal source for the mineralising fluids may be the overlying Upper Carnian siliciclastic Gorno Formation and volcaniclastic Val Sabbia Sandstones or, alternatively, the upper Permian Verrucano Lombardo, which underlies the Triassic carbonate succession and consists of siliciclastic and volcaniclastic fluvial deposits reworking the Variscan metamorphic basement and lower Permian volcanic rocks.

Acknowledgements

The authors are grateful to the Università degli Studi di Milano laboratory staff Matteo Pegoraro for the thin section preparation, Elena Ferrari for the C and O stable isotope analysis and Gianluca Sessa for the LA ICP-MS investigation. The editor Roger Mitchell, the associate editor Jason Harvey, Lorenzo Tavazzani and two other

https://doi.org/10.1180/mgm.2025.10124 Published online by Cambridge University Press

anonymous reviewers are thanked for their valuable comments, which have noticeably improved the quality of the manuscript. This work benefits funding from the Italian Ministry of University and Research (MUR) - Progetti Dipartimenti di Eccellenza. The MUR PRIN2022 grants to M.T. (No. 2022X2EZTN) and to F.B. (No. 2022APF9M2) are also acknowledged.

Competing interests

The author(s) declare none.

Author contributions

Niccolò Coccia - Conceptualization, Methodology, Field work, Writing - original draft, Data curation, Writing - review and editing. **Giovanna Della Porta** - Conceptualization, Methodology, Field work, Writing - original draft, Data curation, Writing - review and editing. **Fabrizio Berra** - Conceptualization, Field work, Writing - review and editing. **Marilena Moroni** - Methodology, Data curation, Writing - review and editing. **Massimo Tiepolo** - Methodology, Review and editing.

Supplementary material

Electronic supplementary material is available to authorised users.

References

Adams J.J., Rostron B.J. and Mendoza C.A. (2000) Evidence for two-fluid mixing at Pine Point, Northwest Territories. Journal of Geochemical Exploration, 69-70, 103-108, https://doi.org/10.1016/S0375-6742(00)00014-5.

Aftabi A., Atapour H., Mohseni S. and Babaki A. (2021) Geochemical discrimination among different types of banded iron formations (BIFs): A comparative review. Ore Geology Reviews, 136, 104244, https://doi.org/10.1016/j.oregeorev.2021.104244.

Alexander B.W., Bau M., Andersson P. and Dulski P. (2008) Continentally-derived solutes in shallow Archean seawater: rare earth element and Nd isotope evidence in iron formation from the 2.9 Ga Pongola Supergroup, South Africa. Geochimica et Cosmochimica Acta, 72, 378-394, https://doi.org/10.1016/j.gca.2007.10.028.

https://doi.org/10.1180/mgm.2025.10124 Published online by Cambridge University Press

Alibo D.S. and Nozaki Y. (1999) Rare earth elements in seawater: particle association, shale normalization, and Ce oxidation. Geochimica et Cosmochimica Acta, 63 (3-4), 363-372, https://doi.org/10.1016/S0016-7037(98)00279-8.

Anderson G.M. and Macqueen R.W. (1982) Ore deposit models - 6. Mississippi Valley-type lead-zinc deposits. Geoscience Canada, 9, 108-117.

Anderson I.K., Ashton J.H., Boyce A.J., Fallick A.E. and Russell M.J. (1998) Ore depositional processes in the Navan Zn + Pb deposit, Ireland. Economic Geology, 93, 535-563, https://doi.org/10.2113/gsecongeo.93.5.535.

Appold M.S. and Garven G. (2000) Reactive flow models of ore formation in the Southeast Missouri district. Economic Geology, 95, 1605-1626, doi:10.2113 / gsecongeo.95.8.1605.

Arche A. and Lopez-Gomez J. (2014) The Carnian Pluvial Event in Western Europe: New data from Iberia and correlation with the Western Neotethys and Eastern North America–NW Africa regions. Earth-Sciences Reviews, 128, 196-231, https://doi.org/10.1016/j.earscirev.2013.10.012.

Ashton J.H., Downing D.T. and Finlay S. (1986) The geology of the Navan Zn-Pb orebody. Pp. 243-280 in: *Geology and Genesis of Mineral Deposits in Ireland* (C.J. Andrew, R.W.A. Crowe, S. Finlay, W.M. Pennell and J. Pyne, editors), Irish Association for Economic Geology, Dublin.

Assereto R. and Casati P. (1965) Revisione della stratigrafia permo-triassica della Val Camonica meridionale (Lombardia). Rivista Italiana di Paleontologia e Stratigrafia, 71, 999-1097.

Assereto R., Jadoul F. and Omenetto P. (1977) Stratigrafia e metallogenesi del settore occidentale del distretto a Pb, Zn, fluorite e barite di Gorno (Alpi Bergamasche). Rivista Italiana di Paleontologia e Stratigrafia, 83(3), 395-532.

Assereto R. and Kendall C.G.S.T.C. (1977) Nature, origin and classification of peritidal tepee structures and relative breccias. Sedimentology, 24, 153-210, https://doi.org/10.1111/j.1365-3091.1977.tb00254.x.

Bakos F., Brondi A. and Perna G. (1972) The age of mineral deposits in the Permian volcanites of Trentino-Alto Adige (Northern Italy). Proc. 2nd ISMIDA, Geologija, 15(1), 181-194.

Balini M., Germani D., Nicora A. and Rizzi E. (2000) Ladinian/Carnian ammonoids and conodonts from the classic Schilpario-Pizzo Camino area (Lombardy): revaluation of the biostratigraphic support to chronostratigraphy and paleogeography. Rivista Italiana di Paleontologia e Stratigrafia, 106, 19-58, 10.13130/2039-4942/5389.

Barago N., Pavoni E., Floreani F., Crosera M., Adami G., Lenaz D. and Covelli S. (2023) Hydrogeochemistry of

https://doi.org/10.1180/mgm.2025.10124 Published online by Cambridge University Press

thallium and other potentially toxic elements in neutral mine drainage at the decommissioned Pb-Zn Raibl mine (Eastern Alps, Italy). Journal of Geochemical Exploration, 245, 107129, https://doi.org/10.1016/j.gexplo.2022.107129.

Barrat J.A., Boulègue J., Tiercelin J.J. and Lesourd M. (2000) Strontium isotopes and rare earth element geochemistry of hydrothermal carbonate deposits from Lake Tanganyika, East Africa. Geochimica et Cosmochimica Acta, 64, 287-298, https://doi.org/10.1016/S0016-7037(99)00294-X.

Barrat J.A., Bayon G. and Lalonde S. (2023) Calculation of cerium and lanthanum anomalies in geological and environmental samples. Chemical Geology, 615, 121202, https://doi.org/10.1016/j.chemgeo.2022.121202.

Barrat J.A. and Bayon G. (2024) Practical guidelines for representing and interpreting rare earth abundances in environmental and biological studies. Chemosphere, 352, 141487, https://doi.org/10.1016/j.chemosphere.2024.141487.

Bau M. (1991) Rare-earth element mobility during hydrothermal and metamorphic fluid-rock interaction and the significance of the oxidation state of europium. Chemical Geology, 93, 219-230, https://doi.org/10.1016/0009-2541(91)90115-8.

Bau M. and Möller P. (1992) Rare earth element fractionation in metamorphogenic hydrothermal calcite, magnesite and siderite. Mineralogy and Petrology, 45, 231-246, http://dx.doi. org/10.1007/BF01163114.

Bau M. and Dulski P. (1996) Distribution of yttrium and rare-earth elements in the Penge and Kuruman iron-formations, Transvaal Supergroup, South Africa. Precambrian Research, 79, 37-55, https://doi.org/10.1016/0301-9268(95)00087-9.

Bau M. (1996) Controls on the fractionation of isovalent trace elements in magmatic and aqueous systems: evidence from Y/Ho, Zr/Hf, and lanthanide tetrad effect. Contributions to Mineralogy and Petrology, 123, 323-333. https://doi.org/10.1007/s004100050159.

Bau M., Koschinsky A., Dulski P. and Hein J.R. (1996) Comparison of the partitioning behaviours of yttrium, rare earth elements, and titanium between hydrogenetic marine ferromanganese crusts and seawater. Geochimica et Cosmochimica Acta, 60(10), 1709-1725, https://doi.org/10.1016/0016-7037(96)00063-4.

Bau M. and Dulski P. (1999) Comparing yttrium and rare earths in hydrothermal fluids from the Mid-Atlantic Ridge: implications for Y and REE behaviour during near-vent mixing and for the YrHo ratio of Proterozoic seawater. Chemical Geology, 155, 77-90, https://doi.org/10.1016/S0009-2541(98)00142-9.

Bau M. and Alexander B.W. (2009) Distribution of high field strength elements (Y, Zr, REE, Hf, Ta, Th, U) in

https://doi.org/10.1180/mgm.2025.10124 Published online by Cambridge University Press

adjacent magnetite and chert bands and in reference standards FeR-3 and FeR-4 from the Temagami iron-formation, Canada, and the redox level of the Neoarchean Ocean. Precambrian Research, 174, 337-346, https://doi.org/10.1016/j.precamres.2009.08.007.

Bau M., Balan S., Schmidt K. and Koschinsky A. (2010) Rare earth elements in mussel shells of the Mytilidae family as tracers for hidden and fossil high-temperature hydrothermal systems. Earth and Planetary Science Letters, 299, 310-316, https://doi.org/10.1016/j.epsl.2010.09.011.

Beales F.W. and Jackson S.A. (1966) Precipitation of lead-zinc ores in carbonate reservoirs as illustrated by Pine Point ore field, Canada. Journal of Mining and Metallurgy, section B, 75, 278-285.

Beales F.W. (1975) Precipitation mechanisms for Mississippi Valley-type ore deposits. Economic Geology, 70, 943-948, https://doi.org/10.2113/gsecongeo.70.5.943.

Beaudoin N., Koehn D., Lacombe O., Lecouty A., Billi A., Aharonov E. and Parlangeau C. (2016) Fingerprinting stress: Stylolite and calcite twinning paleopiezometry revealing the complexity of progressive stress patterns during folding - The case of the Monte Nero anticline in the Apennines, Italy. Tectonics, 35, 1687-1712, https://doi.org/10.1002/2016TC004128.

Berra F. and Jadoul F. (2002) Sedimentological and paleontological evidences of a Mid Carnian transgression in the Western Southern Alps (S. Giovanni B. Fm. Lombardy, Italy): stratigraphic and paleogeographic implications. Rivista Italiana di Paleontologia e Stratigrafia, 108, 119-131, https://hdl.handle.net/2434/52783.

Berra F., Rettori R. and Bassi D. (2005) Recovery of carbonate platform production in the Lombardy Basin during the Anisian: paleoecological significance and constrain on paleogeographic evolution. Facies, 50, 615-621, https://doi.org/10.1007/s10347-004-0043-4.

Berra F. (2007) Sedimentation in shallow to deep water carbonate environments across a sequence boundary: ejects of a fall in sea level on the evolution of a carbonate system (Ladinian-Carnian, eastern Lombardy, Italy). Sedimentology, 54, 721-735, https://doi.org/10.1111/j.1365-3091.2006.00850.x.

Berra F. and Carminati E. (2010) Subsidence history from a backstripping analysis of the Permo-Mesozoic succession of the Central Southern Alps (Northern Italy). Basin Research, 22, 952-975, https://doi.org/10.1111/j.1365-2117.2009.00453.x.

Berra F., Jadoul F., Binda M. and Lanfranchi A. (2011) Large-scale progradation, demise and rebirth of a high-relief carbonate platform (Triassic, Lombardy Southern Alps, Italy). Sedimentary Geology, 239, 48-63, 10.1016/j.sedgeo.2011.05.002.

https://doi.org/10.1180/mgm.2025.10124 Published online by Cambridge University Press

Bertotti G., Picotti V., Bernoulli D. and Castellarin A. (1993) From rifting to drifting: tectonic evolution of the South Alpine upper crust from Triassic to Early Cretaceous. Sedimentary Geology, 86, 53-76, https://doi.org/10.1016/0037-0738(93)90133-P.

Bethke C.M. and Marshak S. (1990) Brine migration across North America - the plate tectonics of groundwater. Annual Reviews of Earth and Planetary Sciences, 18, 287-315, https://doi.org/10.1146/annurev.ea.18.050190.001443.

Bertrandsson Erlandsson V., Wallner D., Ellmies R., Raith J.G. and Melcher F. (2022) Trace element composition of base metal sulfides from the sediment-hosted Dolostone Ore Formation (DOF) Cusingle bondCo deposit in northwestern Namibia: Implications for ore genesis. Journal of Geochemical Exploration, 243, 107105, https://doi.org/10.1016/j.gexplo.2022.107105.

Bilal B.A. (1991) Thermodynamic study of Eu^{3+}/Eu^{2+} redox reaction in aqueous solutions at elevated temperatures and pressures by means of cyclic voltammetry. Zeitschrift für Naturforschung A, 46, 1108-1116, https://doi.org/10.1515/zna-1991-1216.

Boast A.M., Coleman M.L. and Halls C. (1981) Textural and stable isotopic evidence for the genesis of the Tynagh base metal deposit, Ireland. Economic Geology, 76, 27-55, https://doi.org/10.2113/gsecongeo.76.1.27.

Bolhar R. and Van Kranendonk M.J. (2007) A non-marine depositional setting for the northern Fortescue Group, Pilbara Craton, inferred from trace element geochemistry of stromatolitic carbonates. Precambrian Research, 155, 229-250, https://doi.org/10.1016/j.precamres.2007.02.002.

Bonamini E. and Berra F. (2022) Resedimented limestones in fault-controlled basins (Zorzino Limestone, Southern Alps, Norian, Italy): Facies types and depositional model. Sedimentary Geology, 431, 106106, https://doi.org/10.1016/j.sedgeo.2022.106106.

Bradley D.C. and Leach D.L. (2003) Tectonic controls of Mississippi Valley-type lead zinc mineralization in orogenic forelands. Mineralium Deposita, 38, 652-667, https://doi.org/10.1007/s00126-003-0355-2.

Brigo L., Kostelka L., Omenetto P., Schneider H.J., Schroll E., Schulz O. and Štrucl I. (1977) Comparative reflections on four Alpine Pb-Zn deposits. Pp. 273-293 in: *Time and Strata-Bound Ore Deposits* (D.D. Klemm and H.J. Schneider, editors), Springer, Berlin, https://doi.org/10.1007/978-3-642-66806-7_18.

Brigo L. and Omenetto P. (1979a) Metallogenese der Italienischen Ostalpen. Verhandlungen der Geologischen Bundesanstalt, 3, 249-266.

Brigo L. and Omenetto P. (1979b) The Lead and Zinc ores of the Raibl (Cave del Predil-Northern Italy) zone:

https://doi.org/10.1180/mgm.2025.10124 Published online by Cambridge University Press

new metallogenic data. Verhandlungen der Geologischen Bundesanstalt, 3, 241-247.

Brusca C., Farabegoli E. and Viel G. (2010) Le mineralizzazioni Pb-Zn nel quadro paleogeografico del Trias delle Dolomiti Orientali. Ipotesi genetiche. Geo-Archeologia, 2010/1, 59-114.

Cadel G., Cosi M., Pennacchioni G. and Spalla M.I. (1996) A new map of the Permo-Carboniferous cover and Variscan metamorphic basement in the Central Orobic Alps, Southern Alps - Italy: structural and stratigraphical data. Memorie di Scienze Geologuche, 48, 1-53, https://hdl.handle.net/2434/221975.

Casati P. and Gnaccolini M. (1967) Geologia delle Alpi Orobie occidentali. Rivista Italiana di Paleontologia e Stratigrafia, 73, 25-162.

Cassinis G. (1968) Studio stratigrafico del 'Servino' di Passo Valdì (Trias inferiore dell'Alta Val Caffaro). Atti Istituto di Geologia dell'Università di Pavia, 19, 15-39.

Cassinis G., Cortesogno L., Gaggero L., Perotti C.R. and Buzzi L. (2008) Permian to Triassic geodynamic and magmatic evolution of the Brescian Prealps (eastern Lombardy, Italy). Bollettino della Società Geologica Italiana (Italian Journal fo Geosciences), 127(3), 501-518.

Cassinis G., Corbari D., Falletti P., Perotti C., Schirolli P., Calabrò R., Bini A., Rigamonti I., De Donatis S., Siletto G.B., Bersezio R., Jadoul F., Vercesi P., Cobianchi M., Mancin N., Ronchi P., Cortesogno L. and Castellarin A. (2011) Note illustrative della Carta Geologica d'Italia alla scala 1:50.000, F. 99 Iseo. 248 pp., Litografia Artistica Cartografica s.r.l., Verona.

Cathles L.M. and Smith A.T. (1983) Thermal constraints on the formation of Mississippi Valley-type lead-zinc deposits and their implications for episodic basin dewatering and deposit genesis: Economic Geology, 78, 983-1002, https://doi.org/10.2113/gsecongeo.78.5.983.

Cerny I. (1989) Die karbonatgebundenen Blei-ZinkLagerstätten des alpinen und ausser-alpinen Mesozoikums: Die Bedeutung ihrer Geologie, Stratigraphie und Faziesgebundenheit für Prospektion und Bewertung. Archiv für Lagerstättenforschung der Geologischen Bundesanstalt, 11, 5-125.

Choquette P.W. and James N.P. (1987) Diagenesis in Limestones - 3. The Deep Burial Environment. DIAGENESIS #12. Geoscience Canada, 14(1), 3-35, https://id.erudit.org/iderudit/geocan14_1art01.

Corbella M., Ayora C. and Cardellach E. (2004) Hydrothermal mixing, carbonate dissolution and sulfide precipitation in Mississippi Valley-type deposits. Mineralium Deposita, 39, 344-357, https://doi.org/10.1007/s00126-004-0412-5.

Craddock P.R., Bach W., Seewald J.S., Rouxel O.J., Reeves E. and Tivey M.K. (2010) Rare earth element

https://doi.org/10.1180/mgm.2025.10124 Published online by Cambridge University Press

abundances in hydrothermal fluids from the Manus Basin, Papua New Guinea: indicators of sub-seafloor hydrothermal processes in back-arc basins. Geochimica et Cosmochimica Acta, 74, 5494-5513, https://doi.org/10.1016/j.gca.2010.07.003.

Dal Corso J., Gianolla P., Newton R.J., Franceschi M., Roghi G., Caggiati M., Raucsik B., Budai T., Haas J. and Preto N. (2015) Carbon isotope records reveal synchronicity between carbon cycle perturbation and the "Carnian Pluvial Event" in the Tethys realm (Late Triassic). Global and Planetary Change, 127, 79-90, https://doi.org/10.1016/j.gloplacha.2015.01.013.

Dal Corso J., Gianolla P., Rigo M., Franceschi M., Roghi G., Mietto P., Manfrin S., Raucsik B., Budai T., Jenkyns H.C., Reymond C.E., Caggiati M., Gattolin G., Breda A., Merico A. and Preto N. (2018) Multiple negative carbon-isotope excursions during the Carnian Pluvial Episode (Late Triassic). Earth-Sciences Reviews, 185, 732-750, https://doi.org/10.1144/jgs2018-185.

Dal Piaz G.V., Massironi M. and Bistacchi A. (2003) Geological outline of the Alps. Episodes, 26(3), 175-180, https://doi.org/10.18814/epiiugs/2003/v26i3/004.

Danielson A., Moller P. and Dulski P. (1992) The europium anomalies in banded iron formations and the thermal history of the oceanic crust. Chemical Geology, 97, 89-100, https://doi.org/10.1016/0009-2541(92)90137-T.

Davies G.R. and Packard J.J. (2004) Hydrothermal (thermobaric) dolomitization: rock fabric and organic petrology support for emplacement under transient temperature, pressure and shear stress conditions. In: Dolomites - The spectrum: Mechanisms, models, reservoir development. Canadian Society of Petroleum Geologists (R. McAuley, editor), Seminar and Core Conference, Calgary, January 2004, 13-15.

Davies G.R. and Smith L.B. (2006) Structurally controlled hydrothermal dolomite reservoir facies: An overview. AAPG Bulletin, 90(11), 1641-1690, https://doi.org/10.1306/05220605164.

De Baar H.J.W., Bacon M.P., Brewer P.G. and K.W. Bruland (1985a) Rare earth elements in Pacific and Atlantic oceans. Geochimica et Cosmochimica Acta, 49, 1943-1959, https://doi.org/10.1016/0016-7037(85)90089-4.

Della Porta G., Webb G.E. and McDonald I. (2015) REE patterns of microbial carbonate and cements from Sinemurian (Lower Jurassic) siliceous sponge mounds (Djebel Bou Dahar, High Atlas, Morocco). Chemical Geology, 400, 65-86, https://doi.org/10.1016/j.chemgeo.2015.02.010.

Dickson J.A.D. (1966) Carbonate identification and genesis as revealed by staining. Journal of Sedimentary Research, 36(2), 491-505, https://doi.org/10.1306/74D714F6-2B21-11D7-8648000102C1865D.

https://doi.org/10.1180/mgm.2025.10124 Published online by Cambridge University Press

Douville E., Bienvenu P., Charlou J.L., Donval J.P., Fouquet Y., Appriou P. and Gamo T. (1999) Yttrium and rare earth elements in fluids from various deep-sea hydrothermal systems. Geochimica et Cosmochimica Acta, 63(5), 627-643, https://doi.org/10.1016/S0016-7037(99)00024-1.

Douville E., Charlou J.L., Oelkers E.H., Bienvenu P., Colon C.J., Donval J.P., Fouquet Y., Prieur D. and Appriou P. (2002) The rainbow vent fluids (36°14' N, MAR): the influence of ultramafic rocks and phase separation on trace metal content in MidAtlantic Ridge hydrothermal fluids. Chemical Geology, 184, 37-48, https://doi.org/10.1016/S0009-2541(01)00351-5.

Duan X.X., Zeng Q.D., Wang Y.B., Zhou L.L. and Chen B. (2017) - Genesis of the Pb-Zn deposits of the Qingchengzi ore field, eastern Liaoning, China: Constraints from carbonate LA− ICPMS trace element analysis and C-O-S-Pb isotopes. Ore Geology Reviews, 89, 752-771, https://doi.org/10.1016/j.oregeorev.2017.07.012.

Dunnington H.V. (1967) Aspects of diagenesis and shape in stylolitic limestone reservoirs. Geology and Geophysics, Proceedings of the 7th World Petroleum Congress, 2, 339-352.

Ebner M., Koehn D., Toussaint R., Renard F. and Schmittbuhl J. (2008) Stress sensitivity of stylolite morphology. Earth and Planetary Sciences Letters, 277, 394-398, https://doi.org/10.1016/j.epsl.2008.11.001.

Edmonds H.N. and German C.R. (2004) Particle geochemistry in the Rainbow hydrothermal plume, Mid-Atlantic Ridge. Geochimica et Cosmochimica Acta, 68(4), 759-772, https://doi.org/10.1016/S0016-7037(03)00498-8.

Forcella F., Bigoni C., Bini A., Ferliga C., Ronchi A. and Rossi S. (2012) - Note illustrative della Carta Geologica d'Italia alla scala 1:50.000, F. 78 Breno. 284 pp., LTS S.r.l., Treviso.

Frimmel H.E. (2009) Trace element distribution in Neoproterozoic carbonates as palaeoenvironmental indicator. Chemical Geology, 258, 338-353, https://doi.org/10.1016/j.chemgeo.2008.10.033.

Fruth I. and Maucher A. (1966) Spurenelemente und Schwefel-Isotope in Zinkblenden der Blei-Zink-Lagerstätte von Gorno. Mineralium Deposita, 1, 238-250, https://doi.org/10.1007/BF00204550.

Fusciardi L.P., Güven J.F. and Stewart D.R.A. (2003) The geology and genesis of the Lisheen Zn-Pb deposit, Co. Tipperary, Ireland. Pp. 455-481 in: *Europe's Major Base Metal Deposits* (J.G. Kelly, C.J. Andrew and J.H. Ashton, editors), Irish Association for Economic Geology, Dublin.

Gabitov R., Migdisov A., Nguyen A., Van Hartesveldt N., Perez-Huerta A., Sadekov A., Benedict Sauer K., Baker J., Paul V., Caporuscio F., Xu H. and Roback R. (2021) Uptake of uranium by carbonate crystallization from reduced and oxidized hydrothermal fluids. Chemical Geology, 564, 120054,

https://doi.org/10.1180/mgm.2025.10124 Published online by Cambridge University Press

https://doi.org/10.1016/j.chemgeo.2020.120054.

Garven G. (1985) The role of regional fluid flow in the genesis of the Pine Point deposit, Western Canada Sedimentary Basin. Economic Geology, 80, 307-324, https://doi.org/10.2113/gsecongeo.80.2.307.

Garven G. and Freeze R.A. (1984) Theoretical analysis of the role of groundwater flow in the genesis of stratabound ore deposits. 2. Quantitative results. American Journal of Sciences, 284, 1125-1174, https://doi.org/10.2475/ajs.284.10.1125.

Garven G. and Raffensperger J.P. (1997) Hydrogeology and geochemistry of ore genesis in sedimentary basins. Pp. 125-189 in: *Geochemistry of hydrothermal ore deposits* (H.L. Barnes, editor), Wiley, New York.

Garven G. and Wallace M.M. (2009) The geohydrology of MVT-ore genesis in the Canning Basin, Western Australia. Eos, Transactions American Geophysical Union 90(22), Joint Assembly Supplement, Abstract #M#A73C-01.

Garzanti E. (1985) The sandstone memory of the evolution of a Triassic volcanic arc in the Southern Alps, Italy. Sedimentology, 32, 423-433, https://doi.org/10.1111/j.1365-3091.1985.tb00521.x.

Garzanti E. and Jadoul F. (1985) Stratigrafia e paleogeografia del Carnico lombardo (Sondaggio S. Gallo, Val Brembana). Rivista Italiana di Paleontologia e Stratigrafia, 91(3), 295-320.

Garzanti E., Gnaccolini M. and Jadoul F. (1995) Anatomy of a semiarid coastal system: the Upper Carnian of Lombardy (Italy). Rivista Italiana di Paleontologia e Stratigrafia, 101, 17-36.

German C.R., Klinkhammer G.P., Edmond J.M., Mitra A. and Elderfield H. (1990) Hydrothermal scavenging of rare-earth elements in the ocean. Nature, 345, 516-518, https://doi.org/10.1038/345516a0.

Giorno M., Barale L., Bertok C., Frenzel M., Looser N., Guillong M., Bernasconi S.M. and Martire L. (2022) Sulfide-associated hydrothermal dolomite and calcite reveal a shallow burial depth for Alpine-type Zn-(Pb) deposits. Geology, 50, 853-858, https://doi.org/10.1130/G49812.1.

Gnaccolini M. (1983) Un apparato deltizio triassico nelle Prealpi Bergamasche. Rivista Italiana di Paleontologia e Stratigrafia, 88, 599-612.

Gnaccolini M. (1986) La Formazione di Gorno nei dintorni di Dossena e di Gorno (Prealpi Bergamasche): analisi di una laguna triassica. Rivista Italiana di Paleontologia e Stratigrafia, 92, 3-32.

Gnaccolini M. (1988) Arenaria di Val Sabbia e Formazione di Gorno: un sistema deposizionale delta-laguna nel Trias superiore delle Prealpi Bergamasche. Rivista Italiana di Paleontologia e Stratigrafia, 93, 329-336.

Gnaccolini M. and Jadoul F. (1988) Il sistema deposizionale delta-laguna-piattaforma carbonatica: un esempio

https://doi.org/10.1180/mgm.2025.10124 Published online by Cambridge University Press

del Trias superiore lombardo (Alpi Meridionali). Rivista Italiana di Paleontologia e Stratigrafia, 93, 10-32.

Goldberg E.D., Koide M., Schmitt R.A. and Smith R.H. (1963) Rare-earth distributions in the marine environment. Journal of Geophysical Research, 68, 4209-4217, https://doi.org/10.1029/JZ068i014p04209.

Gong Q., Li F., Lu C., Wang H. and Tang H. (2021) Tracing seawater and terrestrial-sourced REE signatures in detritally contaminated, diagenetically altered carbonate rocks. Chemical Geology, 570, 120169, https://doi.org/10.1016/j.chemgeo.2021.120169.

Goodfellow W.D., Lydon S.W. and Turner R.J.W. (1993) Geology and genesis of stratiform sediment-hosted (SEDEX) zinc-lead-silver sulphide deposits. Pp. 201-251 in: *Mineral Deposit Modeling* (R.V. Kirkham, W.D. Sinclair, R.I. Thorpe and J.M. Duke, editors), Geological Association of Canada Special Paper, 40.

Goodfellow W.D. and Lydon J.W. (2007) Sedimentary-exhalative (SEDEX) deposits. Geological Association of Canada, Mineral Deposits Division, Special Publication, 5, 163-183.

Gramaccioli C.M., Diella V. and Demartin F. (2000) The formation of scandium minerals as an example of the role of complexes in the geochemistry of rare earths and HFS elements. European Journal of Mineralogy, 12, 795-808, https://doi.org/10.1127/0935-1221/2000/0012-0795.

Griffin W.L., Powell W., Pearson N.J. and O'Reilly S.Y. (2008) GLITTER: Data reduction software for laser ablation ICP-MS. Laser Ablation-ICP-MS in the Earth Sciences: Current practices and outstanding issues. Mineralogical Association of Canada, 308-311.

Hein U.F., Lüders V. and Dulsky P. (1990) The fluorite vein mineralization of the Southern Alps: combined application of fluid inclusions and rare earth element (REE) distribution. Mineralogical Magazine, 54, 325-333, https://doi.org/10.1180/minmag.1990.054.375.18.

Henjes-Kunst E., Raith J.G. and Boyce A.J. (2017) Micro-scale sulfur isotope and chemical variations in sphalerite from the Bleiberg Pb-Zn deposit, Eastern Alps, Austria. Ore Geology Reviews, 90, 52-62, https://doi.org/10.1016/j.oregeorev.2017.10.020.

Heydari E. and Moore C.H. (1989) Burial diagenesis and thermochemical sulfate reduction, Smackover Formation, southeastern Mississippi Salt Basin. Geology, 12, 1080-1084, https://doi.org/10.1130/0091-7613(1989)017<1080:BDATSR>2.3.CO;2.

Hiatt E.E. and Pufahl P.K. (2014) Cathodoluminescence petrography of carbonate rocks: application to understanding diagenesis, reservoir quality, and pore system evolution. Pp. 75-96 in: *Cathodoluminescence and its application to geoscience* (I. Coulson, editor), Mineralogical Association of Canada, Short Course Series

https://doi.org/10.1180/mgm.2025.10124 Published online by Cambridge University Press

45.

Hitzman M.W. and Beaty D.W. (1996) The Irish Zn-Pb-(Ba) orefield. Pp. 112-143 in: *Carbonate-Hosted Lead-Zinc Deposits* (D.F. Sangster, editor), Society of Economic Geologists Special Publication, 4. Littleton, CO: Society of Economic Geologists, Inc, https://doi.org/10.5382/SP.04.08.

Hitzman M.W., Redmond P.B. and Beaty D.W. (2002) - The carbonate-hosted Lisheen Zn-Pb-Ag deposit, County Tipperary, Ireland. Econ. Geol., 97, 1627-1655, https://doi.org/10.2113/gsecongeo.97.8.1627.

Høgdahl O.T. (1967) Distribution of the rare earth elements in seawater. NATO Research Grant No. 203. Central Inst. Ind. Res., Blindern, Semi-Annu. Progr. Rep., 4 (unpublished).

Høgdahl O.T., Melson S. and Bowen V.T. (1968) Neutron activation analysis of lanthanide elements in seawater. Pp. 308-325 in: *Trace Inorganics in Water* (R.A. Baker editor), Advances in Chemistry Series, 73, 10.1021/ba-1968-0073.ch019.

Hou Y., Azmy K., Berra F., Jadoul F., Blamey N.J.F., Gleeson S.A. and Brand U. (2016) Origin of the Breno and Esino dolomites in the western Southern Alps (Italy): Implications for a volcanic influence. Marine and Petroleum Geology, 69, 38-52, https://doi.org/10.1016/j.marpetgeo.2015.10.010.

Hreus S., Výravský J., Cempýrek J., Breiter K., Galiova M.V., Kratký O., Sesulka V. and Skoda R. (2021) Scandium distribution in the world-class Li-Sn-W Cínovec greisen-type deposit: Result of a complex magmatic to hydrothermal evolution, implications for scandium valorization. Ore Geology Reviews, 139, 104433, https://doi.org/10.1016/j.oregeorev.2021.104433.

Jackson S.A. and Beales F.W. (1967) An aspect of sedimentary basin evolution: The concentration of Mississippi Valley-type ores during the late stages of diagenesis. Bulletin of Canadian Petroleum Geology, 15, 393-433, https://doi.org/10.35767/gscpgbull.15.4.383.

Jadoul F. and Rossi P.M. (1982) Evoluzione paleogeografico-strutturale e vulcanismo triassico nella Lombardia centro-occidentale. Pp. 143-155 in: *Guida alla geologia del Sudalpino centro-occidentale*. Guide Geologiche Regionali della Società Geologica Italiana.

Jadoul F. (1986) Stratigrafia e paleogeografia del Norico nelle Prealpi Bergamasche occidentali. Rivista Italiana di Paleontologia e Stratigrafia, 91 (4), 479-512.

Jadoul F., Berra F., Frisia S., Ricchiuto T. and Ronchi P. (1992a) Stratigraphy, paleogeography and genetic model of Late Carnian carbonate breccias (Castro Formation, Southern Alps of Lombardy, Italy). Rivista Italiana di Paleontologia e Stratigrafia, 97, 355-392, https://hdl.handle.net/2434/430150.

https://doi.org/10.1180/mgm.2025.10124 Published online by Cambridge University Press

Jadoul F., Berra F. and Frisia S. (1992b) Stratigraphic and paleogeographic evolution of a carbonate platform in an extensional tectonic regime: the example of the Dolomia Principale in Lombardy (Italy). Rivista Italiana di Paleontologia e Stratigrafia, 98, 29-44.

Jadoul F., Gervasutti M. and Fantini Sestini N. (1992c) The Middle Triassic of the Brembana Valley: preliminary study of the Esino Platform evolution (Bergamasc Alps). Rivista Italiana di Paleontologia e Stratigrafia, 98, 299-324.

Jadoul F., Berra F., Bini A., Ferliga C., Mazzoccola D., Papani L., Piccin A., Rossi R., Rossi S. and Trombetta G.L. (2012) - Note illustrative della Carta Geologica d'Italia alla scala 1:50.000, F. 77 Clusone. 120 pp, LTS S.r.l., Treviso.

James R.H., Elderfield H. and Palmer M.R. (1995) The chemistry of hydrothermal fluids from the Broken Spur site, 29 °N Mid-Atlantic ridge. Geochimica et Cosmochimica Acta, 59, 651-659, https://doi.org/10.1016/0016-7037(95)00003-I.

Jarvis K.E., Gray A.L. and McCurdy E. (1989) Avoidance of spectral interference on europium in inductively coupled plasma mass spectrometry by sensitive measurement of the doubly charged ion. Journal of Analytical Atomic Spectrometry, 4, 743-747, https://doi.org/10.1039/JA9890400743.

Jicha H.L. (1951) Alpine lead-zinc ores of Europe. Economic Geology, 46, 707-730, https://doi.org/10.2113/gsecongeo.46.7.707.

Johannessen K.C., Vander Roost J., Dahle H., Dundas S.H., Pedersen R.B. and Thorseth I. H. (2017) Environmental controls on biomineralization and Fe-mound formation in a low-temperature hydrothermal system at the Jan Mayen Vent Fields. Geochimica et Cosmochimica Acta, 202, 101-123, https://doi.org/10.1016/j.gca.2016.12.016.

Kamber B.S., Greig A. and Collerson K.D. (2005) A new estimate for the composition of weathered young upper continental crust from alluvial sediments, Queensland, Australia. Geochimica et Cosmochimica Acta, 69, 1041-1058, https://doi.org/10.1016/j.gca.2004.08.020.

Kareem K.H., Al-Aasm I.S. and Mansurbeg H. (2021) Geochemical constraints of hydrothermal alteration of dolostones: An example of Lower Cretaceous Qamchuqa Formation, Kurdistan Region, northern Iraq. Marine and Petroleum Geology, 134, 105337, https://doi.org/10.1016/j.marpetgeo.2021.105337.

Köppel V. and Schroll E. (1988) Pb-isotope evidence for the origin of lead in strata-bound Pb-Zn deposits in triassic carbonates of the Eastern and Southern Alps. Mineralium Deposita, 23, 96-103,

https://doi.org/10.1180/mgm.2025.10124 Published online by Cambridge University Press

https://doi.org/10.1007/BF00206657.

Krouse H.R., Viau C.A., Eliuk L.S., Ueda A. and Halas S. (1988) Chemical and isotopic evidence of thermochemical sulfate reduction by light hydrocarbon gases in deep carbonate reservoirs. Nature, 333, 415-419, https://doi.org/10.1038/333415a0.

Kučera J., Cempírek J., Dolníček Z., Muchez P. and Prochaska W. (2009) Rare earth elements and yttrium geochemistry of dolomite from post-Variscan vein-type mineralization of the Nízký Jeseník and Upper Silesian Basins, Czech Republic. Journal of Geochemical Exploration, 103, 69-79, https://doi.org/10.1016/j.gexplo.2009.08.001.

Kucha H., Schroll E., Raith J.G. and Halas S. (2010) Microbial sphalerite formation in carbonate-hosted Zn-Pb ores, Bleiberg, Austria: Micro to nanotextural and sulfur isotope evidence. Economic Geology, 105, 1005-1023, https://doi.org/10.2113/econgeo.105.5.1005.

Kuhlemann J., Vennemann T., Herlec U., Zeeh S. and Bechstädt T. (2001) Variation of sulfur isotopes, trace element compositions and cathodoluminescence of Mississippi Valley-Type Pb-Zn ores from the Drau range, Eastern Alps (Slovenia-Austria): implications for ore deposition on a regional versus microscale. Economic Geology, 96, 1931-1941, https://doi.org/10.2113/gsecongeo.96.8.1931.

Large D.E. (1983) Sediment-hosted massive sulphide lead-zinc deposits: An empirical model. Pp. 1-29 in: *Sediment-Hosted Stratiform Lead-Zinc Deposits* (D.F. Sangster, editor), Mineralogical Association of Canada Short Course Series, 9, https://doi.org/10.1007/978-94-009-3169-5_1.

Large R.R., Bull S.W., McGoldrick P.J., Walters S., Derrick G.M. and Carr G.R. (2005) Stratiform and stratabound Zn-Pb-Ag deposits in Proterozoic sedimentary basins, northern Australia. Pp. 931-963 in: *Economic Geology 100th Anniversary Volume* (J.W. Hedenquist, J.F.H. Thompson, R.J. Goldfarb and J.P. Richards, editors), Society of Economic Geologists, Littleton CO, United States, https://doi.org/10.5382/AV100.28.

Laubscher H.P. (1985) Large scale, thin-skinned thrusting in the southern Alps: kinematic models. Geological Society of America Bulletin, 96, 710-718, https://doi.org/10.1130/0016-7606(1985)96<710:LTTITS>2.0.CO;2.

Lavoie D. and Chi G. (2001) The Lower Silurian Sayabec Formation in northern Gaspé: carbonate diagenesis and reservoir potential. Bulletin of Canadian Petroleum Geology, 49(2), 282-298, https://doi.org/10.2113/49.2.282.

Lawrence M.G., Greig A., Collerson K.D. and Kamber B.S. (2006) Rare earth element and yttrium variability in southeast Queensland waterways. Aquatic Geochemistry, 12, 39-72, https://doi.org/10.1007/s10498-005-4471-8.

https://doi.org/10.1180/mgm.2025.10124 Published online by Cambridge University Press

Leach D.L. and Sangster D.F. (1993) Mississippi Valley-type lead-zinc deposits. Pp. 289-314 in: *Mineral Deposit Modeling* (R.V. Kirkham, W.D. Sinclair, R.I. Thorpe, J.M. Duke editors), Geological Association of Canada Special Paper, 40, St. John's, NL, Canada.

Leach D.L., Bradley D., Lewchuk M.T., Symons D.T.A., de Marsily G. and Brannon J. (2001) Mississippi Valley–type lead-zinc deposits through geological time: Implications from recent age-dating research. Mineralium Deposita, 36, 711-740, https://doi.org/10.1007/s001260100208.

Leach D.L., Bechstädt T., Boni M. and Zeeh S. (2003) Triassic-hosted Mississippi Valley-type zinc-lead ores of Poland, Austria, Slovenia, and Italy. Pp. 169-213 in: *Europe's Major Base Metal Deposits* (J. Ashton, M. Boland, M. Cruise, G. Earls, L. Fusciardi, J. Kelly, G. Stanley and C. Andrew, editors), Irish Association of Economic Geologists (IAEG).

Leach D.L., Marsh E., Emsbo P., Rombach C.S., Kelley K.D. and Anthony M. (2004) Nature of hydrothermal fluids at the shale-hosted Red Dog Zn-Pb-Ag deposits, Brooks Range, Alaska. Economic Geology, 99(7), 1449-1480, https://doi.org/10.2113/gsecongeo.99.7.1449.

Leach D.L., Sangster D.F., Kelley K.D., Large R.R., Garven G., Allen C.R., Gutzmer J. and Walters S. (2005) Sediment-hosted lead-zinc deposits: A global perspective. Economic Geology 100th Anniversary Volume, 561-607,
https://doi.org/10.5382/AV100.18.

Leach D.L., Bradley D.C., Huston D., Pisarevsky S.A., Taylor R.D. and Gardoll S.J. (2010) Sediment-hosted lead-zinc deposits in Earth history. Economic Geology, 105, 593-625, https://doi.org/10.2113/gsecongeo.105.3.593.

Leach D.L., Taylor R.D., Fey D.L., Diehl S.F. and Saltus R.W. (2010) A deposit model for Mississippi Valley-Type lead-zinc ores. Pp. 52 in: *Mineral deposit models for resource assessment* (U.S. Geological Survey, editor), U.S. Geological Survey Scientific Investigations Report 2010–5070–A, 52 pp.

Li T., Zhu D., Yang M., Zhang X., Li P., Lu C. and Zou H. (2021) Early-stage marine dolomite altered by hydrothermal fluids in the Middle Permian Maokou Formation in the eastern Sichuan Basin, Southern China. Marine and Petroleum Geology, 134, 105367, https://doi.org/10.1016/j.marpetgeo.2021.105367.

Liang T. and Jones B. (2021) Characteristics of primary rare earth elements and yttrium in carbonate rocks from the Mesoproterozoic Gaoyuzhuang Formation, North China: Implications for the depositional system. Sedimentary Geology, 415, 105864, https://doi.org/10.1016/j.sedgeo.2021.105864.

Liu J., Li Z., Wang X., Jiang L., Feng Y. and Wallace M.W. (2022) Tectonic-fluid evolution of an ultra-deep

https://doi.org/10.1180/mgm.2025.10124 Published online by Cambridge University Press

carbonate reservoir in the southern Halahatang Oilfield area, Tarim Basin, NW China. Marine and Petroleum Geology, 145, 105870, https://doi.org/10.1016/j.marpetgeo.2022.105870.

Lowther J.M., Balding A.B., McEvoy F.M. and Dunphy S. (2003) The Galmoy Zn-Pb orebodies: Structure and metal distribution-clues to the genesis of the deposits. Pp. 437-452 in: *Europe's major base metal deposits* (L. Fusciardi, G. Earls, G. Stanley, J. Kelly, J. Ashton, M. Boland and C.J. Andrew, editors), Special Publication of the Irish Association for Economic Geology.

Luong L.D., Shinjo R., Hoang N., Shakirov R.B. and Syrbu N. (2018) Spatial variations in dissolved rare earth element concentrations in the East China Sea water column. Marine Chemistry, 205, 1-15, https://doi.org/10.1016/j.marchem.2018.07.004.

Lydon J.W. (1983) Chemical parameters controlling the origin and deposition of sediment-hosted stratiform lead-zinc deposits. Pp. 175-250 in: *Sediment-Hosted Stratiform Lead-Zinc Deposits* (D.F. Sangster, editor), Mineralogical Association of Canada Short Course Series, 9.

Lydon J. (1996) Sedimentary exhalative sulphides (SEDEX). Pp. 130-152 in: *Geology of Canadian Mineral Deposit Types* (O. Eckstrand, W. Sinclair and R. Thorpe, editors), Geological Survey of Canada, Geology of Canada Series, 8.

Machel H.G. (1987) Saddle dolomite as a by-product of chemical compaction and thermochemical sulfate reduction. Geology, 15, 936-940, https://doi.org/10.1130/0091-7613(1987)15<936:SDAABO>2.0.CO;2.

Machel H.G., Mason R.A., Mariano A.N. and Mucci A. (1991) Causes and emission of luminescence in calcite and dolomite. Luminescence Microscopy. Quantitative and Qualitative Aspects (SC25), 9-26, https://doi.org/10.2110/scn.91.25.0009.

Machel H.G. (2001) Bacterial and thermochemical sulfate reduction in diagenetic settings - old and new insights. Sedimentary Geology, 140(1-2), 143-175, https://doi.org/10.1016/S0037-0738(00)00176-7.

Machel H.G. and Lonnee J. (2002) Hydrothermal dolomite - A product of poor definition and imagination. Sedimentary Geology, 152, 163-171, 10.1016/S0037-0738(02)00259-2.

Machel H.G. (2004) Concepts and models of dolomitization: a critical reappraisal. Pp. 7-63 in: *The Geometry and Petrogenesis of Dolomite Hydrocarbon Reservoirs* (C.J.R. Braithwaite, G. Rizzi and G. Darke, editors), The Geological Society of London, 235. Special Publication, https://doi.org/10.1144/GSL.SP.2004.235.01.02.

Manatschal G. and Bernoulli D. (1998) Rifting and early evolution of ancient ocean basins: the record of the Mesozoic Tethys and of the Galicia-Newfoundland margins. Marine Geophysical Research, 20, 371-381,

https://doi.org/10.1180/mgm.2025.10124 Published online by Cambridge University Press

https://doi.org/10.1023/A:1004459106686.

Marinelli M., Viel G and Farabegoli E. (1980) Il Permo-Trias delle Alpi Meridioali: evoluzione tardo-ercinica di un bacino marginale di retroarco ensialico. Industria Mineraria, 31, 1-14.

Maucher A. and Schneider H.J. (1967) The Alpine lead-zinc ores. Pp. 71-89 in: *Genesis of stratiform lead-zinc-barite-fluorite deposits* (J.S. Brown, editor), Economic Geology Monograph, 3, https://doi.org/10.5382/Mono.03.

McLennan S.M. (1989) Rare earth elements in sedimentary rocks: influence of provenance and sedimentary processes. Reviews in Mineralogy and Geochemistry, 21, 169-200.

Melcher F., Henjes-Kunst F., Henjes-Kunst E., Schneider J. and Thöni M. (2010) Erste Rb-Sr Isotopendatierung an Sphalerit der Zn-Pb Lagerstätte Bleiberg (Kärnten), sowie Sr- und Sm-Nd-Isotopendaten von kogenetischem Karbonat und Fluorit. Journal of Alpine Geology, 52, 178-18.

Melcher F., Bertrandsson Erlandsson V., Gartner V., Henjes-Kunst E., Raith J., Rantitsch G., Onuk P., Henjes-Kunst F., Potočnik Krajnc B. and Šoster A. (2023) Carbonate-hosted "Alpine-type" Zn-Pb deposits in the Eastern and Southern Alps - trace element geochemistry and isotopic data of sulphides. Pp. 443-478 in: *Irish-type Deposits around the world* (C.J. Andrew, M.W. Hitzman and G. Stanley, editors), Irish Association for Economic Geology, https://doi.org/10.61153/NIWU8065.

Melim L.A., Swart P.K. and Maliva R.G. (1995) Meteoric-like fabrics forming in marine waters: Implications for the use of petrography to identify diagenetic environments. Geology, 23, 755-758, https://doi.org/10.1130/0091-7613(1995)023<0755:MLFFIM>2.3.CO;2.

Meyers W.J. (1989) Trace element and isotope geochemistry of zoned calcite cements, Lake Valley Formation (Mississippian, New Mexico): insights from water-rock interaction modelling. Sedimentary Geology, 65, 355-370, https://doi.org/10.1016/0037-0738(89)90034-1.

Michard A., Albarède F., Michard G., Minster J.F. and Charlou J.L. (1983) Rare-earth elements and uranium in high-temperature solutions from East Pacific rise hydrothermal vent field (13 °N). Nature, 303, 795-797, https://doi.org/10.1038/303795a0.

Migdisov A.A., Williams-Jones A. and Wagner T. (2009) An experimental study of the solubility and speciation of the rare earth elements (III) in fluoride- and chloride- bearing aqueous solutions at temperatures up to 300°C. Geochimica et Cosmochimica Acta, 73(23), 7087-7109, https://doi.org/10.1016/j.gca.2009.08.023.

Migdisov A.A., Boukhalfa H., Timofeev A., Runde W., Roback R. and Williams-Jones A.E. (2018) A spectroscopic

https://doi.org/10.1180/mgm.2025.10124 Published online by Cambridge University Press

study of uranyl speciation in chloride-bearing solutions at temperatures up to 250 °C. Geochimica et Cosmochimica Acta, 222, 130-145, https://doi.org/10.1016/j.gca.2017.10.016.

Mitra A., Elderfield H. and Greaves M.J. (1994) Rare earth elements in submarine hydrothermal fluids and plumes from the Mid-Atlantic Ridge. Marine Chemistry, 46, 217-235, https://doi.org/10.1016/0304-4203(94)90079-5.

Möller P., Bau M., Dulski P. and Lüders V. (1998) REE and yttrium fractionation in fluorite and their bearing on fluorite formation. In: Proc 9th Quadr IAGOD Symp, 1998, 575-592.

Mondillo N., Boni M., Balassone G., Spoleto S., Stellato F., Marino A., Santoro L. and Spratt J. (2016) Rare earth elements (REE). Minerals in the Silius fluorite vein system (Sardinia, Italy). Ore Geology Reviews, 74, 211-224, https://doi.org/10.1016/j.oregeorev.2015.11.016.

Mondillo N., Lupone F., Boni M., Joachimski M., Balassone G., De Angelis M., Zanin S. and Granitzio F. (2020) From Alpine-type sulfides to nonsulfides in the Gorno Zn project (Bergamo, Italy). Mineralium Deposita, 55, 953-970, https://doi.org/10.1007/s00126-019-00912-5.

Moore S.L. (1994) *The origin of dolomite of the Middle Cambrian Eldon and Pika Formations in the Yoho Glacier area, Yoho National Park, British Columbia*. Master's thesis, University of Calgary, Canada), https://prism.ucalgary.ca. doi:10.11575/PRISM/24463.

Morad S., Ketzer M. and De Ros L.F. (2000) Spatial and temporal distributions of diagenetic alterations in siliciclastic rocks. Sedimentology, 47, 95-120, https://doi.org/10.1046/j.1365-3091.2000.00007.x.

Morad S., Al-Aasm I.S., Sirat M. and Sattar M.M. (2010) Vein calcite in cretaceous carbonate reservoirs of Abu Dhabi: Record of origin of fluids and diagenetic conditions. Journal of Geochemical Exploration, 106, 156-170, https://doi.org/10.1016/j.gexplo.2010.03.002.

Morrow D. (1998) Regional subsurface dolomitization: Models and constraints. Geoscience Canada, 25(2), 57-70.

Mudd G.M., Jowitt S.M. and Werner T.T. (2017) The world's lead-zinc mineral resources: Scarcity, data, issues and opportunities. Ore Geology Reviews, 80, 1160-1190, https://doi.org/10.1016/j.oregeorev.2016.08.010.

Navarro-Ciurana D., Corral I. and Corbella M. (2023) A tool for Zn-Pb MVT exploration by combining C and O isotopes and REE geochemistry of dolomite. Ore Geology Reviews, 156, 105405, https://doi.org/10.1016/j.oregeorev.2023.105405.

Nelson J., Paradis S., Christensen J. and Gabites J. (2002) Canadian Cordilleran Mississippi Valley-type deposits:

https://doi.org/10.1180/mgm.2025.10124 Published online by Cambridge University Press

A case for Devonian-Mississippian back-arc hydrothermal origin. Economic Geology, 97, 1013-1036, https://doi.org/10.2113/gsecongeo.97.5.1013.

Nicolaides S. and Wallace M.W. (1997) Pressure-dissolution and cementation in an Oligo-tropical limestone (Clifton Formation), Otway Basin, Australia. Pp. 249-261 in: *Cool Water Carbonates* (N.P. James and J.A.D. Clarke, editors), Society for Sedimentary Geology Special Publication, 56, 249-261.

Nothdurft L.D., Webb G.E. and Kamber B.S. (2004) Rare earth element geochemistry of late Devonian reefal carbonates, Canning Basin, Western Australia: confirmation of a seawater REE proxy in ancient limestones. Geochimica et Cosmochimica Acta, 68, 263-283, https://doi.org/10.1016/S0016-7037(03)00422-8.

Nozaki Y., Zhang J. and Amakawa H. (1997) The fractionation between Y and Ho in the marine environment. Earth and Planetary Science Letters, 148, 329-340, https://doi.org/10.1016/S0012-821X(97)00034-4.

Oliver J. (1986) Fluids expelled tectonically from orogenic belts, their role in hydrocarbon migration and other geological phenomena. Geology, 14, 99-102, https://doi.org/10.1130/0091-7613(1986)14<99:FETFOB>2.0.CO;2.

Omenetto P. (1966) Il giacimento Piombo-Zincifero di Oltre il Colle (Alpi Bergamasche). Memorie degli Istituti di Geologia e Mineralogia dell'Università di Padova, XXV, 49 pp.

Omenetto P. and Vailati G. (1977) Ricerche geominerarie nel settore centrale del distretto a Pb, Zn, fluorite e barite di Gorno (Lombardia). L'Industria Mineraria, Gennaio-Febbraio 1977, 25-44.

Packard J., Al-Aasm I.S., Samson I. and Berger Z. (2001) A Devonian "hydrothermal" chert reservoir: the 225 Bcf Parkland Field, British Columbia, Canada. AAPG Bulletin 85, 51–84, https://doi.org/10.1306/8626C75D-173B-11D7-8645000102C1865D.

Palinkaš L.A., Šoštarić S.B. and Palinkaš S.S. (2008) Metallogeny of the Northwestern and Central Dinarides and Southern Tisia. Ore Geology Reviews, 34, 501-520, https://doi.org/10.1016/j.oregeorev.2008.05.006.

Paradis S., Hannigan P. and Dewing K. (2007) Mississippi Valley-type lead-zinc deposits. Pp. 185-203 in: *Mineral Deposits of Canada: A Synthesis of Major Deposit-Types, District Metallogeny, the Evolution of Geological Provinces, and Exploration Methods* (W.D. Goodfellow, editor), Geological Association of Canada, Mineral Deposits Division, Special Publication 5, 185-203.Preto N., Kustatscher E. and Wignall P.B. (2010) Triassic climates - State of the art and perspectives. Palaeogeography, Palaeoclimatology, Paleoecology, 290, 1-10, https://doi.org/10.1016/j.palaeo.2010.03.015.

Preto N., Willems H., Guaiumi C. and Westphal H. (2013) Onset of significant pelagic carbonate accumulation

https://doi.org/10.1180/mgm.2025.10124 Published online by Cambridge University Press

after the Carnian Pluvial Event (CPE) in the western Tethys. Facies, 59, 891-914, https://doi.org/10.1007/s10347-012-0338-9.

Qing H. and Mountjoy E.W. (1992) Formation of Coarsely Crystalline, Hydrothermal Dolomite Reservoirs in the Presqu'ile Barrier, Western Canada Sedimentary Basin. AAPG Bulletin, 78(1), 55-77, https://doi.org/10.1306/BDFF9014-1718-11D7-8645000102C1865D.

Qing H. and Mountjoy E.W. (1994) Rare earth element geochemistry of dolomites in the Middle Devonian Presqùile barrier, Western Canada Sedimentary Basin: implications for fluid-rock ratios during dolomitization. Sedimentology, 41, 787-804, https://doi.org/10.1111/j.1365-3091.1994.tb01424.x.

Rachidi M., Neuweiler F. and Kirkwood D. (2009) Diagenetic-geochemical patterns and fluid evolution history of a Lower Jurassic petroleum source rock, Middle Atlas, Morocco. Journal of Petroleum Geology, 32, 111-128, https://doi.org/10.1111/j.1747-5457.2009.00439.x.

Radke B.M. and Mathis R.L. (1980) On the formation and occurrence of saddle dolomite. Journal of Sedimentary Petrology, 50(4) , 1149-1168, https://doi.org/10.1306/212F7B9E-2B24-11D7-8648000102C1865D.

Rameil S. (2008) Early diagenetic dolomitization and dedolomitization of Late Jurassic and earliest Cretaceous platform carbonates: A case study from the Jura Mountains (NW Switzerland, E France). Sedimentary Geology, 212(1-4), 70-85, https://doi.org/10.1016/j.sedgeo.2008.10.004.

Rasmussen B. and Krapez B. (2000) Evidence of hydrocarbon and metalliferous fluid migration in the Palaeoproterozoic Earaheedy Basin of Western Australia. Journal of the Geological Society of London, 157, 355-366, https://doi.org/10.1144/jgs.157.2.355.

Richardson C.K. and Holland H.D. (1979) Fluorite deposition in hydrothermal systems. Geochimica et Cosmochimica Acta, 43., 1327-1335, https://doi.org/10.1016/0016-7037(79)90122-4.

Rigo M., Preto N., Roghi G., Tateo F. and Mietto P. (2007) A rise in the Carbonate Compensation Depth of western Tethys in the Carnian (Late Triassic): Deep-water evidence for the Carnian Pluvial Event. Palaeogeography, Palaeoclimatology, Paleoecology, 246, 188-205, https://doi.org/10.1016/j.palaeo.2006.09.013.

Rimstid J.D., Balog A. and Webb J. (1998) Distribution of trace elements between carbonate minerals and aqueous solutions. Geochimica et Cosmochimica Acta, 62, 1851-1863, https://doi.org/10.1016/S0016-7037(98)00125-2.

https://doi.org/10.1180/mgm.2025.10124 Published online by Cambridge University Press

Rodeghiero F., Jadoul F., Vailati G. and Venerandi I. (1986) Dati preliminari sulle mineralizzazioni a Pb-Zn dell'area tra Mandello e Ballabio (Lombardia Centrale). Memorie della Società Geologica Italiana, 32, 133-150.

Ronchi P., Masetti D., Tassan S. and Camocino D. (2012) Hydrothermal dolomitization in platform and basin carbonate successions during thrusting: A hydrocarbon reservoir analogue (Mesozoic of Venetian Southern Alps, Italy). Marine and Petroleum Geology, 29(1), 68-89, https://doi.org/10.1016/j.marpetgeo.2011.09.004.

Rossetti R. (1967) Considerazioni sui rapporti tra le diverse facies ladiniche nella zona del Pizzo Camino e della Concarena (Bresciano nord-occidentale). Atti dell'Istituto di Geologia dell'Università di Pavia, 17, 124-142.

Russel M.J. (1978) Downward-excavating hydrothermal cells and Irish type ore deposits: Importance of an underlying thick Caledonian prism. Journal of Mining and Metallurgy, section B, 87, B168-B171.

Russel M.J. (1986) Extension and convection: A genetic model for the Irish Carboniferous base metal and barite deposits. Pp. 545-554 in: *Geology and Genesis of Mineral Deposits in Ireland* (C.J. Andrew, R.W.A. Crowe, S. Finlay, W.M. Pennell and J. Pyne, editors), Dublin Irish Association for Economic Geology.

Saito M.A., Sigman D.M. and Morel F.M. (2003) The bioinorganic chemistry of the ancient ocean: the co-evolution of cyanobacterial metal requirements and biogeochemical cycles at the Archean–Proterozoic boundary? Inorganica Chimica Acta, 356, 308–318, https://doi.org/10.1016/S0020-1693(03)00442-0.

Sangster D.F. (1976) Carbonate-hosted lead-zinc deposits. Pp. 447-456 in: *Handbook of stratabound and stratiform ore deposits* (Wolf K.H., editor), 6, https://doi.org/10.5382/SP.04.

Sangster D.F. (1990) Mississippi Valley-type and sedex lead-zinc deposits: a comparative examination. Journal of Mining and Metallurgy, section B., 99, B21-B42.

Sciunnach D., Garzanti E. and Confalonieri M. (1996) Stratigraphy and petrography of Upper Permian to Anisian terrigenous wedges (Verrucano Lombardo, Servino and Bellano Formations; western Southern Alps). Rivista Italiana di Paleontologia e Stratigrafia, 102(1), 27-48.

Schmid S.M., Aebli H.R., Heller F. and Zingg A. (1989) The role of the periadriatic line in the tectonic evolution of the Alps. Pp. 153-171 in: Alpine tectonics, 45, (M.P. Coward, D. Dietrich and R.G. Park, editors), Geological Society of London, Special Publications, London, https://doi.org/10.1144/GSL.SP.1989.045.01.08.Schroll E., Köppel V. and Cerny I. (2006) Pb and Sr isotope and geochemical data from the Pb-Zn deposit Bleiberg (Austria): Constraints on the age of mineralization. Mineralogy and Petrology, 86, 129-156, https://doi.org/10.1007/s00710-005-0107-3.

Schulz O. (1964) Lead-zinc deposits in the Calcareous Alps as an example of submarine hydrothermal

https://doi.org/10.1180/mgm.2025.10124 Published online by Cambridge University Press

formation of mineral deposits. Developments in Sedimentology, 2, 47-52, https://doi.org/10.1016/S0070-4571(08)70528-4.

Schwinn G. and Markl G. (2005) REE systematics in hydrothermal fluorite. Chemical Geology, 216, 225-248, https://doi.org/10.1016/j.chemgeo.2004.11.012.

Searl A. (1989) Saddle dolomite: a new view of its nature and origin. Mineralogical Magazine, 53(373), 547-555, https://doi.org/10.1180/minmag.1989.053.373.05.

Sharp J.M.J. (1978) Energy and momentum transport model of the Ouachita basin and its possible impact on formation of economic mineral deposits. Economic Geology, 73, 1057-1068, https://doi.org/10.2113/gsecongeo.73.6.1057.

Shields G.A. and Webb G.E. (2004) Has the REE composition of seawater changed over geological time? Chemical Geology, 204, 103-107, 10.1016/j.chemgeo.2003.09.010.

Simms M.J. and Ruffell A.H. (1989) Synchroneity of climatic change and extinctions in the Late Triassic. Geology, 17, 265-268, https://doi.org/10.1130/0091-7613(1989)017<0265:SOCCAE>2.3.CO;2.

Simms M.J. and Ruffell A. (2018) The Carnian Pluvial Episode: From discovery, through obscurity, to acceptance. Journal of the Geological Society, 175, 989-992, https://doi.org/10.1144/jgs2018-020.

Sirat M., Al-Aasm I.S., Morad S., Aldahan A., Al-Jallad O., Ceriani A., Morad D., Mansurbeg H. and Al-Suwaidi A. (2016) Saddle dolomite and calcite cements as records of fluid flow during basin evolution: Paleogene carbonates, United Arab Emirates. Marine and Petroleum Geology, 74, 71-91, https://doi.org/10.1016/j.marpetgeo.2015.11.005.

Spangenberg J.E., Fontbote L. and Macko S.A. (1999) An evaluation of the inorganic and organic geochemistry of the San Vicente mississippi valley-type zinc-lead district, central Peru; implications for ore fluid composition, mixing processes, and sulfate reduction. Economic Geology, 94, 1067-1092, https://doi.org/10.2113/gsecongeo.94.7.1067.

Spangenberg J.E. and Herlec U. (2006) Hydrocarbon Biomarkers in the Topla-Mezica Zinc-Lead Deposits, Northern Karavanke/Drau Range, Slovenia: Paleoenvironment at the Site of Ore Formation. Economic Geology, 101, 997-1021, https://doi.org/10.2113/gsecongeo.101.5.997.

Spencer R.J., Jeary V. and Moore S.L.O. (2004) Sedimentary exhalative dolomite from the Middle Cambrian Eldon and Cathedral formations of the Canadian Rocky Mountains. In: *Dolomites - The spectrum: Mechanisms, models, reservoir development* (R. McAuley, editor), Canadian Society of Petroleum Geologists, Seminar and

https://doi.org/10.1180/mgm.2025.10124 Published online by Cambridge University Press

Core Conference, January 13-15, 2004, Calgary, Extended Abstracts, CD format.

Stacey J., Wallace M., Reed C., Moynihan C., Leonard W. and Hood A. (2022) A novel chemical model for burial diagenesis and Zn-Pb sulphide precipitation within the Carboniferous Waulsortian Limestone, Ireland. Sedimentary Geology, 442, 106297, https://doi.org/10.1016/j.sedgeo.2022.106297.

Sverjensky D.A. (1984) Europium redox equilibria in aqueous solution. Earth and Planetary Science Letters, 67(1), 70-78, https://doi.org/10.1016/0012-821X(84)90039-6.

Sverjensky D.A. (1984) Oil field brines as ore-forming solutions. Economic Geology, 79, 23-27, https://doi.org/10.2113/gsecongeo.79.1.23.

Sverjensky D.A. (1986) Genesis of Mississippi Valley-type lead-zinc deposits. Annual Review of Earth and Planetary Sciences, 14, 177-199, https://doi.org/10.1146/annurev.ea.14.050186.001141.

Swart P.K. (2015) The geochemistry of carbonate diagenesis: The past, present and future. Sedimentology, 62, 1233-1304, https://doi.org/10.1111/sed.12205.

Sylvestre G., Evine Laure N.T., Gus Djibril K.N., Arlette D.S., Cyriel M., Timolèon N. and Jean Paul N. (2017) A mixed seawater and hydrothermal origin of superior-type banded iron formation (BIF)-hosted Kouambo iron deposit, Palaeoproterozoic Nyong series, Southwestern Cameroon: constraints from petrography and geochemistry. Ore Geology Reviews, 80, 860-875, https://doi.org/10.1016/j.oregeorev.2016.08.021.

Takahashi Y., Yoshida H., Sato N., Hama K., Yusa Y. And Shimizu H. (2002) W- and M-type tetrad effects in REE patterns for water–rock systems in the Tono uranium deposit, central Japan. Chemical Geology, 184(3-4), 311-335, https://doi.org/10.1016/S0009-2541(01)00388-6.

Tavazzani L., Guillong M., Giuliani A., Fontboté L. and Chelle-Michou C. (2024) Not so fast: Million-years of metal precipitation in Mississippi Valley type deposits inferred from in-situ petrochronology of hydrothermal carbonates. Earth and Planetary Science Letters, 636, 118718, https://doi.org/10.1016/j.epsl.2024.118718.

Taylor S.R. and McLennan S.M. (1981) The composition and evolution of the continental crust: rare earth element evidence from sedimentary rocks. Philosophical Transactions of the Royal Society of London. Series A, Mathematical and Physical Sciences, 301, 381-399, http://doi.org/10.1098/rsta.1981.0119.

Taylor S.R. (1984) Structural and paleotopographic controls of lead-zinc mineralization in the Silvermines orebodies, Republic of Ireland. Economic Geology, 79, 529-548, https://doi.org/10.2113/gsecongeo.79.3.529.

Taylor S.R. and McLennan S.M. (1985) *The Continental Crust: its composition and evolution*. Blackwell, Malden, Mass, 1985.

https://doi.org/10.1180/mgm.2025.10124 Published online by Cambridge University Press

Trombetta G.L. (2013) Paleogeografia del Triassico superiore delle Prealpi Bergamasche: nuovi dati sul rifting norico nel Bacino Lombardo. Quaderni del Museo di Storia Naturale di Ferrara, 1, 11-24.

Tucker M.E. and Wright V.P. (1990) *Carbonate Sedimentology*. Blackwell Publishing, Oxford, UK, 482 pp.

Vachè R. (1966) Ricerche microstratigrafiche sul Metallifero di Gorno (Prealpi Bergamasche). Rivista Italiana di Paleontologia e Stratigrafia, 72, 53-144.

Vailati G. (1966) Concentrazioni di minerali di piombo e zinco legate a fenomeni tettonici nel giacimento di Gorno. Simp. Int. Giacim. Min. d'Alpi, Trento-Mendola 11-18 Settembre 1966, 183-204.

Van Kranendonk M.J., Webb G.E. and Kamber B.S. (2003) Geological and trace element evidence for a marine sedimentary environment of deposition and biogenicity of 3.45 Ga stromatolitic carbonates in the Pilbara Craton, and support for a reducing Archaean Ocean. Geobiology, 1, 91-108, https://doi.org/10.1046/j.1472-4669.2003.00014.x.

Veizer J., Ala D., Azmy K., Bruckschen P., Bruhn F., Buhl D., Carden G., Diener A., Ebneth S., Goddris Y., Jasper T., Korte C., Pawellek F., Podlaha O. and Strauss H. (1999) $^{87}Sr/^{86}Sr$, $\delta^{13}C$ and $\delta^{18}O$ evolution of Phanerozoic seawater. Chemical Geology, 161, 59-88, https://doi.org/10.1016/S0009-2541(99)00081-9.

Wang J., Williams-Jones A.E., Timofeev A., Zhang X., Liu J. and Yuan S (2023) The role of scandium chloride and hydroxyde complexes in the formation of scandium deposits: insights from experiments and modeling. Economic Geology, 118, 1995-2004, https://doi.org/10.5382/econgeo.5026.

Warren J. (2000) Dolomite: occurrence, evolution and economically important associations. Earth-Sciences Reviews, 52(1-3), 1-81, https://doi.org/10.1016/S0012-8252(00)00022-2.

White D.E. (1957) Thermal waters of volcanic origin. Geological Society of America Bulletin, 68, 1637-1658, https://doi.org/10.1130/0016-7606(1957)68[1637:TWOVO]2.0.CO;2.

Wilkinson J.J. (2003) On diagenesis, dolomitisation and mineralisation in the Irish Zn-Pb orefield. Mineralium Deposita, 38, 968-983, https://doi.org/10.1007/s00126-003-0387-7.

Wilkinson J.J., Eyre S.L. and Boyce A.J. (2005a) Ore-forming processes in Irish-type carbonate-hosted Zn-Pb deposits: Evidence from mineralogy, chemistry and isotopic composition on of sulfides at the Lisheen Mine. Economic Geology, 100, 63-86, https://doi.org/10.2113/100.1.0063.

Wilkinson J.J., Everett C.E., Boyce A.J., Gleeson S.A. and Rye D.M. (2005b) Intracratonic crustal seawater circulation and the genesis of sub-seafloor Zn-Pb mineralization in the Irish orefield. Geology, 33, 805-808, https://doi.org/10.1130/G21740.1.

https://doi.org/10.1180/mgm.2025.10124 Published online by Cambridge University Press

Wilkinson J.J. (2014) Sediment-hosted zinc-lead mineralization: processes and perspectives. Pp. 219-249 in: *Treatise on Geochemistry, 2* (H.D. Holland and K.K Turekian, editors), https://doi.org/10.1016/B978-0-08-095975-7.01109-8.

William-Jones A.E., Migdisov A.A. and Samson I.M. (2012) Hydrothermal Mobilisation of the Rare Earth Elements – a Tale of "Ceria" and "Yttria". Elements, 8(5), 355-360, https://doi.org/10.2113/gselements.8.5.355.

Williams-Jones A.E. and Vasyukova O.V. (2018) The economic geology of scandium, the runt of the rare earth element litter. Economic Geology, 113, 973-988, https://doi.org/10.5382/econgeo.2018.4579.

Winterer E.L. and Bosellini A. (1981) Subsidence and Sedimentation on Jurassic Passive Continental Margin, Southern Alps, Italy. AAPG Bulletin, 65(3), 394-421, https://doi.org/10.1306/2F9197E2-16CE-11D7-8645000102C1865D.

Worden R.H., Smalley P.C. and Oxtoby N.H. (1995) Gas sowing by thermochemical sulfate reduction at 140°C. American Association of Petroleum Geology, section B, 79, 854-863, https://doi.org/10.1306/8D2B1BCE-171E-11D7-8645000102C1865D.

Xing Y., Etschmann B., Liu W., Mei Y., Shvarov Y., Testemale D., Tomkins A. and Brugger J. (2019) The role of fluorine in hydrothermal mobilization and transportation of Fe, U and REE and the formation of IOCG deposits. Chemical Geology, 504, 158-176, https://doi.org/10.1016/j.chemgeo.2018.11.008.

Zanchetta S., Garzanti E., Doglioni C. and Zanchi A. (2012) The Alps in the Cretaceous: a doubly vergent pre-collisional orogen. Terra Nova, 24, 351-356, https://doi.org/10.1111/j.1365-3121.2012.01071.x.

Zeeh S., Kuhlemann J. and Bechstädt T. (1998) The classical Pb-Zn deposits of the Eastern Alps (Austria/Slovenia) revisited: MVT deposits resulting from gravity driven fluid flow in the Alpine Realm. Geologija, 41, 257-273, https://doi.org/10.5474/geologija.1998.014.

https://doi.org/10.1180/mgm.2025.10124 Published online by Cambridge University Press

Figure. 1. (a) and (b) Location of the study area (red square) in Northern Italy and in Lombardy region, respectively: I = Italy; CH = Switzerland. (c) Geological sketch of the central Southern Alps domain in Lombardy. The Dossena mine district area is marked by the red star in the Triassic sedimentary rock outcrops. (d) Geological sketch detailing the study area, with outcrops of the Middle-Upper Triassic sedimentary succession. Historical mine districts are marked by the hammer symbols: Pb-Zn sulfides, fluorite and baryte mineralization are exploited in the Esino Limestone, Breno Formation, Calcare Metallifero Bergamasco and Gorno Formation.

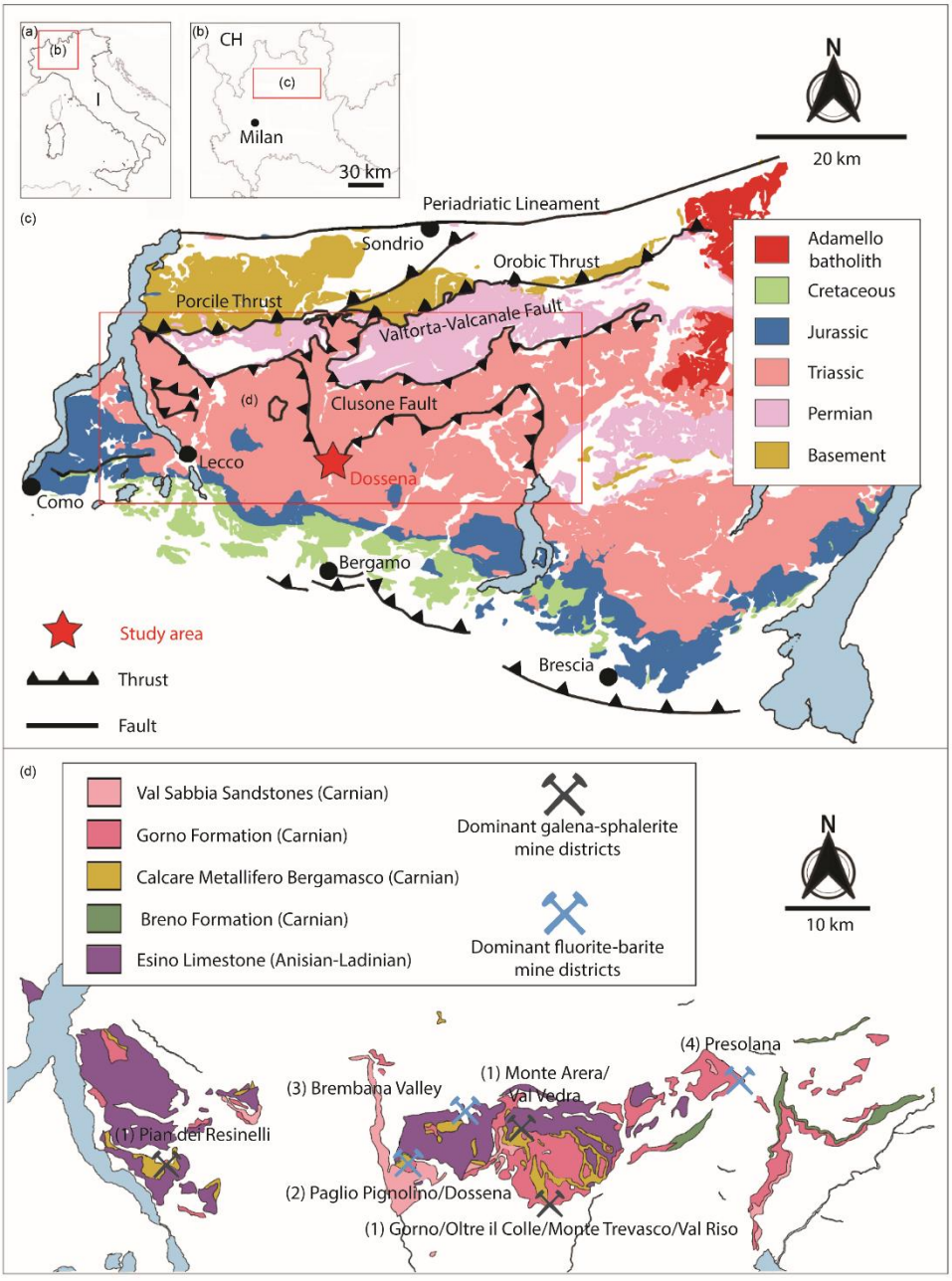

https://doi.org/10.1180/mgm.2025.10124 Published online by Cambridge University Press

Figure. 2. Stratigraphic scheme and lithostratigraphic units of the sedimentary succession in the Lombardy Basin overlying the Variscan metamorphic basement (Pre-Pennsylvanian) from the Permian to the Upper Triassic Riva di Solto Shales (upper Norian), modified after Forcella et al. (2012) and Jadoul et al. (2012). CGB = Basal Conglomerate; VUC = Monte Cabianca volcaniclastic rocks; FPZ = Pizzo del Diavolo Formation; VER = Verrucano Lombardo; SRV = Servino Formation; BOV = Carniola di Bovegno; ANG = Angolo Limestone; CAM = Camorelli Limestone; PRZ = Prezzo Limestone; BUC = Buchenstein Formation; WEN = Wengen Formation; PTO = Pratotondo Limestone; LOZ = Lozio Shale; ESI = Esino Limestone; KLR = Calcare Rosso; BRE = Breno Formation; CMB = Calcare Metallifero Bergamasco; SAB = Val Sabbia Sandstones; GOR = Gorno Formation; SGB = San Giovanni Bianco Formation; CSO = Castro Sebino Formation; DPR = Dolomia Principale; DZN = Dolomie Zonate; ZOR = Zorzino Limestone; ARS = Riva di Solto Shales. The Dossena mine district is indicated by the hammer symbol.

https://doi.org/10.1180/mgm.2025.10124 Published online by Cambridge University Press

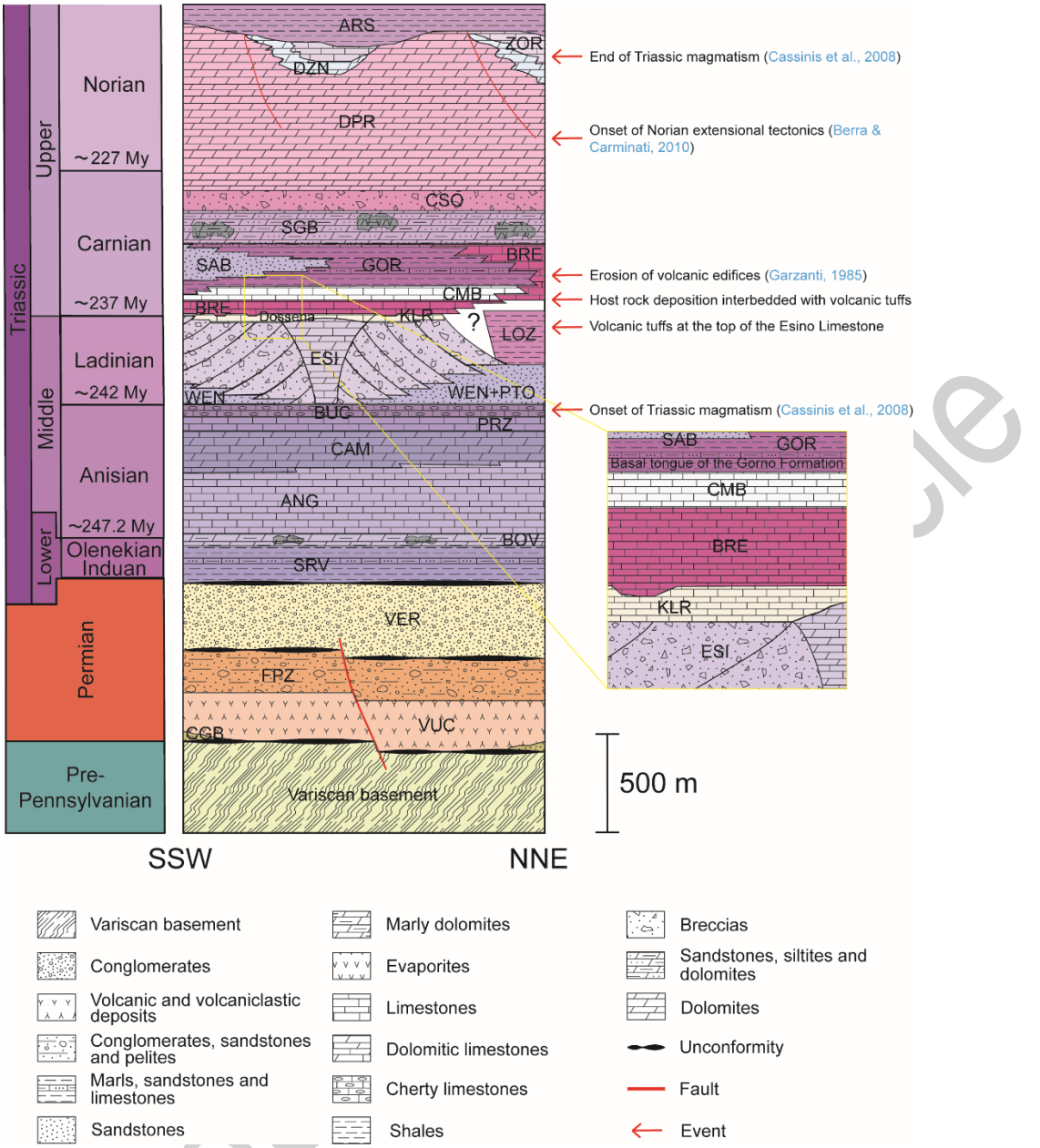

Figure. 3. (a) and (b) Photomicrographs in plane polarizer and in CL, respectively: Cal 0 peloidal skeletal packstone-wackestone (dull red) and Cal 1 blocky sparite filling primary voids (non-luminescent) cross-cut by fractures filled by bright orange luminescent Cal 6 sparite to microsparite. (c) Plane polarizer image displaying framboidal pyrite crystals dispersed within the Cal 0 host rock. (d) Outcrop photograph showing the intertidal facies of the BRE with fenestrae occluded by Cal 1 and cross-cut by fractures filled by Dol 1 saddle dolomite. Stylolite 1 post-dates the fractures filled by Dol 1. (e) and (f) Plane polarizer and CL photomicrographs of millimetre-size vugs filled by limpid blocky sparite cement: Cal 2 (non-luminescent cores and bright orange rims), Cal 3 (dull red) and Cal 4 (bright orange to zoned dull red-bright orange). (g) Fracture filled by Dol 1 saddle dolomite cement across Cal 0 and vugs filled by Cal 2+3+4. Cal 5 equant calcite overlies and fills porosity

https://doi.org/10.1180/mgm.2025.10124 Published online by Cambridge University Press

between Dol 1 crystals in the same fractures hosting saddle dolomite. (h) Image in crossed polarizer showing the undulose extinction of Dol 1 saddle dolomite.

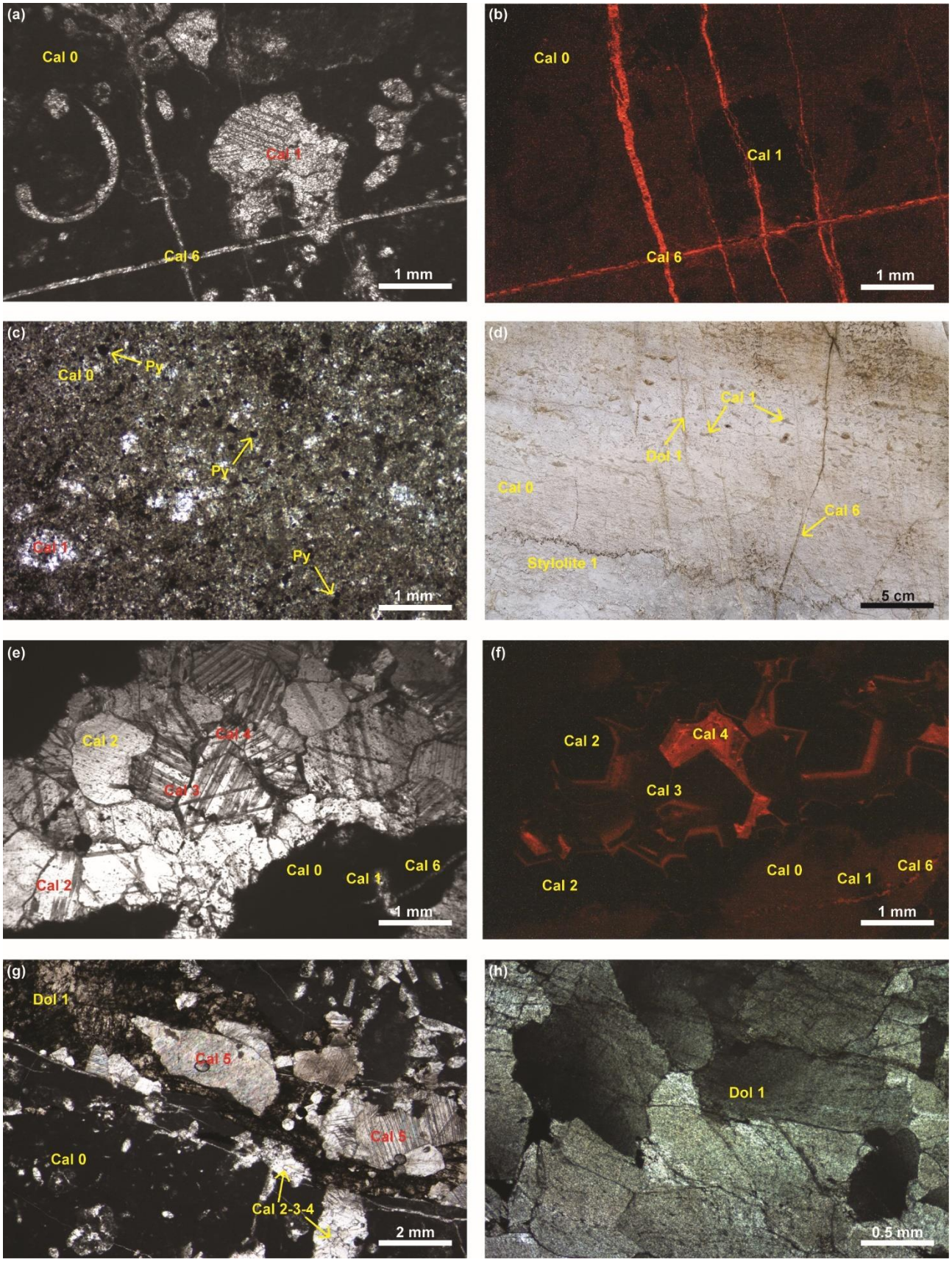

https://doi.org/10.1180/mgm.2025.10124 Published online by Cambridge University Press

Figure. 4. (a) and (b) Photomicrographs in polarized light and CL showing Dol 1 saddle dolomite cement (dull red) in fractures across Cal 0 (dull red). Cal 5 calcite (zoned non-luminescent cores with bright orange and dull red to non-luminescent rims) overlies Dol 1 in the same fractures and are both crossed by fractures filled by bright orange Cal 6 sparite to microsparite. (c) and (d) Plane polarizer and CL photomicrographs showing Cal 5 equant calcite (dull red) filling intercrystal pores of Dol 1, cross-cut by Cal 6 fracture filling sparite to microsparite (bright orange). (e) and (f) Photomicrographs in plane polarizer and CL showing Cal 6 (bright orange) and Cal 7 sparite (quenched with respect to Cal 6) cutting through Dol 1 saddle dolomite (dull red). Cal 5 (dull orange) fills the intercrystal voids between Dol 1 and Cal 6 partially replaces Dol 1, resulting in spotted bright portions on Dol 1 crystals. Euhedral hexagonal bipyramidal quartz (Qz, non-luminescent) overlies Cal 7. (g) and (h) Plane polarizer and CL photomicrographs detailing Dol 1 saddle dolomite (dull red) cross-cut in sequence by Cal 6 (bright orange) and Cal 7 (quenched with respect to Cal 6). Euhedral hexagonal bipyramidal quartz (Qz, non-luminescent) on Cal 7 sparite.

https://doi.org/10.1180/mgm.2025.10124 Published online by Cambridge University Press

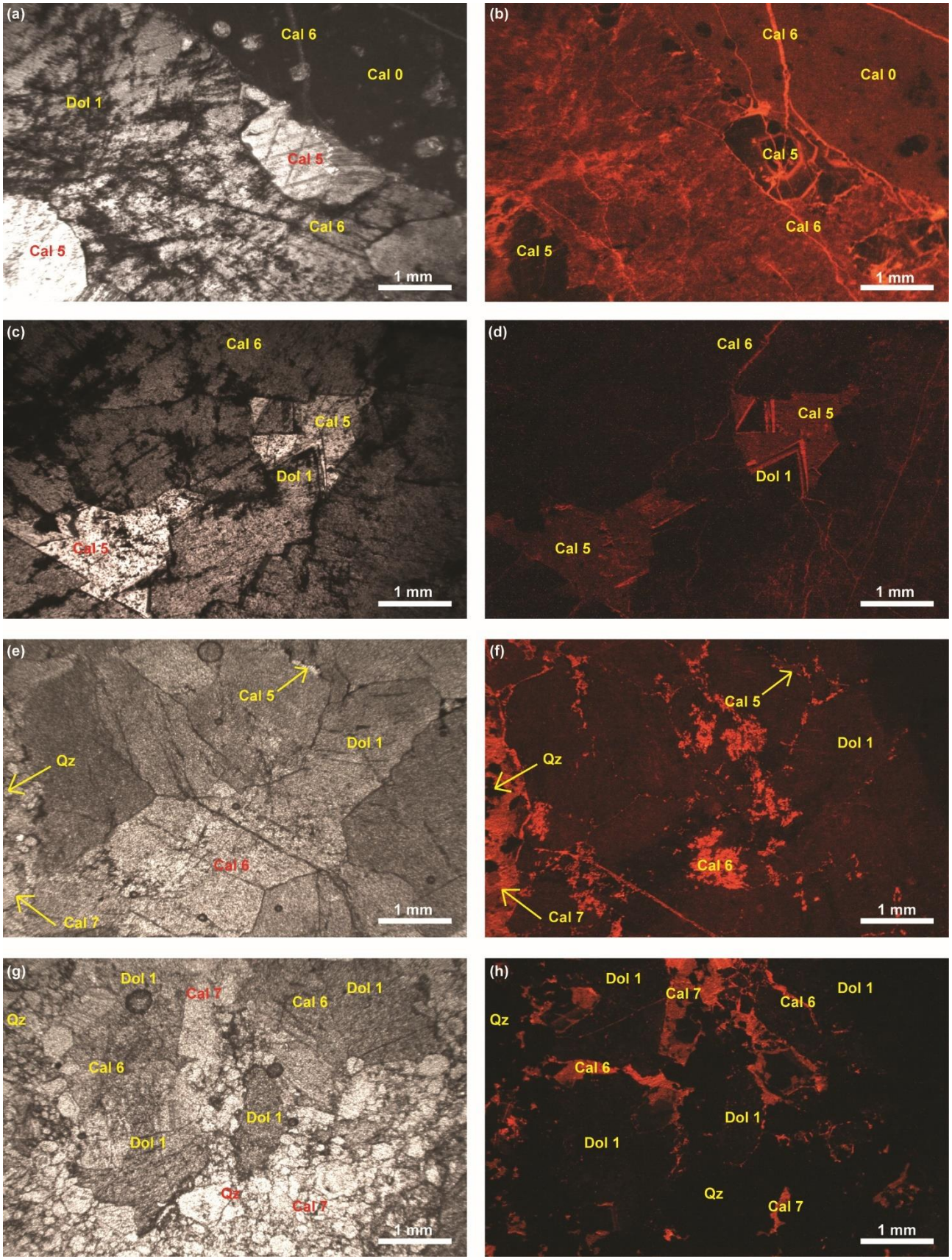

https://doi.org/10.1180/mgm.2025.10124 Published online by Cambridge University Press

Figure. 5. (a) Outcrop image showing Cal 6 sparite filling fractures brecciating Dol 1 saddle dolomite. (b) Outcrop photo showing the relationships between Cal 0 host rock, Cal 6 sparite, sphalerite, galena and fluorite. This mineralisation is associated with limpid white Cal 6 sparite cement, which is cross-cut by Cal 7 sparite with euhedral hexagonal bipyramidal quartz (Qz). (c) and (d) Thin section photographs in plane polarizer and in CL displaying fluorite crystal precipitated in Cal 6 intercrystal porosity. (e) Cal 7 sparite stained in pink by alizarin red-S and K-ferricyanide and euhedral hexagonal bipyramidal quartz (Qz) cross-cutting in microfractures fluorite crystals (Fl). (f) Thin section image in plane polarized light showing Cal 7 sparite cement stained in pink and euhedral hexagonal bipyramidal quartz cutting through Dol 1 saddle dolomite in fractures. (g) Outcrop photograph showing Cal 7 calcite and bipyramidal quartz (Qz). (h) Plane polarized photomicrograph of Cal 0 fragments brecciated by Cal 7 sparite and euhedral quartz (Qz), while stylolite 1 follows Qz.

https://doi.org/10.1180/mgm.2025.10124 Published online by Cambridge University Press

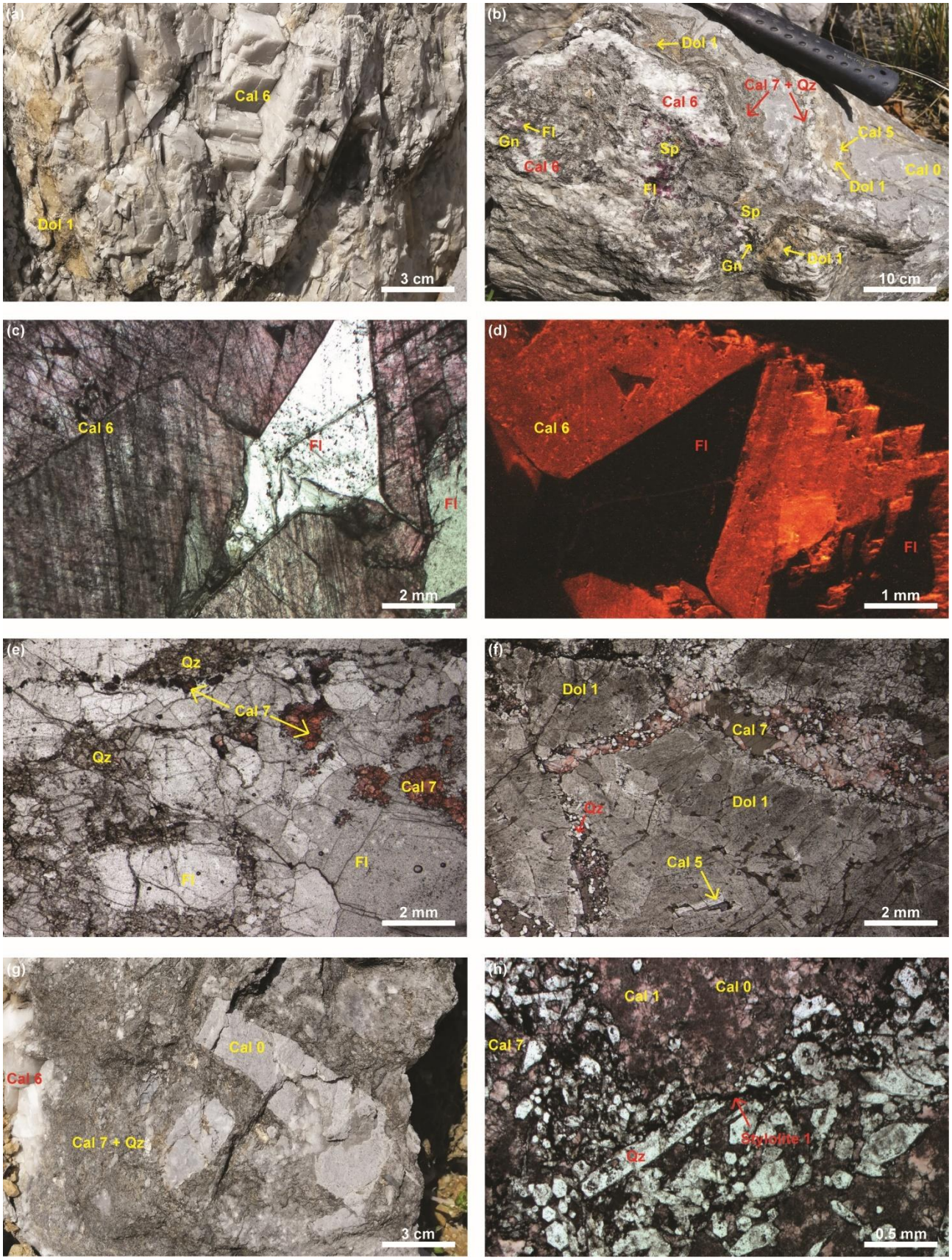

https://doi.org/10.1180/mgm.2025.10124 Published online by Cambridge University Press

Figure. 6. Paragenetic sequences identified in the Breno Formation (a) and in the Calcare Metallifero Bergamasco (b). Red colour marks the diagenetic events comprised between the saddle dolomite and the sphalerite, galena and fluorite precipitation. CL = cathodoluminescence; DL = dull luminescent; NL = non-luminescent; BL = bright luminescent; PL = patchy luminescent.

https://doi.org/10.1180/mgm.2025.10124 Published online by Cambridge University Press

(a)

Breno Formation

Diagenetic setting	Diagenetic event (CL)	Pre-saddle dolomite	Saddle dolomite and mineralization	Post-mineralization
Marine	Cal 0 host rock (DL)			
Marine burial	Cal 1 blocky sparite filling primary voids and mouldic porosity (NL)			
Burial	Cal 2 blocky sparite filling dissolution vugs (NL cores and BL rims)			
	Cal 3 blocky sparite filling dissolution vugs after Cal 2 (DL)			
	Cal 4 blocky sparite filling dissolution vugs after Cal 3 (BL to zoned BL-DL)			
	Dol 1 saddle dolomite filling fractures cutting through Cal 0-4 (DL or zoned with DL cores and BL rims)			
	Cal 5 equant calcite overlying Dol 1 saddle dolomite and filling Dol 1 intercrystalline voids (zoned with NL cores and BL rims or NL to DL)			
	Cal 6 sparite to microsparite filling fractures and replacing Dol 1 saddle dolomite (BL)			
	Sphalerite, galena and fluorite			
	Cal 7 sparite filling fractures and overlying fluorite crystals (BL)			
	Euhedral hexagonal bipyramidal quartz			
	Stylolite 1			

(b)

Calcare Metallifero Bergamasco

Diagenetic setting	Diagenetic event (CL)	Pre-saddle dolomite	Saddle dolomite and mineralization	Post-mineralization
Marine	Cal 0 host rock (BL)			
Marine burial	Cal 1 blocky microsparite-sparite filling interparticle, mouldic and dissolution vugs (NL)			
Burial	Stylolite 1			
	Dol 1 replacive fabric destructive anhedral dolomicrosparite of Cal 0 (PL)			
	Silicification of Cal 0 by microquartz and fibrous chalcedony (NL)			
	Stylolite 2			
	Dol 2 saddle dolomite filling fractures or as sparse crystals in the silicified portions (zoned DL-NL cores and BL rims)			
	Cal 2 prismatic to equant calcite filling fractures after Dol 2, overlying saddle dolomite and occluding intercrystalline voids between saddle dolomite (BL)			
	Sphalerite, galena and fluorite			
	Cal 3 equant sparite filling fractures, replacing Cal 0, Dol 2, Cal 2 and overlying fluorite (BL)			
	Quartz mosaic filling intercrystalline porosity between sulphides and fluorite			
	Stylolite 3			

https://doi.org/10.1180/mgm.2025.10124 Published online by Cambridge University Press

Figure. 7. (a) Thin section image showing Cal 0 peloidal packstone with benthic foraminifers and Cal 1 blocky microsparite-sparite filling interparticle porosity. (b) Photomicrograph of Cal 0 peloidal skeletal packstone with bivalves with Cal 1 mouldic porosity filling limpid blocky microsparite-sparite and Cal 3 fracture filling equant sparite. (c) and (d) Photomicrographs in plane polarizer and CL displaying Cal 1 blocky sparite (non-luminescent) filling vugs in Cal 0 host rock (bright orange). Cal 0 and Cal 1 are cross-cut by Cal 3 fracture-filling equant sparite (bright orange). (e) and (f) Plane polarized and CL photomicrographs of Cal 3 fracture filling equant sparite (bright orange) cutting through Dol 1 replacive destructive dolomicrosparite mosaic (patchy luminescent). (g) Outcrop image showing silicified portions of the upper CMB, marked by arrows. (h) Silicified portions of Cal 0 host rock cross-cut by fractures filled in sequence by Dol 2 saddle dolomite cement (dark) and enlarged and filled by subsequent Cal 2 equant calcite, stained in pink by alizarin red-S and K-ferricyanide. Fractures filled with Cal 3 cross-cut and displace fractures filled by Cal 2.

https://doi.org/10.1180/mgm.2025.10124 Published online by Cambridge University Press

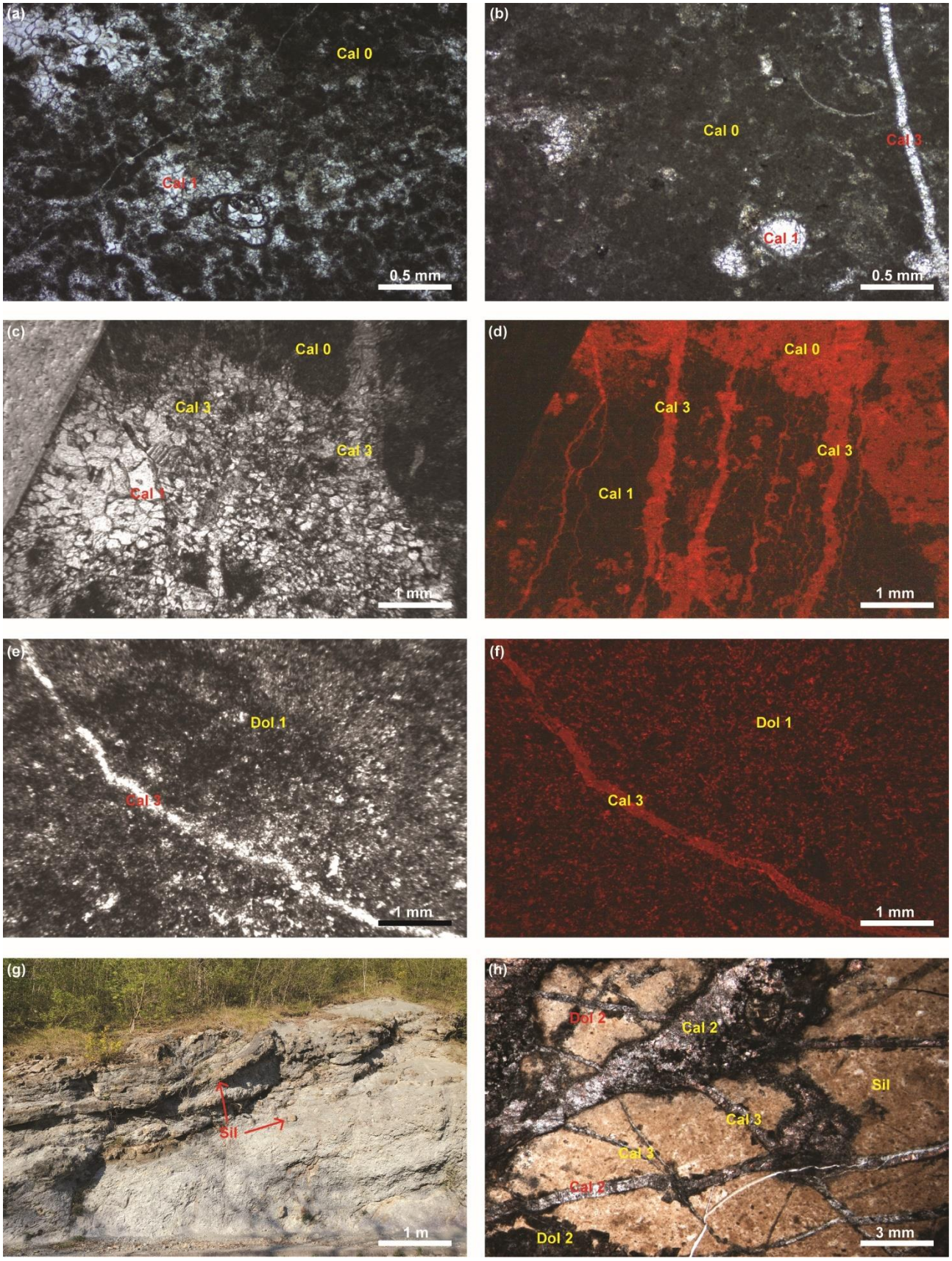

https://doi.org/10.1180/mgm.2025.10124 Published online by Cambridge University Press

Figure. 8. (a) and (b) Images in plane polarizer and CL displaying the silicification (Sil, non-luminescent) of the host rock crossed by fractures filled in sequence by Dol 2 saddle dolomite (non-luminescent) and Cal 2 equant calcite cement (bright luminescent). (c) and (d) Photomicrographs in plane polarized light and CL exhibiting Cal 2 sparite (bright luminescent) filling intercrystal voids between Dol 2 saddle dolomite (dull red) crystals, which are partially replaced by Cal 3, resulting in spotted brighter orange portions than Cal 2. (e) Crossed polarizer image of Dol 2 saddle dolomite with undulose extinction. Cal 2 and Cal 3 equant sparites cut through Dol 2. (f) Outcrop photograph displaying fractures with Cal 2 equant sparite overlying Dol 2 saddle dolomite, crossed by another set of fractures filled with Cal 3. (g) and (h) Photomicrographs in plane polarizer and CL detailing Cal 0 host rock (bright orange) cross-cut by fracture filled by Dol 2 saddle dolomite (dull red). Cal 2 prismatic to equant sparite (bright orange) overlies Dol 2 and are both crossed by Cal 3 (brighter orange than Cal 2).

https://doi.org/10.1180/mgm.2025.10124 Published online by Cambridge University Press

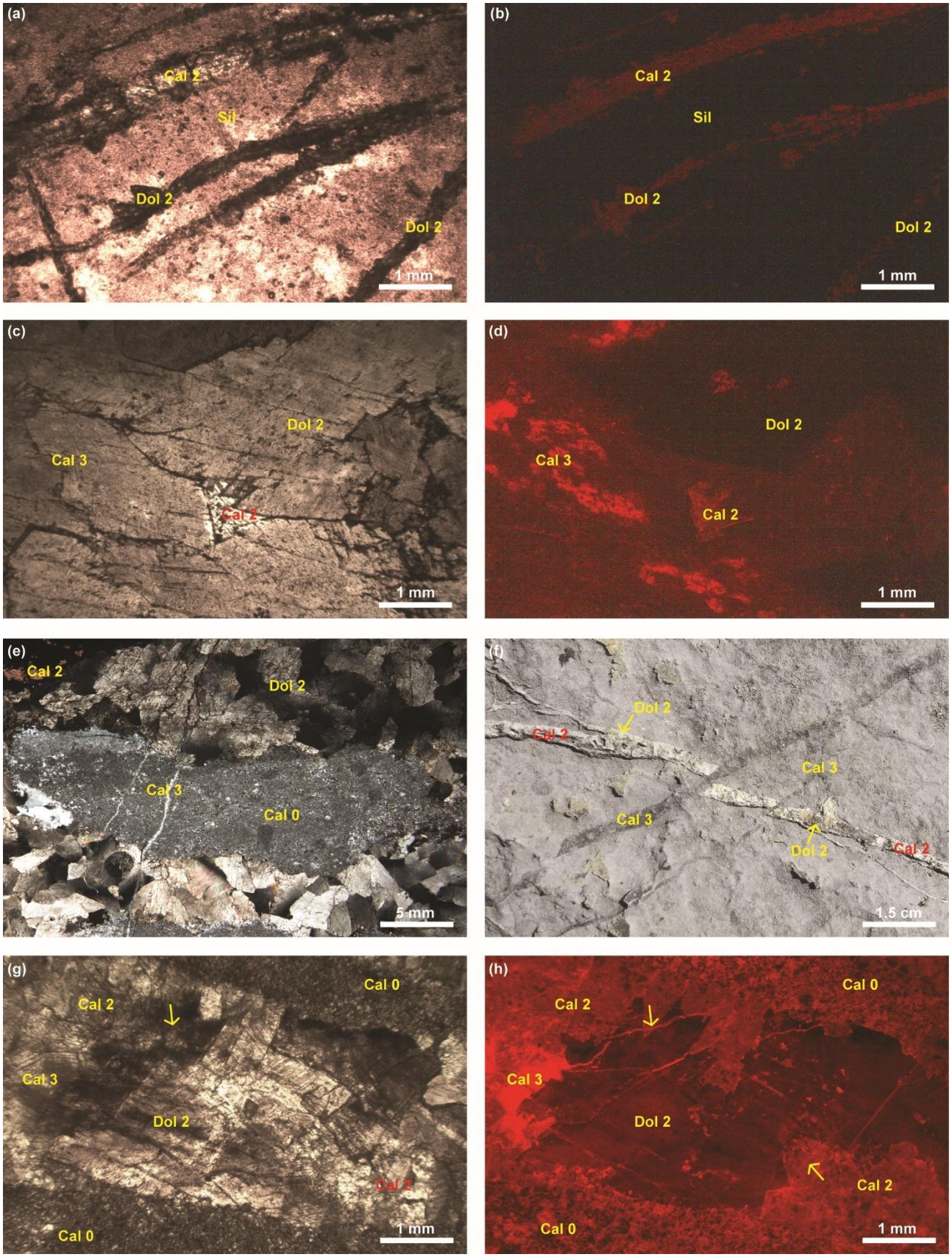

https://doi.org/10.1180/mgm.2025.10124 Published online by Cambridge University Press

Figure. 9. (a) Plane polarizer image displaying a fracture filled by Dol 2 saddle dolomite, partially replaced by Cal 2 sparite, cutting through a stylolite of the second set (yellow arrows). (b) Stained thin section detailing Cal 0 host rock and stylolites of the second set (yellow arrows) cut by fractures filled by Cal 2 prismatic cement (dashed yellow line) followed by fluorite crystals (Fl, white). (c) Photomicrograph in crossed polarizer showing a silicified portion of Cal 0 (Sil) and a stylolite of the second set (yellow arrows) cut by fractures filled in sequence by Dol 2 saddle dolomite and Cal 2 equant sparite. (d) Image in plane polarizer detailing a fracture filled by Cal 2 prismatic sparite and followed by euhedral sphalerite crystals (Sp). A fragment of shale is enclosed between the pre-ore calcite and the mineralisation (shale). (e) Fracture filled with fluorite (Fl, white) and cut by Cal 3 equant sparite cement (pink because of staining). Cal 3 euhedral crystals overlie fluorite on the right. The third set of stylolites separates fluorite from Cal 3. (f) Photograph in plane polarizer exhibiting Cal 0 peloidal packstone crossed by fractures filled by fluorite (Fl), cut in their turn by Cal 3 filled fractures. (g) and (h) Plane polarized and CL photomicrographs showing a fracture filled by Cal 2 prismatic to equant sparite (bright orange) and Cal 3 sparite cement (brighter than Cal 2) crossing Dol 1 replacive dolomicrosparite (patchy luminescent).

https://doi.org/10.1180/mgm.2025.10124 Published online by Cambridge University Press

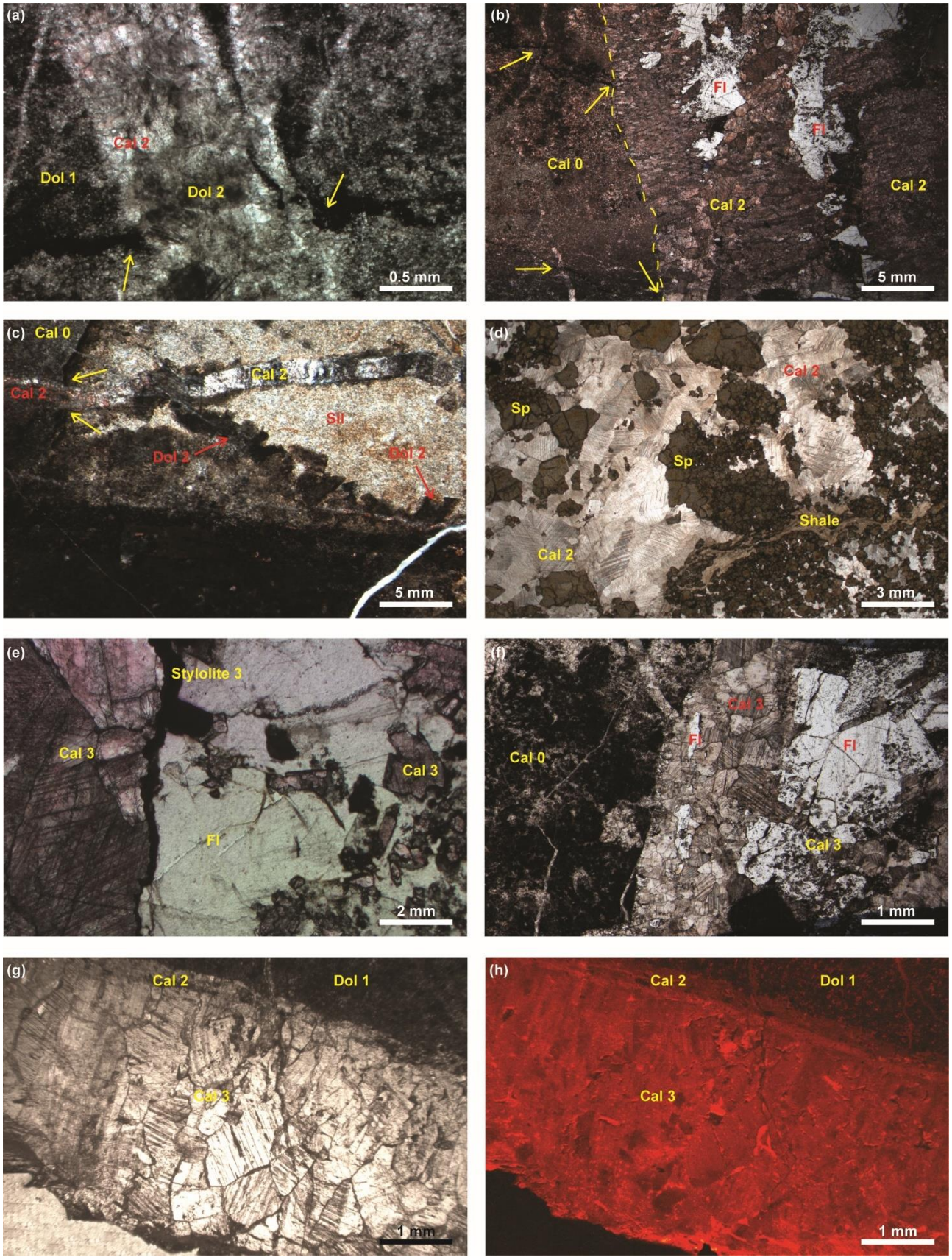

https://doi.org/10.1180/mgm.2025.10124 Published online by Cambridge University Press

Figure. 10. (a) Cross-plot of $\delta^{13}C$ and $\delta^{18}O$ of the analysed BRE Cal 0 + 1, Cal 2 + 3 + 4, Dol 1 saddle dolomite preceding mineralization, Cal 6 + 7 post-saddle dolomite carbonate phases. (b) Cross-plot of $\delta^{13}C$ and $\delta^{18}O$ of the analysed CMB Cal 0 + 1, Dol 1, Dol 2 saddle dolomite pre-mineralization, Cal 2 and Cal 3 post-saddle dolomite carbonate phases.

https://doi.org/10.1180/mgm.2025.10124 Published online by Cambridge University Press

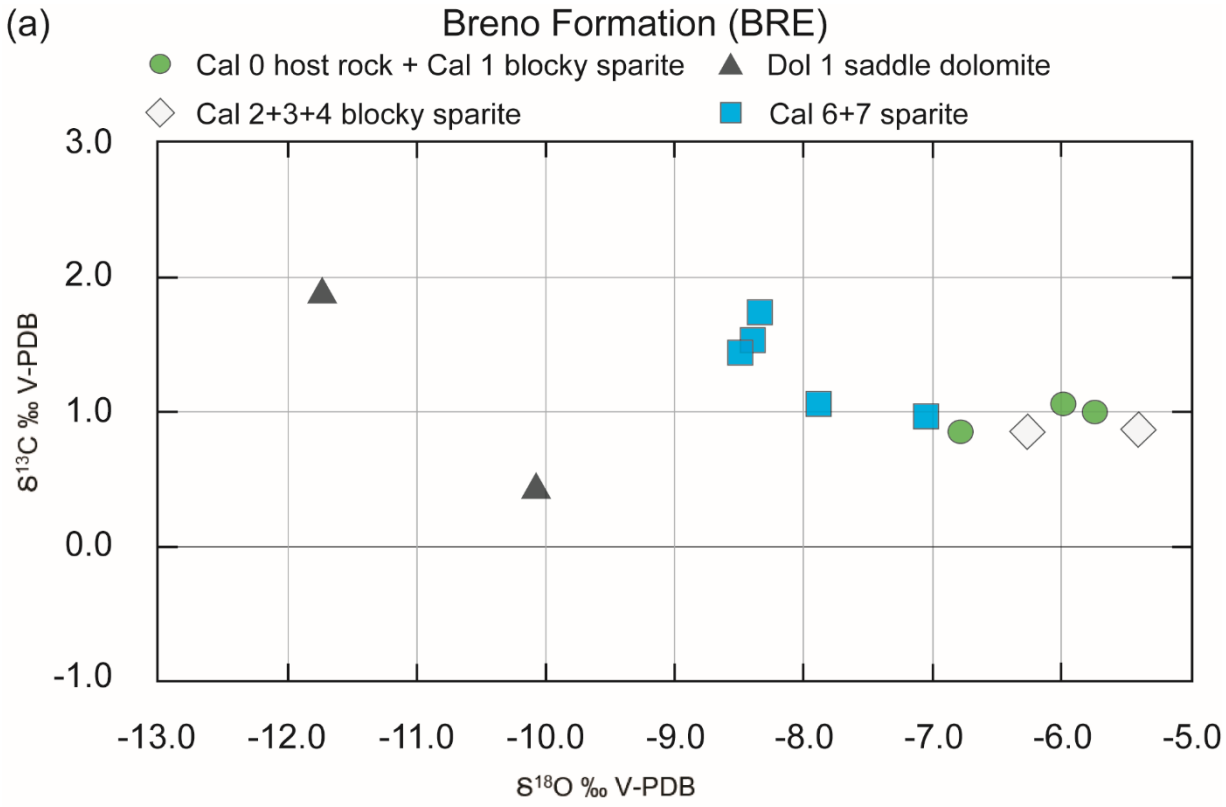

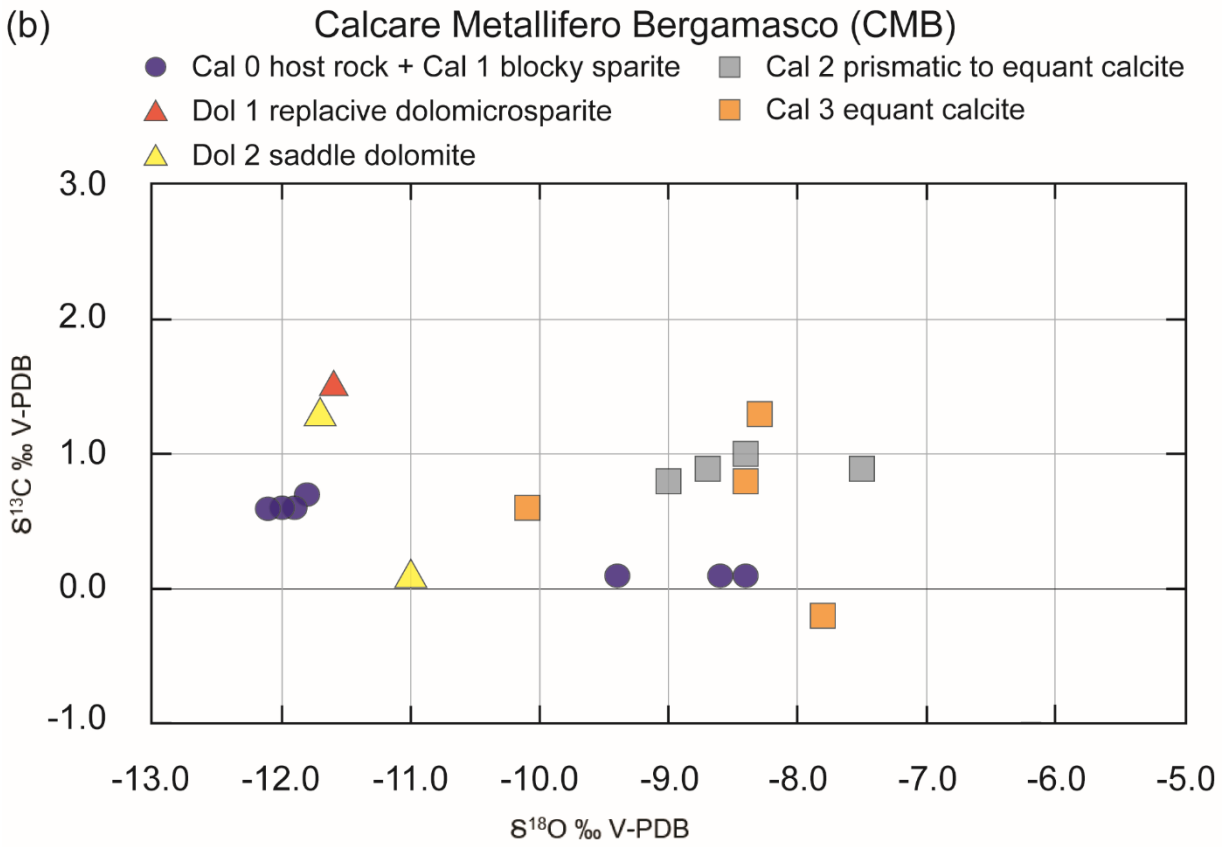

https://doi.org/10.1180/mgm.2025.10124 Published online by Cambridge University Press

Figure. 11. Plot of the $REEY_{SN}$ patterns normalised to PAAS (McLennan, 1989) of the BRE investigated carbonate phases.

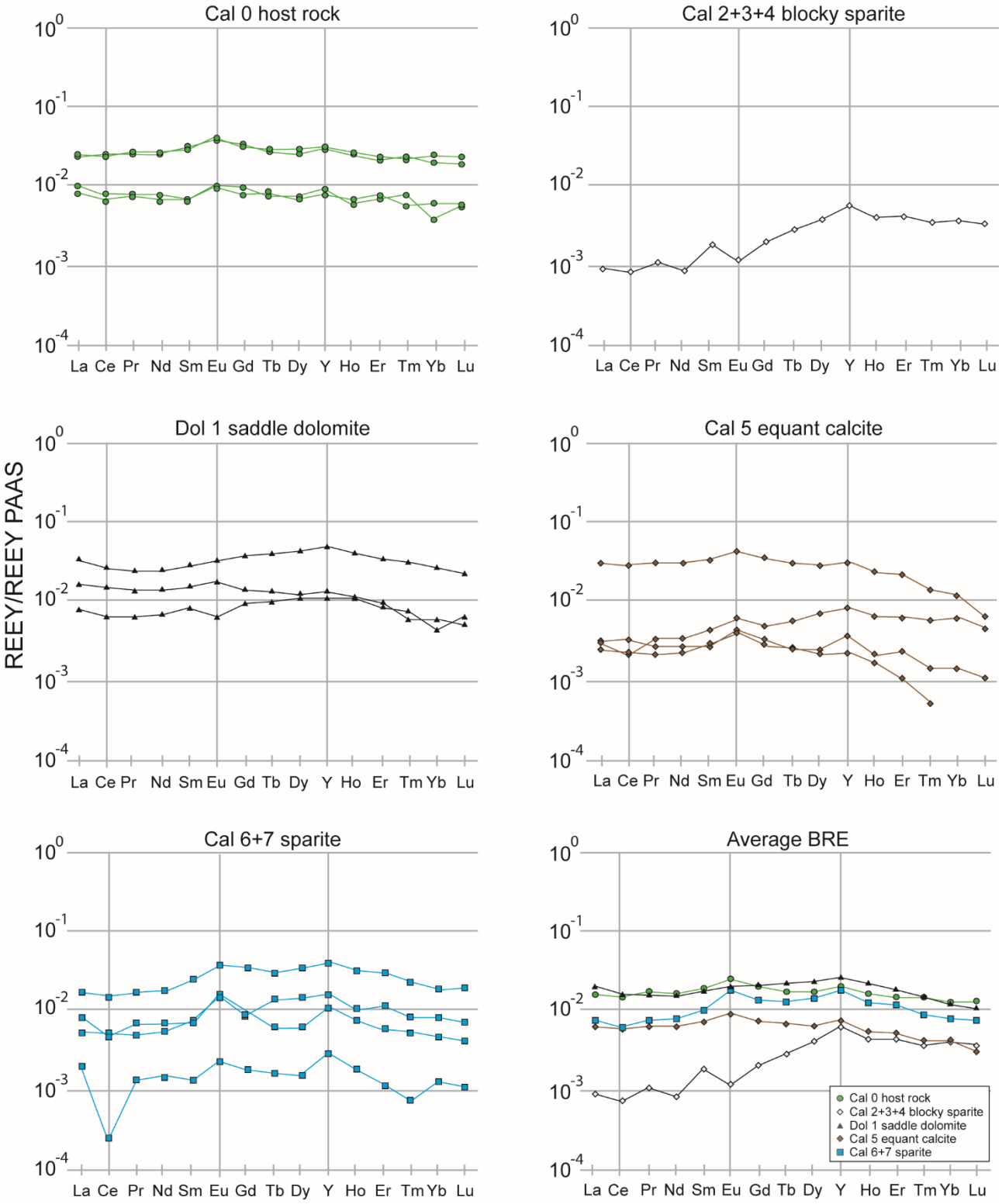

https://doi.org/10.1180/mgm.2025.10124 Published online by Cambridge University Press

Figure. 12. Plot showing the $REEY_{SN}$ patterns normalised to PAAS (McLennan, 1989) of the CMB investigated carbonate phases.

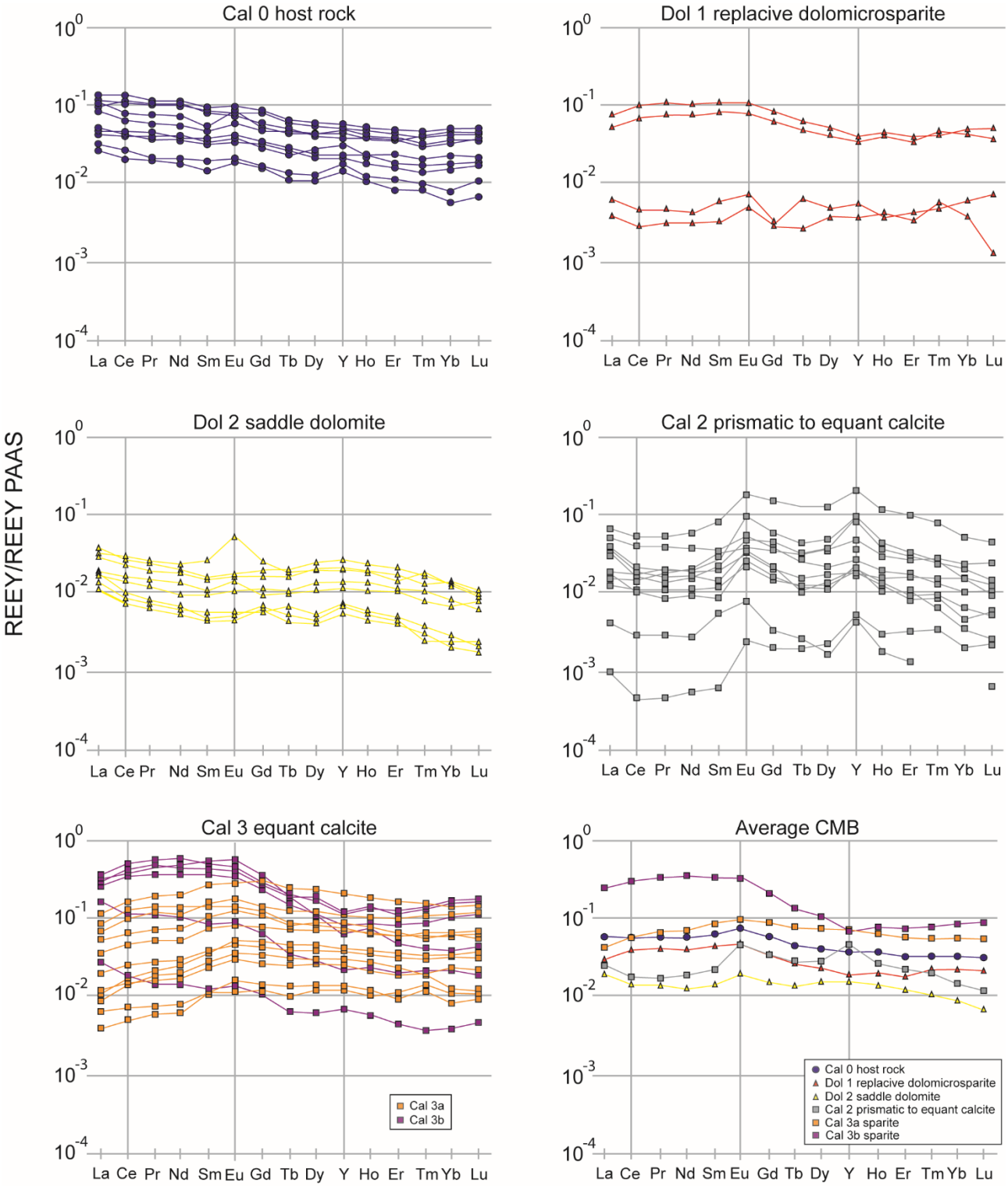

https://doi.org/10.1180/mgm.2025.10124 Published online by Cambridge University Press

Figure. 13. Box plot diagrams showing the abundances in ppm of different detected metals in the BRE and CMB carbonate phases: (a) Zn; (b) Pb; (c) Ba; (d) Cu; (e) V; (f) U; (g) Sc.

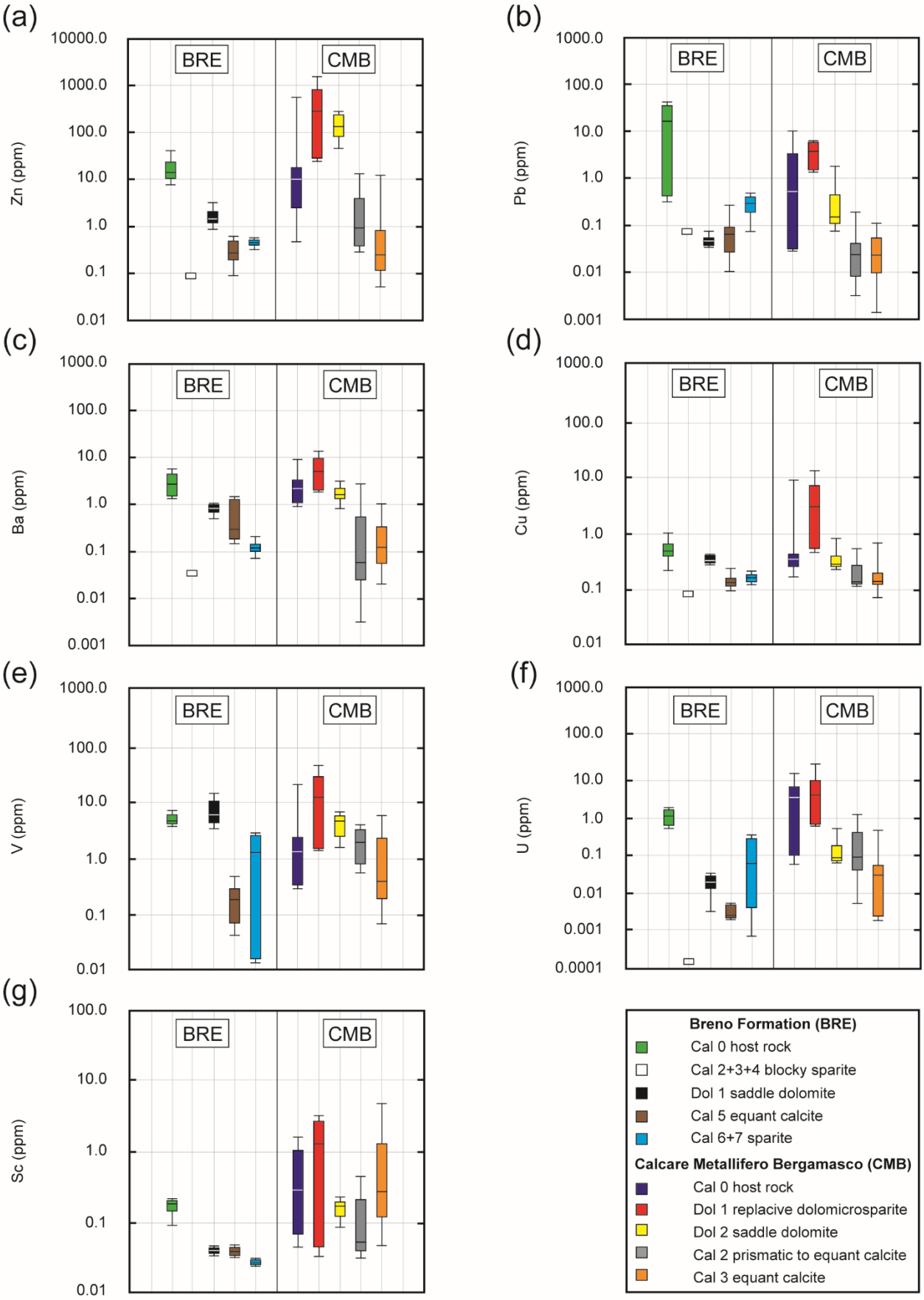

https://doi.org/10.1180/mgm.2025.10124 Published online by Cambridge University Press

Figure. 14. Comparative diagram of the average BRE and CMB REEY patterns of the investigated carbonate phases normalised to PAAS (McLennan, 1989) and C-1 carbonaceous chondrite (Taylor and McLennan, 1981). Reference material REEY normalised patterns are supplied: modern seawater (Alibo and Nozaki, 1999); low temperature hydrothermal fluids (Alexander et al., 2008); high temperature hydrothermal fluids (Bau and Dulski, 1999); Upper Continental Crust (Taylor and McLennan, 1981); Fe-Mn crusts and nodules (Bau et al., 1996).

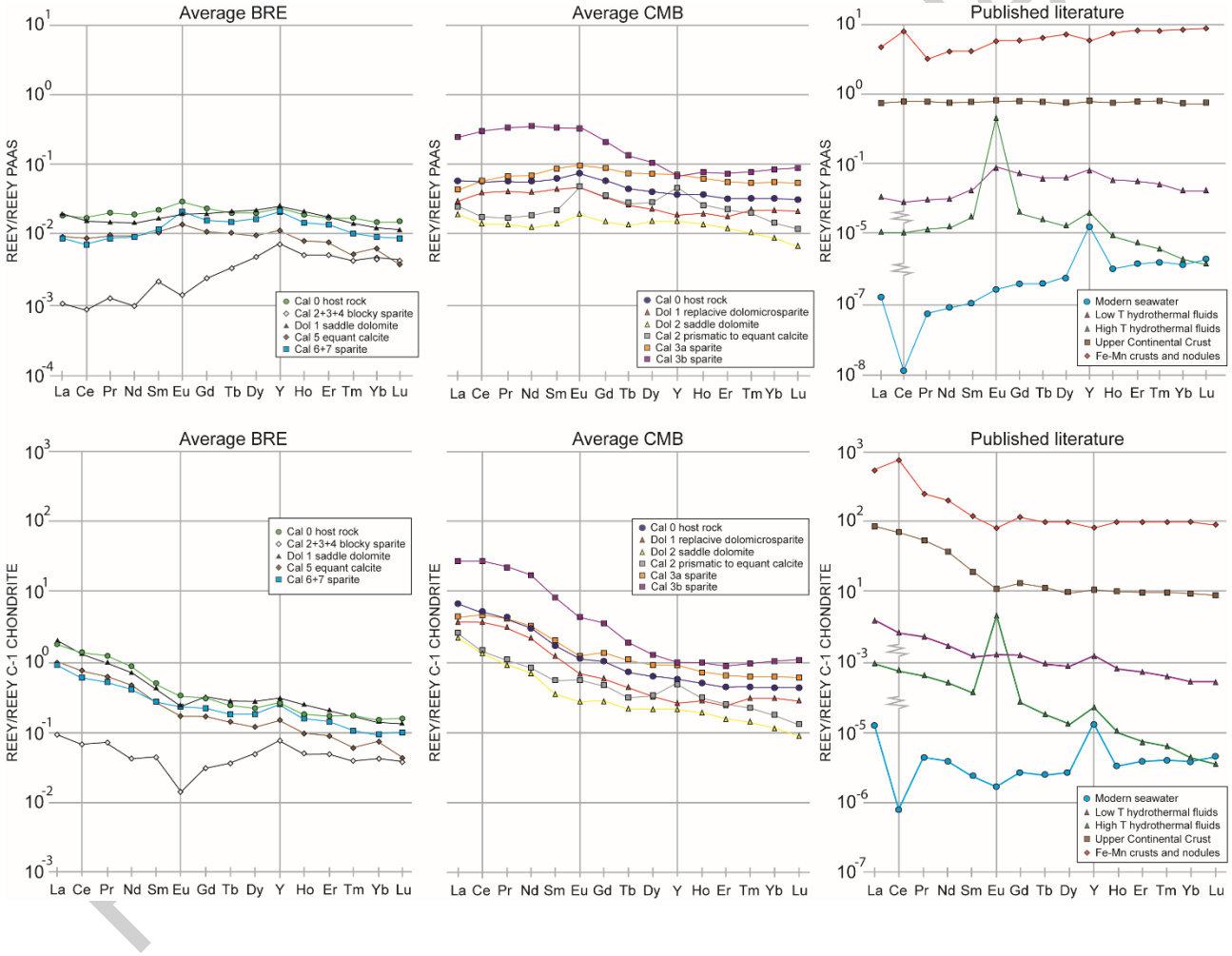

https://doi.org/10.1180/mgm.2025.10124 Published online by Cambridge University Press

Figure. 15. (a) Cross plot of PAAS normalised Pr/Pr^*_{SN} (Lanthanum anomaly) versus Ce/Ce^*_{SN} values of the carbonate phases identified and studied in the BRE and CMB, modified after Bau and Dulski (1996) and Navarro-Ciurana et al. (2023). Pink and violet colour areas correspond to present day hydrothermal fluids and seawater compositions, respectively. Field I = neither Ce/Ce^*_{SN} and La/La^*_{SN} anomalies; Field IIa = positive La/La^*_{SN} anomaly, no Ce/Ce^*_{SN} anomaly; Field IIb = negative La/La^*_{SN} anomaly, no Ce/Ce^*_{SN} anomaly; Field IIIa = positive Ce/Ce^*_{SN} anomaly; Field IIIb = negative Ce/Ce^*_{SN} anomaly. Diagrams showing: (b) La/La^*_{SN} versus Ce/Ce^*_{SN} anomalies; (c) Y/Ho ratio compared with Eu/Eu^*_{SN} anomaly; (d) ∑REE confronted with Eu/Eu^*_{SN} anomaly; (e) Eu/Eu^*_{SN} versus Ce/Ce^*_{SN} anomalies.

https://doi.org/10.1180/mgm.2025.10124 Published online by Cambridge University Press

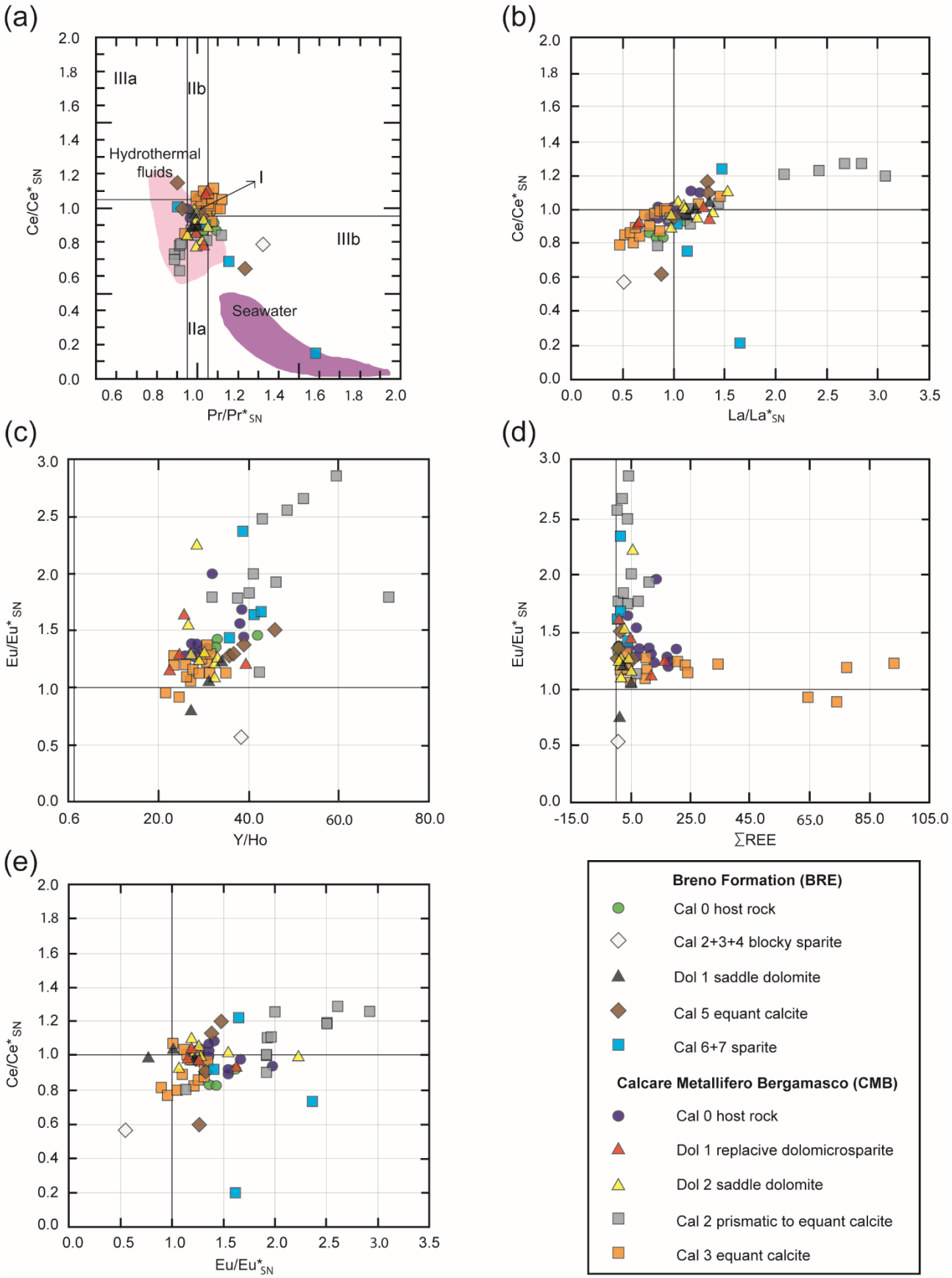

Figure 16. Total subsidence curves for the Paleozoic basement (black), base of the BRE (blue) and top of the

https://doi.org/10.1180/mgm.2025.10124 Published online by Cambridge University Press

CMB (green) in the Brembana Valley sector from the Permian to the Toarcian, modified after Berra and Carminati (2010) according to the new ages of the Geological Time Scale 12/2024. The orange line denotes the moment in which both the BRE and CMB were at burial depths of 300 m, while the green dotted line points to 221.6 (226.9 - 5.3) Ma according to the radiometric ages obtained by Giorno et al. (2022) for the post-ore calcite. VUC = Monte Cabianca volcaniclastic rocks; FPZ = Pizzo del Diavolo Formation; VER = Verrucano Lombardo; SRV = Servino Formation; BOV = Carniola di Bovegno; ANG = Angolo Limestone; CAM = Camorelli Limestone; PRZ = Prezzo Limestone; ESI = Esino Limestone; KLR = Calcare Rosso; BRE = Breno Formation; CMB = Calcare Metallifero Bergamasco; SAB = Val Sabbia Sandstones; GOR = Gorno Formation; SGB = San Giovanni Bianco Formation; CSO = Castro Sebino Formation; DPR = Dolomia Principale; ARS = Riva di Solto Shales; ZUU = Zu Limestone; MAL = Malanotte Formation; ALZ = Albenza Formation; SED = Sedrina Limestone; MOT = Moltrasio Limestone; DOM = Domaro Limestone; SOG = Sogno Formation; U = Unconformity.

https://doi.org/10.1180/mgm.2025.10124 Published online by Cambridge University Press

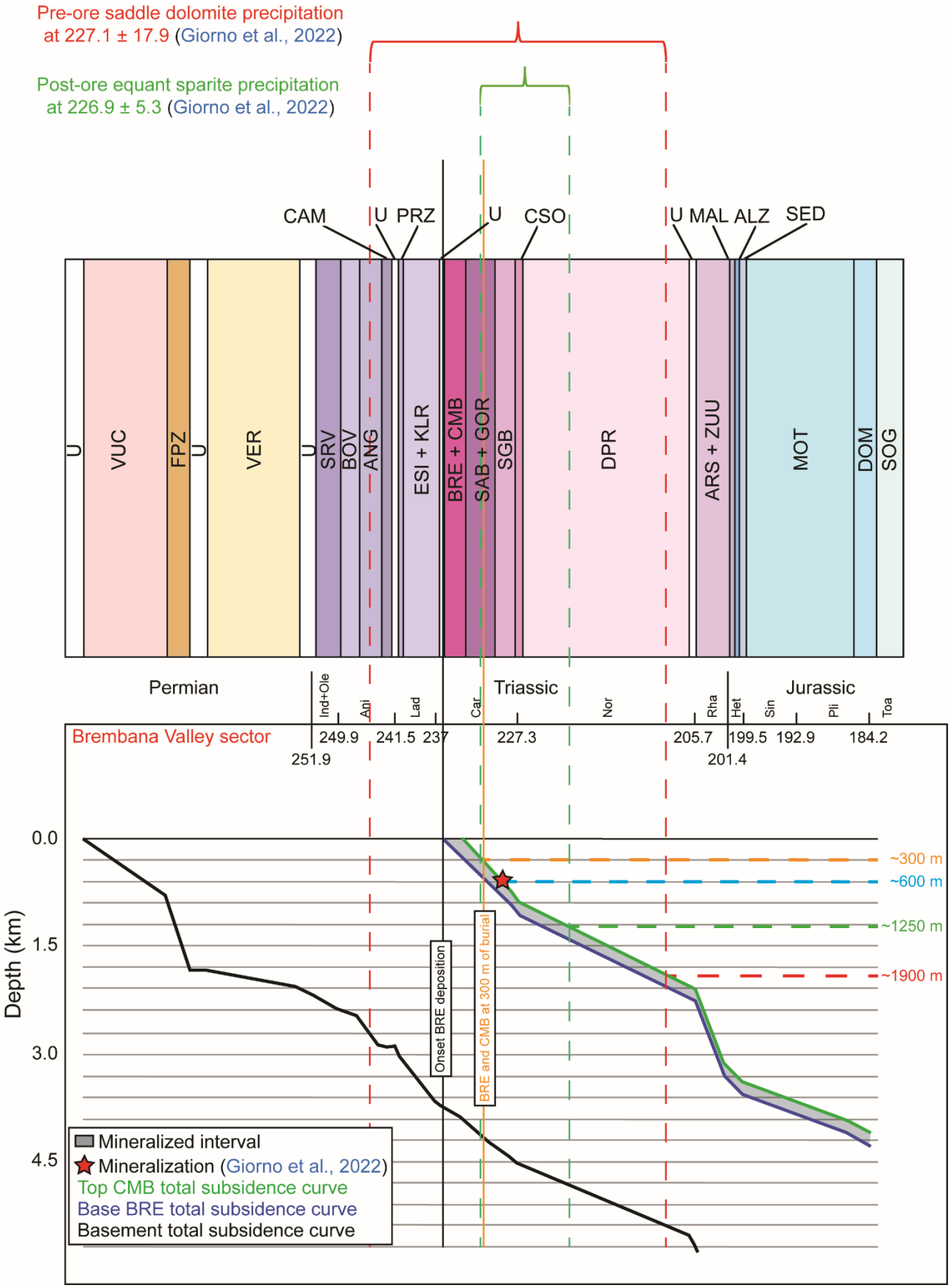

https://doi.org/10.1180/mgm.2025.10124 Published online by Cambridge University Press

Authors	Formation (Age)	Locality	Analytical techniques	Carbonate phases	Mineralisation	Genesis and timing of mineralisation	Supporting evidence
Vachè (1966)	Esino Limestone (Anisian-Ladinian), BRE and CMB (lower Carnian), Gorno Fm. (Carnian).	Gorno/Monte Trevasco	Field work, petrography.	-	Dominant sphalerite, galena and pyrite.	Syngenetic mineralisation due to submarine exhalations strictly related to late Ladinian-Carnian volcanism.	Ores concentrated close to volcanic tuffs from late Ladinian-Carnian explosive volcanic events.
Omenetto (1966)	Esino Limestone (Anisian-Ladinian), BRE and CMB (lower Carnian), Gorno Fm. (Carnian).	Oltre il Colle	Field work, petrography,	-	Sphalerite, galena,fluorite, tetraedrite, tennantite, bournonite, As-bournonite, jamesonite, boulangerite, pyrite, marcasite, chalcopyrite, covellite, chalcocite.	Double phase hydrothermal mineralisation: (1) synsedimentary for upper Ladinian stratiform mineralisation; (2) epigenetic for columnar and inside fault mineralisation during Alpine orogenesis.	Synsedimentary mineralisation: (1) stratiform mineralisation interbedded with bituminous shales; (2) epigenetic mineralisation: mineralised faults and “column” cross-cut cemented carbonates.
Assereto et al. (1977)	Esino Limestone (Anisian-Ladinian), BRE and CMB (lower Carnian).	Paglio Pignolino/Dossena	Field work, petrography.	-	Dominant fluorite, subordinated sphalerite, galena and baryte.	Early diagenetic mineralisation.	Filling dissolution cavities (subconcordant and/or discordant to bedding) and stratiform mineralisation. Siliciclastic supply and leaching of elements from volcaniclastic rocks.
Omenetto and Vailati (1977)	Esino Limestone (Anisian-Ladinian), BRE and CMB (lower Carnian).	Val Vedra	Petrography, geochemistry.	-	Sphalerite, galena and pyrite, subordinate baryte and fluorite.	Early diagenetic mineralisation. The mineralising process ended before the Middle Triassic.	Ore crossed by porphyric dykes, suggesting that the mineralisation was not related to volcanic activity, metals supplied by continental siliciclastic deposits.
Rodeghiero et al. (1986)	BRE and CMB (lower Carnian).	Ballabio-Mandello del Lario (Pian dei Resinelli).	Petrography, CL, XRD.	Post-mineralisation blocky calcite cement bright orange in CL.	Dominant sphalerite and galena, subordinate pyrite, baryte and fluorite.	Alpine-Type syngenetic to epigenetic mineralisation, with ore mineral recrystallisation in deep burial (3 km depth) by hydrothermal fluids during Early-Middle Jurassic rifting.	Stylolites crossed by dissolution linked to Early-Middle Jurassic rifting at 3 km depth. Metals derived from coeval Ladinian-Carnian volcanic rocks or from basement leached by hydrothermal fluids.

https://doi.org/10.1180/mgm.2025.10124 Published online by Cambridge University Press

Mondillo et al. (2020)	BRE and CMB (lower Carnian).	Val Vedra/Monte Trevasco.	Petrography, CL, C-O isotopes, XRD, XRF.	Replacive dolomicrite on limestone host rock, saddle dolomite cement, several blocky sparite cement pre- and post-mineralisation following saddle dolomite.	Dominant sphalerite and galena, subordinate pyrite, chalcopyrite.	Alpine-Type mineralisation in deep burial settings by hydrothermal fluids through volcaniclastic deposits, with precipitation during Early-Middle Jurassic extensional tectonics.	Low $\delta^{18}O$ and $\delta^{13}C$ of calcite and dolomite cements; high Cu, Sb, As, Ag, Mo, Ge, and Cd concentrations in the sulphides in agreement with hydrothermal fluid circulation through volcaniclastic deposits.
Giorno et al. (2022)	BRE and CMB (lower Carnian).	Monte Arera, Gorno/Monte Trevasco, Paglio Pignolino/Dossena.	Petrography, CL, LA-ICP-MS, U-Pb radiometric dating, FIs.	Replacive dolomicrite Dol 1 on limestone (bright red luminescent), Cal 1 sparry calcite in fenestral pores (non-luminescent, dull brown, zoned), Dol 2 vein filling dolosparite and saddle dolomite cement (dull red to non-luminescent), Dol 3 vein filling saddle dolomite and overgrowth on Dol 2 (dull brown), Cal 2 blocky sparite filling veins, pores and overgrowth on previous carbonate phases (bright orange).	Sphalerite, galena, fluorite and baryte.	Alpine-Type mineralisation in shallow burial settings (tens to few hundred meters) by hydrothermal fluids related to Triassic magmatism and prior to the Early Jurassic rifting phase.	U-Pb radiometric dating of carbonate phases before and after sulphide precipitation (Dol 2 saddle dolomite cement: 229.9 ± 11.2 Ma - 227.1 ± 17.9 Ma; Cal 2 blocky calcite cement: 232.2 ± 5.2 Ma - 226.9 ± 5.3 Ma corresponding to late Carnian).
Zeeh et al. (1998)	Wetterstein Formation (Ladinian-Carnian), Raibl Group (Carnian).	Drau Range (South Austria-North-East Slovenia).	Petrography, CL, S stable isotope, FIs.	The first and the second sphalerite generations are preceded and followed by clear saddle dolomite (CSD) and followed by zoned blocky sparite cement (ZBC).	Sphalerite, galena, fluorite, barite, anhydrite (Late Triassic-Early Jurassic and Cretaceous-Miocene).	Near surface, shallow to deep burial diagenesis. Alpine-type MVT mineralisation in deep burial settings.	Th from FIs of carbonate cements (CSD: 122-147°C; CLOSD: 175-194°C; ZBC: 200-280°C), sphalerite (126-159°C) and fluorite (1: 200-225°C; 2: 150-175°C; 3: 124-165°C), O stable isotopes CSD (6 - 10‰ V-SMOW). CSD is found in fissures of Anisian to Lower Jurassic rocks.
Kuhlemann et al. (2001)	Wetterstein Formation (Ladinian-Carnian).	Drau Range (Austria), Mezica (Slovenia), Bleiberg (Austria).	S isotope data (Zeeh et al., 1998).	The first and the second sphalerite generations are preceded and followed by CSD and followed by ZBC.	Sphalerite, galena, fluorite, baryte, anhydrite.	Near surface, shallow to deep burial diagenesis. MVT mineralisation in deep burial settings.	S isotope data of sphalerite (-28.64 - 2.79‰).
Palinkas et al. (2008)	Silurian-Triassic (?).	Sv. Jakob, Medvednica Mt. (Croatia).	Petrography, FIs, S isotope data, U-Pb radiometric dating.	-	Galena, sphalerite, pyrite, anglesite, cerussite.	Influence of warm basinal brines expelled during Middle Triassic advanced rifting mixed with less saline, colder meteoric fluids.	FIs on quartz (NaCl-CaCl2-H2O composition, 6-19 wt% NaCl eq., Th (80-230°C), δ34S (7 - 10‰), U-Pb radiometric age on sulphur (490 Ma corresponding to Cambrian).
Brusca et	Dolomia del	Salafossa,	-	-	Sphalerite, galena,	Enrichment of clay in base	Literature research.

https://doi.org/10.1180/mgm.2025.10124 Published online by Cambridge University Press

al. (2010)	Serla (Anisian), Dolomia Cassiana (Upper Ladinian-Middle Carnian).	Auronzo, Monte Rite, Cima Rolle (Italy).			pyrite, marcasite, baryte (Triassic-Cenozoic?).	metals, increase in T with progressive burial, OM provided by sediments and S provided by evaporite lenses. Syngenetic to epigenetic mineralisation related to the Alpine orogenesis.	
Henjes-Kunst et al. (2017)	Wetterstein Formation (Ladinian-Carnian).	Bleiberg (Austria).	Petrography, EPMA chemistry, S isotope.	Several generations of mineralisation intergrown with calcite and dolomite cements and with baryte, galena, pyrite and fluorite	Sphalerite, galena, pyrite, baryte, fluorite.	Alpine-type MVT mineralisation divided in early (Norian) and late stage (Rhaetian-Hettangian).	Maximum burial temperatures of the basin (110°C), Rb-Sr radiometric dating on sphalerite obtained by Melcher et al. (2010) of 201.2 ± 1.6 Ma and 225.2 ± 2.1 Ma (corresponding to Rhaetian/Hettangian and early Norian, respectively).

Table 1. Table summarising published literature on the genesis of the mineralisation in the Alps and the diagenesis of carbonate host rocks: CL = cathodoluminescence; XRD = X-ray diffraction; XRF = X-ray fluorescence; LA-ICP-MS = laser ablation-inductively coupled plasma-mass spectrometry; FIs = fluid inclusions; EPMA = electron microprobe; Th = homogenization temperature; CSD = clear saddle dolomite; ZBC = zoned blocky sparite; CLOSD = cloudy saddle dolomite; OM = organic matter; T = temperature. Syngenetic or synsedimentary = during the deposition of the host rock; epigenetic = after lithification of the host rock. BRE = Breno Formation; CMB = Calcare Metallifero Bergamasco. Lombardy Basin localities are reported in Fig. 1D.

https://doi.org/10.1180/mgm.2025.10124 Published online by Cambridge University Press

Breno Formation				
Phase	**Features**	**Occurrence (Fig.)**	**Sizes**	**CL (Fig.)**
Cal 1	Limpid blocky sparite cement	Primary voids and mouldic porosity after former aragonitic mollusc shells (Fig. 3a-d)	70-500 µm	NL (Fig. 3b)
Cal 2	Limpid blocky sparite cement	Millimetre-size vugs (Fig. 3e)	100-800 µm	Zoned: NL cores and BL rims (Fig. 3f)
Cal 3	Limpid blocky sparite cement	Millimetre-size vugs (Fig. 3e)	300-900 µm	DL (Fig. 3f)
Cal 4	Limpid blocky sparite cement	Millimetre-size vugs (Fig. 3e)	50-300 µm	BL or zoned BL-DL (Fig. 3f)
Dol 1	Cloudy brownish saddle dolomite cement	Fractures cross-cutting Cal 0 to Cal 4 (Figs 3g,h, 4a,c,e,g)	100 µm - 2.5 mm	DL (Fig. 4b,f,h) or zoned with DL cores and BL-DL rims (Fig. 4d)
Cal 5	Limpid equant calcite cement	Overlying Dol 1 (Figs 3g, 4a) and filling intercrystal spaces between Dol 1 (Fig. 4c,e)	200 µm - 1 mm	Zoned with NL cores and BL rims (Fig. 4b) or NL to DL (Fig. 4d,e)
Cal 6	Cloudy sparite to microsparite cement	Fractures cutting through Cal 0 to Cal 5 (Figs 3a,b, 4a,c,g, 5c), partially replacing Dol 1 (Fig. 4b,f), locally resulting in breccia textures (Fig. 5a)	<50 µm – 2 cm	BL (Figs 3b, 4b,d,f,h, 5d)
Sphalerite, galena and fluorite	-	Intercrystal porosity between Cal 6 (Fig. 5b,c)	150 µm - 3 mm	-
Cal 7	Cloudy sparite cement	Fractures cross-cutting Dol 1 (Figs 4e,g, 5f), Cal 6 (Figs 4e,g, 5b), overlying fluorite crystals (Fig. 5e) and brecciating Cal 0 in mm to cm size angular fragments (Fig. 5g,h)	100-800 µm	BL, less than Cal 6 (Fig. 4f,h)
Quartz	Euhedral hexagonal bipyramidal quartz	Fractures associated with Cal 7 (Figs 4e-h, 5b, e,f,g,h)	100 µm – 2 mm	-
Stylolite 1	-	Cutting through Cal 0 to quartz (Figs 3d, 5h)	-	-

Table 2. Table detailing the petrographic features of the identified diagenetic phases of the Breno Formation. NL = non-luminescent; BL = bright luminescent; DL = dull luminescent.

https://doi.org/10.1180/mgm.2025.10124 Published online by Cambridge University Press

Calcare Metallifero Bergamasco

Phase	Features	Occurrence (Fig.)	Sizes	CL (Fig.)
Cal 1	Limpid blocky microsparite-sparite cement	Interparticle, vug and mouldic porosity (Fig. 7a-c)	20-150 µm	NL (Fig. 7d)
Stylolite 1	-	Cutting through Cal 0 and Cal 1	-	-
Dol 1	Fabric destructive anhedral dolomicrosparite	Replacing Cal 0 (Fig. 7e)	20-50 µm	PL (Fig. 7f)
Silicification	Microquartz and fibrous chalcedony	Replacing Cal 0 (Figs 7g,h, 8a,b)	<20-50 µm	NL (Figs 8b, S2b)
Dol 2	Cloudy saddle dolomite cement	Fractures (Figs 7h, 8a,e, S2c) or sparse in the silicified portions (Fig. S2a)	70 µm - 1 mm	Zoned with DL to NL cores and BL rims (Fig. 8d,S2b,d)
Cal 2	Limpid prismatic to equant calcite cement	Fractures (Figs 7h, 8a, 9a-d) and intercrystal voids between Dol 2 (Fig. 8c)	80 µm - 2.5 mm	BL (Figs 8b,d,h, 9h)
Stylolite 2	-	Cutting through Cal 0 and silicification and cross-cut by fractures filled by Dol 2 and Cal 2 (Fig. 9a-c)	-	-
Sphalerite, galena and fluorite	Euhedral	Fractures and secondary voids after Cal 2 (Figs 9b,d-f, S2e-h)	Sp: 100 µm - 2.5 mm**.** Gn: 80 µm - 1.5 mm**.** Fl: 100 µm - 1.5 mm	-
Cal 3	Equant sparite cement	Fractures cross-cutting all previous phases (Figs 7c,e, 8e,f, 9e-g, S2f) partially replacing Dol 2 (Figs 8c,d,g,h, S2c,d), Cal 2 (Fig. 8g,h), Cal 0 (Fig. 7c,d) and overlying fluorite (Fig. S2g,h)	<20-600 µm	BL (Figs 7d,f, 8d,h, 9h, S2d,h)
Quartz mosaic	Equant cement	Filling the intercrystal porosity between sphalerite, galena and fluorite (Fig. S2e)	80 µm - 2 mm	-
Stylolite 3	-	Cutting through fluorite (Fig. 9e)	-	-

Table 3. Table detailing the petrographic features of the identified diagenetic phases of the Calcare Metallifero Bergamasco. NL = non-luminescent; PL = patchy luminescent; BL = bright luminescent; DL = dull luminescent; Sp = sphalerite; Gn = galena; Fl = fluorite.

https://doi.org/10.1180/mgm.2025.10124 Published online by Cambridge University Press

	Breno Formation											
	Fe	Mn	Sr	Si	Zr	Sc	Th	Ti	Zn	Pb	∑REE	Mn/Fe
Cal 0 (DL) (*N* = 4)												
Mean	275	454	135	1010	0.225	0.168	0.049	7.70	18.6	18.4	3.05	2.44
SD	159	250	51.7	747	0.194	0.058	0.013	9.44	14.5	21.1	1.86	0.01
Max	289	702	186	1925	0.469	0.220	0.066	21.1	39.7	40.9	4.70	2.44
Min	261	218	87.5	272	0.025	0.089	0.037	0.310	7.58	0.311	1.33	2.43
Cal 2 (NL cores-BL rims) + Cal 3 (DL) + Cal 4 (BL) (*N* = 1)												
Mean	n.m.	193	183	419	n.d.	n.d.	n.d.	0.184	0.085	0.073	0.207	-
Dol 1 (DL cores-BL rims) (*N* = 3)												
Mean	n.m.	310	49.4	490	n.d.	0.05	0.01	1.43	1.83	0.042	3.10	-
SD	-	117	18.7	26.9	n.d.	0.03	0.01	0.794	1.20	0.01	1.96	-
Max	-	431	70.0	518	n.d.	0.05	0.02	2.35	3.17	0.053	5.24	-
Min	-	197	33.4	464	n.d.	n.d.	0.01	0.96	0.846	0.035	1.33	-
Cal 5 (NL cores-BL rims-NL-DL overgrowth) (*N* = 4)												
Mean	n.m.	222	300	538	0.004	0.04	0.01	0.179	0.285	0.084	1.75	-
SD	-	231	163	31.9	0.004	0.02	0.02	0.09	0.208	0.117	2.45	-
Max	-	483	426	577	0.01	0.04	0.04	0.179	0.568	0.258	5.44	-
Min	-	24.4	76.5	505	n.d.	n.d.	n.d.	n.d.	0.086	0.01	0.425	-
Cal 6 (BL) + Cal 7 (BL) (*N* = 4)												
Mean	182	435	148	380	n.d.	0.03	0.01	n.d.	0.444	0.288	1.51	2.42
SD	8.56	483	61.0	66.4	n.d.	0.02	0.01	-	0.091	0.186	1.37	2.69
Max	194	925	237	479	n.d.	0.03	0.01	n.d.	0.504	0.518	3.44	5.07
Min	176	4.79	98.1	342	n.d.	n.d.	n.d.	n.d.	0.311	0.075	0.199	0.027

Table 4A. Fe, Mn, Sr, Si, Zr, Sc, Th, Ti, Zn, Pb, total amount of Rare Earth Element (except Y) concentrations in ppm and Mn/Fe ratios in the investigated carbonate phases of the Breno Formation. BL = bright luminescent; DL = dull luminescent; NL = non-luminescent; n.m. = not measured; n.d. = not detected. Values < 0.01 are here considered as n.d.

https://doi.org/10.1180/mgm.2025.10124 Published online by Cambridge University Press

	Breno Formation										
	Li	B	V	Co	Ni	Cu	Ba	U	As	Sb	Rb
Cal 0 (DL) (*N* = 4)											
Mean	0.413	1.87	6.02	0.095	0.482	0.556	3.25	1.22	0.329	0.229	0.585
SD	0.364	1.12	1.44	0.054	0.175	0.339	2.19	0.722	0.360	0.091	0.496
Max	0.841	3.32	7.27	0.173	0.738	1.03	6.00	1.93	0.858	0.325	1.25
Min	0.038	0.870	4.34	0.057	0.366	0.222	1.40	0.535	0.086	0.106	0.046
Cal 2 (NL cores-BL rims) + Cal 3 (DL) + Cal 4 (BL) (*N* = 1)											
Mean	0.020	1.03	n.d.	0.154	0.432	0.080	0.035	n.d.	n.d.	n.d.	n.d.
Dol 1 (DL cores-BL rims) (*N* = 3)											
Mean	0.408	2.31	8.20	0.046	0.335	0.333	0.773	0.019	0.046	0.016	0.050
SD	0.091	0.095	6.48	0.010	0.108	0.055	0.237	0.014	0.015	0.010	0.014
Max	0.497	2.40	15.6	0.053	0.459	0.394	0.997	0.030	0.061	0.025	0.061
Min	0.315	2.21	3.55	0.035	0.261	0.286	0.524	n.d.	0.034	0.010	0.034
Cal 5 (NL cores-BL rims-NL-DL overgrowth) (*N* = 4)											
Mean	0.149	1.53	0.202	0.079	0.369	0.148	0.713	0.003	0.035	0.013	0.008
SD	0.064	0.121	0.176	0.01	0.058	0.056	0.603	0.001	0.020	0.001	0.004
Max	0.243	1.66	0.433	0.085	0.424	0.227	1.28	0.01	0.036	0.015	0.010
Min	0.103	1.41	0.044	0.074	0.308	0.094	0.189	0.002	n.d.	n.d.	n.d.
Cal 6 (BL) + Cal 7 (BL) (*N* = 4)											
Mean	0.077	1.42	1.44	0.110	0.393	0.159	0.121	0.123	0.072	n.d.	0.010
SD	0.059	0.082	1.65	0.011	0.041	0.028	0.065	0.166	0.042	-	0.010
Max	0.155	1.52	3.04	0.121	0.428	0.194	0.211	0.355	0.082	-	0.012
Min	0.024	1.32	0.014	0.097	0.346	0.127	0.065	n.d.	n.d.	-	n.d.

Table 4B. Li, B, V, Co, Ni, Cu, Ba, U, As, Sb, Rb concentrations in ppm in the investigated carbonate phases of the Breno Formation. BL = bright luminescent; DL = dull luminescent; NL = non-luminescent; n.d. = not detected. Values < 0.01 are here considered as n.d.

https://doi.org/10.1180/mgm.2025.10124 Published online by Cambridge University Press

Breno Formation																
	La	Ce	Pr	Nd	Sm	Eu	Gd	Tb	Dy	Y	Ho	Er	Tm	Yb	Lu	Y/Ho
Cal 0 (DL) (*N* = 4)																
Mean	0.630	1.27	0.155	0.568	0.104	0.027	0.098	0.014	0.081	0.537	0.016	0.043	0.010	0.038	0.010	35.0
SD	0.325	0.776	0.099	0.369	0.074	0.019	0.065	0.010	0.053	0.354	0.011	0.025	0.004	0.028	0.004	4.80
Max	0.939	1.97	0.243	0.909	0.171	0.045	0.158	0.022	0.136	0.863	0.026	0.068	0.010	0.068	0.010	42.2
Min	0.312	0.545	0.065	0.228	0.039	0.011	0.038	0.01	0.033	0.215	0.010	0.020	n.d.	0.011	n.d.	31.6
Cal 2 (NL cores-BL rims) + Cal 3 (DL) + Cal 4 (BL) (*N* = 1)																
Mean	0.035	0.063	0.010	0.029	0.010	0.001	0.009	n.d.	0.018	0.157	n.d.	0.012	n.d.	0.011	n.d.	38.5
Dol 1 (DL cores-BL rims) (*N* = 3)																
Mean	0.736	1.26	0.134	0.513	0.095	0.021	0.098	0.016	0.107	0.665	0.021	0.052	0.010	0.036	0.010	30.3
SD	0.498	0.771	0.079	0.300	0.054	0.014	0.072	0.013	0.089	0.575	0.018	0.043	0.010	0.035	0.004	2.54
Max	1.28	2.06	0.217	0.831	0.153	0.035	0.180	0.031	0.209	1.33	0.042	0.101	0.013	0.076	0.010	31.9
Min	0.301	0.525	0.060	0.234	0.046	0.007	0.046	0.008	0.052	0.300	0.011	0.025	n.d.	0.012	0.002	27.3
Cal 5 (NL cores-BL rims-NL-DL overgrowth) (*N* = 4)																
Mean	0.372	0.729	0.086	0.332	0.060	0.015	0.053	0.010	0.046	0.312	0.010	0.022	n.d.	0.019	n.d.	39.4
SD	0.526	1.05	0.123	0.471	0.081	0.020	0.071	0.010	0.056	0.370	0.010	0.027	n.d.	0.015	n.d.	4.53
Max	1.16	2.30	0.271	1.04	0.182	0.045	0.159	0.024	0.129	0.857	0.023	0.062	n.d.	0.034	n.d.	46.0
Min	0.094	0.165	0.020	0.094	0.017	0.004	0.013	0.002	0.010	0.063	0.002	0.003	n.d.	n.d.	n.d.	35.9
Cal 6 (BL) + Cal 7 (BL) (*N* = 4)																
Mean	0.321	0.534	0.070	0.281	0.060	0.020	0.066	0.011	0.069	0.503	0.013	0.036	n.d.	0.024	n.d.	39.9
SD	0.251	0.518	0.062	0.246	0.058	0.016	0.067	0.010	0.072	0.463	0.013	0.037	n.d.	0.021	n.d.	2.99
Max	0.665	1.26	0.158	0.629	0.143	0.042	0.164	0.025	0.170	1.16	0.032	0.089	n.d.	0.053	n.d.	42.8
Min	0.077	0.021	0.012	0.051	0.008	0.003	0.009	n.d.	0.010	0.081	n.d.	n.d.	n.d.	n.d.	n.d.	36.1

Table 4C. REEY concentrations in ppm and Y/Ho ratios in the investigated carbonate phases of the BRE. BL = bright luminescent; DL = dull luminescent; NL = non-luminescent; n.d. = not detected. Values < 0.01 are here considered as n.d.

https://doi.org/10.1180/mgm.2025.10124 Published online by Cambridge University Press

Breno Formation

Normalising factor		Nd/Yb_N	Pr/Yb_N	La/Sm_N	Dy/Yb_N	Lawrence et al. (2006) La/La^*_N	Eu/Eu^*_N	Gd/Gd^*_N	Ce/Ce^*_N	Bau and Dulski (1996) Pr/Pr^*_N	Eu/Eu^*_N	Ce/Ce^*_N
	Cal 0 (DL) (*N* = 4)											
$PAAS_{SN}$	**Mean**	1.4	1.5	1.0	1.4	0.9	1.4	1.2	0.9	1.1	1.4	0.9
	SD	0.5	0.5	0.3	0.4	0.1	0.1	0.1	0.0	0.0	0.1	0.1
	Max	2.1	2.2	1.4	2.1	1.1	1.4	1.3	0.9	1.1	1.4	1.0
	Min	1.1	1.1	0.8	1.2	0.8	1.3	1.0	0.8	1.0	1.3	0.9
MuQ_{SN}	**Mean**	1.7	1.8	1.5	1.3	1.0	1.2	1.1	0.9	1.0	1.2	0.9
	SD	0.6	0.6	0.5	0.4	0.2	0.0	0.1	0.0	0.0	0.0	0.1
	Max	2.5	2.6	2.1	1.9	1.2	1.2	1.2	1.0	1.1	1.2	1.0
	Min	1.3	1.4	1.1	1.1	0.8	1.1	1.0	0.9	1.0	1.1	0.9
$C\text{-}1_{CN}$	**Mean**	5.9	8.4	4.5	1.5	0.8	0.9	1.1	0.8	1.1	0.8	0.9
	SD	1.9	2.7	1.3	0.5	0.1	0.0	0.1	0.0	0.0	0.0	0.1
	Max	8.8	12.4	6.2	2.2	1.0	0.9	1.2	0.9	1.1	0.9	1.0
	Min	4.7	6.5	3.2	1.3	0.7	0.8	1.0	0.8	1.0	0.8	0.8
	Cal 2 (NL cores-BL rims) + Cal 3 (DL) + Cal 4 (BL) (*N* = 1)											
	Mean	0.2	0.3	0.5	1.0	0.5	0.5	0.8	0.6	1.3	0.5	0.8
	Mean	0.3	0.3	0.7	1.0	0.6	0.5	0.7	0.6	1.3	0.5	0.8
	Mean	1.0	1.6	2.1	1.1	0.5	0.3	0.8	0.5	1.3	0.3	0.8
	Dol 1 (DL cores-BL rims) (*N* = 3)											
	Mean	1.6	1.6	1.1	2.1	1.2	1.0	1.1	1.0	1.0	1.0	0.9
	SD	0.6	0.7	0.1	0.5	0.1	0.2	0.0	0.0	0.0	0.2	0.0
	Max	2.2	2.2	1.2	2.5	1.4	1.2	1.1	1.1	1.0	1.2	1.0
	Min	0.9	0.9	0.9	1.7	1.1	0.8	1.0	1.0	1.0	0.8	0.9
	Mean	1.9	1.9	1.6	1.9	1.3	0.9	1.0	1.1	1.0	0.9	0.9
	SD	0.8	0.8	0.2	0.4	0.1	0.2	0.0	0.0	0.0	0.2	0.0
	Max	2.6	2.7	1.8	2.3	1.5	1.1	1.0	1.1	1.0	1.1	1.0
	Min	1.1	1.1	1.4	1.5	1.2	0.7	1.0	1.1	0.9	0.7	0.9
	Mean	6.5	8.8	4.6	2.2	1.1	0.6	1.0	1.0	1.0	0.6	0.9
	SD	2.7	3.7	0.6	0.5	0.1	0.2	0.0	0.0	0.0	0.1	0.1
	Max	9.2	12.6	5.3	2.8	1.2	0.8	1.0	1.0	1.0	0.7	0.9
	Min	3.8	5.2	4.1	1.8	1.0	0.5	1.0	0.9	1.0	0.5	0.9
	Cal 5 (NL cores-BL rims-NL-DL overgrowth) (*N* = 4)											
	Mean	1.7	1.7	0.9	1.7	1.1	1.4	1.1	1.0	1.0	1.4	0.9
	SD	1.2	1.2	0.2	1.0	0.2	0.1	0.1	0.3	0.2	0.1	0.2
	Max	2.6	2.6	1.0	2.3	1.3	1.5	1.3	1.2	1.2	1.5	1.1
	Min	n.d.	n.d.	0.7	n.d.	0.9	1.3	1.0	0.6	0.9	1.3	0.6
	Mean	2.0	2.0	1.3	1.6	1.2	1.2	1.0	1.0	1.0	1.2	0.9
	SD	1.4	1.4	0.2	0.9	0.2	0.1	0.1	0.3	0.2	0.1	0.2
	Max	3.0	3.1	1.5	2.1	1.5	1.3	1.2	1.3	1.2	1.3	1.2
	Min	n.d.	n.d.	1.0	n.d.	1.0	1.1	0.9	0.6	0.9	1.1	0.7
	Mean	6.9	9.4	3.7	1.9	1.0	0.9	1.0	0.9	1.0	0.8	0.9

https://doi.org/10.1180/mgm.2025.10124 Published online by Cambridge University Press

SD	4.9	6.7	0.7	1.1	0.2	0.1	0.1	0.3	0.2	0.1	0.2
Max	10.7	14.5	4.5	2.5	1.2	0.9	1.2	1.2	1.3	0.9	1.1
Min	n.d.	n.d.	3.0	n.d.	0.8	0.8	0.9	0.6	0.9	0.8	0.6
Cal 6 (BL) + Cal 7 (BL) (*N* = 4)											
Mean	1.1	1.0	1.0	1.5	1.3	1.8	1.2	0.8	1.2	1.7	0.7
SD	0.3	0.4	0.3	0.4	0.3	0.4	0.3	0.4	0.3	0.4	0.4
Max	1.5	1.5	1.4	1.9	1.7	2.3	1.6	1.2	1.6	2.3	1.0
Min	0.7	0.6	0.7	1.2	1.1	1.4	0.8	0.2	0.9	1.4	0.2
Mean	1.3	1.2	1.4	1.4	1.5	1.5	1.1	0.8	1.2	1.5	0.7
SD	0.4	0.4	0.5	0.3	0.3	0.4	0.3	0.5	0.3	0.4	0.4
Max	1.7	1.8	2.1	1.8	1.8	2.0	1.4	1.3	1.6	2.0	1.0
Min	0.8	0.7	1.0	1.1	1.2	1.2	0.8	0.2	0.9	1.2	0.2
Mean	4.4	5.7	4.2	1.7	1.2	1.1	1.1	0.7	1.3	1.1	0.7
SD	1.3	2.0	1.5	0.4	0.3	0.3	0.3	0.4	0.5	0.2	0.4
Max	6.1	8.3	6.1	2.1	1.5	1.5	1.5	1.2	1.9	1.4	1.0
Min	2.9	3.4	2.9	1.3	0.9	0.9	0.8	0.2	0.9	0.9	0.1

Table 4D. Normalised Nd/Yb, Dy/Yb, Pr/Yb, La/Sm ratios, calculated La, Eu, Gd and Ce geometric anomalies according to Lawrence et al. (2006) and Pr, Eu and Ce anomalies according to Bau and Dulski (1996) of the investigated carbonate phases of the Breno Formation. All the calculated parameters are normalised to Post-Archean Australian Shale (PAAS, McLennan, 1989), Mud from Queensland (MuQ, Kamber et al., 2005) and Carbonaceous chondrites (C-1, Taylor and McLennan, 1981). N = normalised; SN = shale normalised; CN = chondrite normalised; BL = bright luminescent; DL = dull luminescent; NL = non-luminescent.

https://doi.org/10.1180/mgm.2025.10124 Published online by Cambridge University Press

Calcare Metallifero Bergamasco

	Fe	Mn	Sr	Si	Zr	Sc	Th	Ti	Zn	Pb	∑REE	Mn/Fe
Cal 0 (BL) (*N* = 12)												
Mean	270	544	141	4100	0.452	0.515	0.060	13.4	60.6	1.79	11.0	1.85
SD	169	288	37.3	7868	1.19	0.547	0.082	33.2	163	2.73	5.28	1.08
Max	552	1109	178	27728	4.23	1.51	0.307	118	576	9.35	19.9	3.21
Min	189	278	66.7	450	0.041	0.043	0.010	0.179	0.503	0.023	3.67	n.d.
Dol 1 (PL) (*N* = 4)												
Mean	5199	2262	69.7	19207	2.81	1.42	0.389	109	560	3.51	7.25	0.552
SD	3040	851	19.5	24208	3.63	1.61	0.442	124	747	2.40	7.75	0.321
Max	5792	2910	90.9	51330	7.73	3.10	0.836	241	1613	5.71	16.1	0.601
Min	4605	1051	51.6	407	0.066	0.032	0.010	2.99	27.3	1.36	0.601	n.d.
Dol 2 (DL cores-BL rims) (*N* = 8)												
Mean	n.m.	1085	96.0	387	0.016	0.130	0.022	1.98	163	0.426	2.97	-
SD	-	916	32	80.9	0.024	0.081	0.022	0.514	94.2	0.589	1.44	-
Max	-	2513	167	514	0.073	0.215	0.066	2.58	295	1.72	4.97	-
Min	-	176	73.8	297	n.d.	n.d.	n.d.	1.39	47.7	0.072	1.37	-
Cal 2 (BL) (*N* = 11)												
Mean	188	1360	165	396	n.d.	0.127	0.031	0.209	3.76	0.041	3.76	8.32
SD	97.4	405	73.7	72.9	n.d.	0.133	0.023	0.112	5.16	0.053	3.04	2.16
Max	193	2194	328	581	0.01	0.433	0.071	0.280	14.0	0.185	11.0	11.8
Min	183	730	77.1	304	n.d.	n.d.	n.d.	n.d.	n.d.	n.d.	0.157	n.d.
Cal 3 (BL) (n = 21)												
Mean	233	801	105	426	n.d.	1.05	0.050	0.270	1.30	0.039	23.7	4.39
SD	141	316	33.7	51.0	n.d.	1.49	0.057	0.059	2.95	0.041	28.2	2.03
Max	521	1498	176	520	0.01	5.62	0.207	0.270	13.1	0.126	92.9	8.08
Min	173	376	55.2	350	n.d.	n.d.	n.d.	n.d.	n.d.	n.d.	1.22	n.d.

Table 5A. Fe, Mn, Sr, Si, Zr, Sc, Th, Ti, Zn, Pb, total amount of Rare Earth Element (except Y) concentrations in ppm and Mn/Fe ratios in the investigated carbonate phases of the CMB. BL = bright luminescent; DL = dull luminescent; NL = non-luminescent; PL = patchy luminescent; n.m. = not measured; n.d. = not detected. Values < 0.01 are here considered as n.d.

https://doi.org/10.1180/mgm.2025.10124 Published online by Cambridge University Press

Calcare Metallifero Bergamasco

	Li	B	V	Co	Ni	Cu	Ba	U	As	Sb	Rb
Cal 0 (BL) (*N* = 12)											
Mean	1.87	3.07	3.22	0.148	0.721	1.19	2.73	3.31	7.62	2.78	2.05
SD	3.08	5.62	6.30	0.143	0.609	2.61	2.29	3.49	13.5	4.22	6.15
Max	11.1	20.9	22.9	0.560	2.14	9.37	9.19	10.1	39.7	12.1	21.5
Min	0.084	0.850	0.301	n.d.	0.361	0.176	0.918	0.059	0.189	0.030	0.010
Dol 1 (PL) (*N* = 4)											
Mean	10.3	19.0	19.3	0.513	4.03	5.18	6.55	3.70	9.68	5.22	18.6
SD	12.1	21.5	22.9	0.517	4.84	6.29	5.84	3.71	4.99	4.56	23.7
Max	26.3	47.5	49.5	1.09	10.7	13.9	14.2	7.97	16.0	11.0	49.7
Min	0.919	2.23	1.51	0.069	0.366	0.481	1.89	0.585	3.75	0.561	0.168
Dol 2 (DL cores-BL rims) (*N* = 8)											
Mean	0.697	2.21	4.58	0.061	0.477	0.377	1.79	0.144	1.87	2.38	0.082
SD	0.145	0.728	2.05	0.024	0.167	0.206	0.873	0.131	3.32	5.14	0.037
Max	0.915	3.41	7.14	0.102	0.805	0.861	3.15	0.450	9.79	15.0	0.163
Min	0.447	1.28	1.73	0.030	0.308	0.242	0.789	0.062	0.064	0.054	0.054
Cal 2 (BL) (*N* = 11)											
Mean	0.145	1.33	2.08	0.101	0.384	0.204	0.438	0.365	0.208	0.059	0.016
SD	0.095	0.357	1.39	0.035	0.026	0.128	0.797	0.364	0.160	0.057	0.010
Max	0.286	1.67	3.80	0.120	0.431	0.464	2.71	0.920	0.519	0.188	0.031
Min	n.d.	0.830	n.d.	n.d.	0.341	n.d.	n.d.	0.010	n.d.	n.d.	n.d.
Cal 3 (BL) (*N* = 21)											
Mean	0.093	1.73	1.23	0.103	0.380	0.200	0.227	0.094	0.066	0.033	0.010
SD	0.072	0.725	1.69	0.023	0.038	0.144	0.247	0.108	0.047	0.019	0.010
Max	0.283	3.32	5.77	0.136	0.490	0.699	0.990	0.408	0.179	0.055	0.013
Min	n.d.	0.800	0.072	0.064	0.318	0.072	0.020	n.d.	n.d.	n.d.	n.d.

Table 5B. Li, B, V, Co, Ni, Cu, Ba, U, As, Sb, Rb concentrations in ppm in the investigated carbonate phases of the CMB. BL = bright luminescent; DL = dull luminescent; NL = non-luminescent; PL = patchy luminescent; n.d. = not detected. Values < 0.01 are here considered as n.d.

https://doi.org/10.1180/mgm.2025.10124 Published online by Cambridge University Press

Calcare Metallifero Bergamasco

	La	Ce	Pr	Nd	Sm	Eu	Gd	Tb	Dy	Y	Ho	Er	Tm	Yb	Lu	Y/Ho
Cal 0 (BL) (*N* = 12)																
Mean	2.35	4.83	0.538	2.03	0.363	0.089	0.297	0.038	0.209	1.17	0.039	0.102	0.014	0.098	0.015	31.4
SD	1.06	2.36	0.271	1.05	0.176	0.040	0.142	0.017	0.091	0.453	0.017	0.046	0.010	0.050	0.007	4.66
Max	4.24	8.79	0.965	3.70	0.640	0.152	0.555	0.066	0.361	1.79	0.065	0.163	0.024	0.165	0.025	39.2
Min	0.898	1.56	0.171	0.639	0.106	0.031	0.109	0.011	0.068	0.500	0.013	0.028	0.010	0.019	n.d.	26.3
Dol 1 (PL) (*N* = 4)																
Mean	1.24	3.33	0.399	1.50	0.267	0.053	0.167	0.022	0.117	0.549	0.022	0.057	0.010	0.069	0.010	28.3
SD	1.25	3.62	0.436	1.64	0.284	0.055	0.178	0.022	0.113	0.494	0.021	0.053	0.010	0.064	0.010	7.56
Max	2.70	7.47	0.901	3.41	0.574	0.116	0.348	0.045	0.237	1.05	0.042	0.111	0.017	0.131	0.021	39.5
Min	0.150	0.225	0.028	0.112	0.019	0.006	0.014	n.d.	0.018	0.103	n.d.	0.010	n.d.	0.011	n.d.	22.9
Dol 2 (DL cores-BL rims) (*N* = 8)																
Mean	0.766	1.26	0.130	0.454	0.080	0.023	0.078	0.011	0.076	0.458	0.016	0.038	0.010	0.026	0.003	30.1
SD	0.330	0.629	0.068	0.240	0.042	0.016	0.037	0.006	0.044	0.242	0.010	0.021	0.003	0.016	0.002	2.53
Max	1.24	2.17	0.226	0.815	0.144	0.056	0.132	0.020	0.148	0.874	0.030	0.072	0.010	0.047	0.005	33.2
Min	0.409	0.568	0.054	0.193	0.034	0.010	0.039	n.d.	0.028	0.196	0.010	0.016	n.d.	0.010	n.d.	26.9
Cal 2 (BL) (*N* = 11)																
Mean	0.952	1.40	0.155	0.626	0.122	0.049	0.159	0.021	0.130	1.24	0.025	0.064	0.010	0.042	0.005	48.9
SD	0.705	1.14	0.127	0.512	0.111	0.049	0.173	0.025	0.149	1.42	0.029	0.072	0.008	0.039	0.005	11.8
Max	2.39	3.92	0.447	1.86	0.413	0.178	0.633	0.090	0.537	4.91	0.106	0.262	0.029	0.139	0.019	71.3
Min	0.041	0.040	0.010	0.021	n.d.	n.d.	0.010	n.d.	0.008	0.124	n.d.	n.d.	n.d.	n.d.	n.d.	32.0
Cal 3 (BL) (*N* = 21)																
Mean	4.00	10.6	1.31	5.19	0.890	0.181	0.599	0.073	0.388	1.90	0.068	0.175	0.025	0.182	0.028	29.0
SD	4.78	13.2	1.63	6.48	1.01	0.192	0.549	0.061	0.301	1.39	0.050	0.134	0.020	0.156	0.025	3.42
Max	14.8	43.8	5.39	21.6	3.08	0.655	1.84	0.210	1.18	6.12	0.205	0.514	0.067	0.527	0.083	35.1
Min	0.166	0.444	0.061	0.229	0.069	0.020	0.057	0.010	0.032	0.206	0.010	0.014	n.d.	0.013	n.d.	21.8

Table 5C. REEY concentrations in ppm and Y/Ho ratios in the investigated carbonate phases of the CMB. BL = bright luminescent; DL = dull luminescent; NL = non-luminescent; PL = patchy luminescent; n.d. = not detected. Values < 0.01 are here considered as n.d.

https://doi.org/10.1180/mgm.2025.10124 Published online by Cambridge University Press

Calcare Metallifero Bergamasco

Normalising factor		Nd/Yb_N	Pr/Yb_N	La/Sm_N	Dy/Yb_N	Lawrence et al. (2006) La/La^*_N	Lawrence et al. (2006) Eu/Eu^*_N	Lawrence et al. (2006) Gd/Gd^*_N	Lawrence et al. (2006) Ce/Ce^*_N	Bau and Dulski (1996) Pr/Pr^*_N	Bau and Dulski (1996) Eu/Eu^*_N	Bau and Dulski (1996) Ce/Ce^*_N
	Cal 0 (BL) (*N* = 12)											
$PAAS_{SN}$	**Mean**	1.8	1.9	1.0	1.4	1.0	1.4	1.2	1.0	1.0	1.4	1.0
	SD	0.4	0.4	0.1	0.3	0.1	0.2	0.1	0.1	0.0	0.2	0.1
	Max	2.8	2.9	1.2	2.2	1.3	2.0	1.5	1.1	1.0	2.0	1.1
	Min	1.3	1.3	0.8	1.0	0.8	1.2	1.0	0.9	0.9	1.2	0.9
MuQ_{SN}	**Mean**	2.2	2.2	1.4	1.3	1.1	1.2	1.1	1.0	1.0	1.2	1.0
	SD	0.5	0.5	0.2	0.3	0.2	0.2	0.1	0.1	0.0	0.2	0.1
	Max	3.3	3.5	1.8	2.0	1.4	1.7	1.4	1.2	1.0	1.7	1.1
	Min	1.6	1.6	1.1	0.9	0.8	1.1	1.0	1.0	0.9	1.0	0.9
$C\text{-}1_{CN}$	**Mean**	7.6	10.6	4.2	1.5	0.9	0.9	1.1	0.9	1.0	0.8	1.0
	SD	1.7	2.5	0.6	0.4	0.1	0.1	0.1	0.1	0.0	0.1	0.1
	Max	11.7	16.3	5.3	2.3	1.1	1.2	1.4	1.1	1.0	1.2	1.1
	Min	5.5	8.1	3.3	1.1	0.7	0.8	1.0	0.9	0.9	0.7	0.9
	Dol 1 (PL) (*N* = 4)											
	Mean	1.4	1.4	0.9	1.0	1.0	1.3	0.9	0.9	1.0	1.3	1.0
	SD	0.7	0.7	0.3	0.1	0.4	0.2	0.3	0.0	0.0	0.2	0.2
	Max	2.2	2.2	1.1	1.1	1.3	1.6	2.1	1.0	1.1	1.6	1.1
	Min	0.7	0.8	0.6	0.9	0.6	1.1	0.5	0.9	1.0	1.1	0.8
	Mean	1.6	1.7	1.3	0.9	1.1	1.1	0.9	1.0	1.0	1.1	1.0
	SD	0.8	0.8	0.4	0.1	0.4	0.2	0.2	0.0	0.0	0.2	0.2
	Max	2.6	2.6	1.6	1.0	1.5	1.4	1.0	1.1	1.0	1.4	1.1
	Min	0.9	0.9	0.9	0.8	0.7	1.0	0.5	1.0	1.0	0.9	0.8
	Mean	5.7	7.8	3.8	1.1	0.9	0.8	0.9	0.9	1.0	0.8	1.0
	SD	2.8	3.9	1.1	0.1	0.3	0.1	0.2	0.0	0.0	0.1	0.2
	Max	9.1	12.5	4.9	1.2	1.2	1.0	1.1	1.0	1.0	0.9	1.1
	Min	3.1	4.4	2.6	0.9	0.6	0.7	0.5	0.9	1.0	0.6	0.8
	Dol 2 (DL cores-BL rims) (*N* = 8)											
	Mean	1.7	1.8	1.5	1.9	1.2	1.4	1.2	1.0	1.0	1.4	0.9
	SD	0.5	1.4	0.7	1.7	0.2	0.4	0.1	0.1	0.0	0.4	0.1
	Max	2.2	2.6	2.5	2.3	1.5	2.2	1.4	1.1	1.1	2.2	1.0
	Min	1.1	1.2	1.1	1.5	1.0	1.1	1.0	0.9	1.0	1.1	0.8
	Mean	2.0	2.2	2.2	1.7	1.3	1.2	1.1	1.0	1.0	1.2	0.9
	SD	0.5	0.6	0.7	0.2	0.2	0.3	0.1	0.1	0.0	0.3	0.1
	Max	2.6	3.2	3.6	2.1	1.7	1.9	1.3	1.2	1.0	1.9	1.0
	Min	1.3	1.5	1.6	1.4	1.1	0.9	0.9	0.9	0.9	0.9	0.8
	Mean	7.0	10.4	6.6	2.0	1.0	0.9	1.1	0.9	1.0	0.8	0.9
	SD	1.9	2.9	2.0	0.3	0.2	0.2	0.1	0.1	0.0	0.2	0.1
	Max	9.3	14.9	10.8	2.5	1.3	1.4	1.3	1.0	1.0	1.3	1.0
	Min	4.5	6.9	4.9	1.7	0.9	0.7	0.9	0.9	0.9	0.7	0.7
	Cal 2 (BL) (*N* = 11)											
	Mean	1.7	1.6	1.3	2.0	1.9	2.1	1.4	1.1	1.0	2.0	0.8

https://doi.org/10.1180/mgm.2025.10124 Published online by Cambridge University Press

SD	1.0	1.0	0.6	0.7	0.8	0.5	0.2	0.2	0.1	0.5	0.1
Max	3.5	3.6	2.4	3.2	3.1	2.8	1.7	1.3	1.1	2.8	1.0
Min	0.3	0.2	0.5	1.1	0.9	1.1	1.0	0.8	0.9	1.1	0.6
Mean	2.0	1.9	1.9	1.9	2.0	1.8	1.3	1.2	0.9	1.7	0.8
SD	1.3	1.3	0.8	0.8	0.9	0.4	0.2	0.2	0.1	0.4	0.1
Max	4.2	4.3	3.6	2.9	3.4	2.4	1.6	1.3	1.1	2.4	1.0
Min	0.3	0.3	0.7	1.0	0.9	1.0	0.9	0.8	0.9	1.0	0.6
Mean	7.0	8.9	5.6	2.2	1.7	1.3	1.3	1.0	1.0	1.2	0.8
SD	4.7	6.2	2.5	1.0	0.7	0.3	0.2	0.1	0.1	0.3	0.1
Max	14.7	20.5	10.6	3.4	2.7	1.8	1.6	1.2	1.1	1.8	0.9
Min	1.2	1.3	2.1	1.1	0.8	0.7	0.9	0.7	0.9	0.7	0.6
Cal 3 (BL) (*N* = 21)											
Mean	2.3	2.2	0.7	1.4	0.8	1.2	1.2	0.9	1.0	1.2	1.0
SD	2.5	2.4	0.5	0.4	0.3	0.1	0.1	0.1	0.0	0.1	0.1
Max	11.9	11.0	2.2	2.7	1.6	1.5	1.4	1.1	1.1	1.4	1.1
Min	0.5	0.5	0.3	1.0	0.5	1.0	1.1	0.8	0.9	1.0	0.8
Mean	2.7	2.7	1.0	1.3	0.9	1.1	1.1	1.0	1.0	1.0	1.0
SD	3.0	2.8	0.7	0.4	0.3	0.1	0.1	0.1	0.0	0.1	0.1
Max	14.2	13.3	3.2	2.4	1.8	1.3	1.3	1.2	1.1	1.2	1.1
Min	0.6	0.6	0.4	0.9	0.6	0.9	1.0	0.8	0.9	0.9	0.8
Mean	9.7	12.7	3.0	1.5	0.7	0.8	1.1	0.9	1.0	0.7	1.1
SD	10.5	13.4	2.1	0.5	0.2	0.1	0.1	0.1	0.1	0.1	0.1
Max	50.0	62.6	9.4	2.9	1.4	1.0	1.3	1.1	1.1	0.8	1.2
Min	2.2	3.0	1.2	1.0	0.5	0.7	1.0	0.8	0.9	0.6	0.8

Table 5D. Normalised Nd/Yb, Dy/Yb, Pr/Yb, La/Sm ratios, calculated La, Eu, Gd and Ce geometric anomalies according to Lawrence et al. (2006) and Pr, Eu and Ce anomalies according to Bau and Dulski (1996) of the investigated carbonate phases of the Calcare Metallifero Bergamasco. All the calculated parameters are normalised to Post Archean Australian Shales (PAAS, McLennan, 1989), Mud from Queensland (MuQ, Kamber et al., 2005) and Carbonaceous chondrites (C-1, Taylor and McLennan, 1981). N = normalised; SN = shale normalised; CN = chondrite normalised; BL = bright luminescent; DL = dull luminescent; NL = non-luminescent; PL = patchy luminescent.

https://doi.org/10.1180/mgm.2025.10124 Published online by Cambridge University Press